High-Speed Rotor Testing and Spin-Test Facility Development

by

Philip A. Miller

A thesis
presented to the University of Ottawa
in fulfillment of the
thesis requirement for the degree of
Master of Applied Science
in
Mechanical Engineering

ISBN 0-315-33303-0

ACKNOWLEDGMENT

The author is indebted to Dr RC Flanagan for his supervision, encouragement, and valuable suggestions throughout the course of the research and in the writing of this thesis.

He also gratefully acknowledges the financial assistance provided under National Research Council of Canada contracts OSU80-00043, OSU82-00422, and OST84-00459 and Natural Sciences and Engineering Research Council grants A1638 and G1009.

On behalf of all of the members of the Flywheel Project, a sincere expression of appreciation is extended to the supervisors, machinists, and technicians in the Departments of Mechanical Engineering, Civil Engineering, Chemical Engineering, and Physics, who have assisted along the way. Without their quality workmanship and excellent cooperation, the Project would have suffered immeasurably.

Nor would the Project have been able to test composite-hub rotor designs without the cooperation of Owens-Corning, Granville, Ohio, who contributed very high-grade glass composite plates in exchange for test data.

The support of colleagues in the Project and others associated with it is also acknowledged. The author is particularly grateful to his laboratory neighbor of three years, Luc Menard, for his valuable assistance in computational and other matters.

ABSTRACT

One of the promising new technologies to emerge from the energy crisis of the 1970s is the application of fiber composites to the design and manufacture of mechanical energy-storage rotors. An important component of the University of Ottawa program to build a 1-kWh usable-energy fiber-composite, energy-storage rotor ("ESR", or "flywheel" as some still prefer) was the development of a spin-test facility and the dynamic testing of composite ESRs and components.

This thesis describes the development of a world-caliber high-speed, spin-testing laboratory for the rotor program, beginning with only a vacuum chamber and video monitor, and the formulation, execution, and analysis of a number of unique spin tests. In a progressive fashion, component tests paved the way for material-property tests which, in turn, provided data essential for the design of the full-scale rotors that were the subject of the final tests.

In a series of destructive ultimate-speed tests, the biaxial tensile strengths of two sheet molding compound (SMC) and one S2-glass laminate disk specimens were found to be 212.8, 219.1, and 863 MPa, respectively, and the radial transverse strength of a carbon-fiber/epoxy resin ring wound in the rotor program's materials laboratory was found to be 36.5 MPa. In these tests, a novel method of bolting composite disks to a shaft attachment was proven to be feasible for the first time anywhere.

In a series of nondestructive tests, two metal-hub designs were found to be dynamically stable to speeds in excess of their designed maximum operating

speeds. Furthermore, their radial growth (dilation) versus speed behavior was found to behave predictably, an important result since both hubs were designed to exhibit large radial displacements for compatibility with composite-material rings.

Data from both test series were used in the design of four 1-kWh rotors, three of which were tested to their maximum operating speed. Of the three, two are composite-hub rotors with shrunk-fit carbon rings and the third, a flex-rim hub fitted with a biannular S2-glass/carbon ring. The flex-rim hub (FRH) rotor proved to be the most stable dynamically, but suffered from ring-manufacture and possible ring-assembly problems that resulted in two failures, one in the carbon ring, the other in the S2-glass ring. The fourth rotor design, a spring-spoke hub (SSH) and biannular ring, was assembled twice and an attempt was made to balance it, but it was never tested to speed because the runout and tilt could not be reduced to acceptable levels, requiring gross force and moment corrections. The failures of the FRH rotor rings did, however, prove that high-energy ESRs can be designed for safe failure, with the implication that containment-mass requirements may be reduced significantly.

In summary, this thesis describes the upgrading of the University of Ottawa Spin-Test Facility from a vacuum chamber and video system to the equivalent of many to the laboratories described in the literature. It then goes on to document several unique spin-test experiments.

GLOSSARY OF TERMS

ESR	–	Energy-Storage Rotor
FRA	–	Flex-Rim Attachment
FRH	–	Flex-Rim Hub
FFT	–	Fast Fourier Transform
MEST	–	Mechanical Energy Storage Technology
RPM	–	Revolutions Per Minute
Mil	–	Milliinch
S2L	–	S2-Glass Laminate
SMC	–	Sheet-Molding Compound
SSH	–	Spring-Spoke Hub
STF	–	Spin-Test Facility
a	–	radius of disk central hole
b	–	radius of disk
ν	–	Poisson's ratio
ρ	–	density
ω	–	angular velocity
σ	–	stress

CONTENTS

FIGURES

TABLES

Chapter I

INTRODUCTION

1.1 *Historical Perspective*

The Oil Crisis

The world price of one barrel of crude oil, in US dollars, rose from 2.60 to 11.60 between October 1973 and January 1974, profoundly affecting for many years the economies of every oil-importing country in the world. During the years immediately following this price discontinuity, initiatives were taken in many of these countries to develop oil-conservation technologies and, in a few of them, one of the emergent technologies took the form of mechanically storing energy in compact, lightweight, fiber-composite flywheels.[1] This thesis is concerned with the performance and dynamic testing of rotors of this kind, several of which have been designed, manufactured, and tested at the University of Ottawa.

The Ubiquitous Flywheel

The wheel was invented at least 5500 years ago. Two or three millennia later, the archeological record shows that one of these was used as a flywheel in the manufacture of pottery.

[1] Webster defines a flywheel as a "heavy wheel regulating the motion of a machine". A more appropriate generic term coined by RC Flanagan at the University of Ottawa is "energy-storage rotor" or ESR. Since "flywheel" has come to mean energy-storage device in the literature, both names are used interchangeably in this thesis, although ESR is preferred.

From the potter's wheel to stabilized inertial platforms, the flywheel today is to be found in many applications, none less obvious nor more prevalent than the classical heat-engine flywheel. In recent times, the flywheel has begun to evolve into a high-energy, lightweight mechanical energy-storage device which can be used, among other things, for propelling vehicles, either between periodical charges from external sources, or in a hybrid engine-flywheel powertrain where the rotor's charge is maintained by an on-board engine and by the recovery of braking energy.

Long before the energy crisis, but probably not before the appearance of the flywheel-powered toy car, the Swiss company Oerlikon A.G. manufactured flywheel-powered, regeneratively-braked trolley buses that travelled one mile between charges of their 1500-kg, 3000-rpm steel flywheels [1]. These buses were in service from 1950 until 1969 in Switzerland, Zaire, and Belgium. Ironically, it was the price of oil that both brought about the demise of the first ESR-powered bus in the '60s, and its resurrection in the '70s. The dramatic oil-price decline of the '80s has temporarily delayed the development of ESRs for buses, or any other vehicle for that matter, but this has not ruled out many other potential energy-storage applications that are independent of world oil prices.

The Transportation Flywheel

Around the time that the Oerlikon bus was being phased out of service, advanced steel flywheels were being developed in the United States, England, West Germany, and Russia. In 1974, Garrett installed a mechanical-energy storage system in two New York City subway cars for a trial period [2,3] and, in 1976, the University of Wisconsin installed a Garrett steel-flywheel system in a modified Ford Pinto [4].

Although steel-flywheel development was to continue for a brief time, weight, strength, safety advantages, and increasing availability would make fiber composites the materials of choice for ESRs. In fact, the Mechanical Energy Storage Technology (MEST) program created by the US Department of Energy in 1975 was specifically charged with the responsibility of developing fiber-composite rotors [5].

The Fiber-Composite Flywheel

After more than 20 years of flywheel research, Rockwell International's Rocketdyne Division pushed steel ESRs close to their ultimate design limit with a tapered, constant-stress, alloy rotor capable of storing 25.6 Wh/kg at its maximum design speed, an achievement that was matched by General Electric with its own steel-rotor design [6,7]. This, however, merely represents the starting point for composite-flywheel energy densities, as demonstrated in Table 1.1.

In addition to the higher specific strengths of composites (strength per unit density) compared with metals (Figure 1.1) composite flywheels can be designed to fail in a manner that requires substantially less containment than metal rotors of the same energy capacity. Togwood has estimated that the containment weight required for a composite rotor is only 15 to 30 percent of that required for a steel rotor [2].
Given that General Electric's prototype containment package weighed 36 kg (80 pounds) for a 10.1 kg rotor [12], one might conclude that the equivalent steel-rotor would require a containment mass somewhere between 100 and 200 kg. Under these conditions, the composite rotor stores a maximum of 11.1 Wh per kilogram of total energy-storage system mass, while the steel rotor stores only 3.0 to 1.6 Wh/kg. The University of Ottawa ESR experience suggests

Table 1.1: Flywheel Energy Densities

Specific energy densities for representative isotropic and quasi-isotropic energy-storage rotors.

Rotor Type	Total Energy (kWh)	Total Mass (kg)	Energy Density (Wh/kg)	Ref.
Flat steel disk	24.6	595.0	7.6	[3]
Tapered steel disk	16.0	624.0	25.6	[7]
Flat composite disk	0.23	10.5	21.3	[8]
Tapered composite disk	0.47	17.0	27.6	[9]
Composite disk/ring	1.34	34.4	39.0	[10]

that the GE containment, built to contain fragments, was more massive than necessary to contain a flywheel with a circumferentially-wound ring that is designed to fail in the transverse (radial) direction. Clearly, then, an order of magnitude improvement in energy-to-weight ratio is possible with composite over metal rotors.

Flywheel Economics

The quantity of fuel consumed by internal-combustion-engine vehicles is truly staggering. In 1981, Eisenhaure et al [13] estimated that the annual United

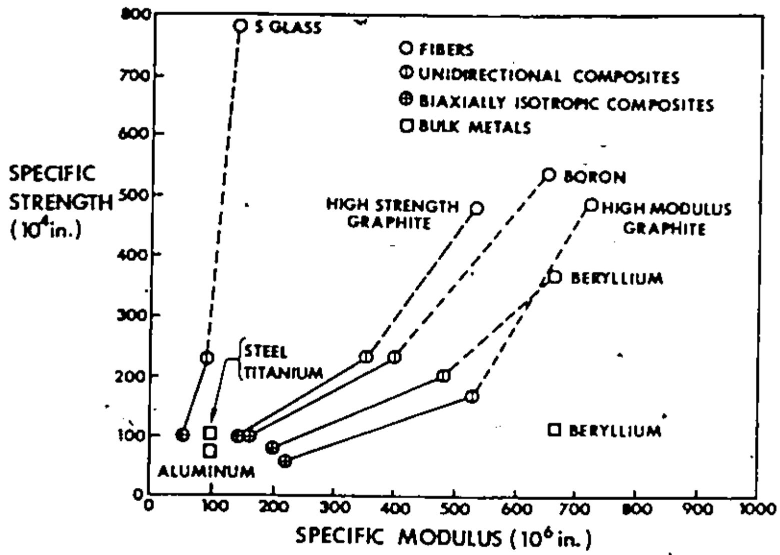

Figure 1.1: Specific Strengths of Metals and Composites. Strength and stiffness of advanced composite materials [11].

States general automotive consumption of gasoline was some 79 billion gallons, 1.4 billion gallons of which was attributed to taxi usage. In the same year, Krupka et al. [14] concluded that a saving in fuel costs of 50% for the New York City taxi fleet was feasible, employing state-of-the-art, steel-flywheel technology. Thus, a potential 1981 saving in fuel costs (albeit a simplistic one) of some $0.8 billion existed, in that year, for US taxis alone. The University of Wisconsin's demonstration of a 25% fuel-economy saving with a steel-flywheel-equipped Ford Pinto, and its projection of a 50% saving with a second-generation, fiber-composite rotor-equipped car [15] lends some credibility to the economic studies of Eisenhaure and Krupka.

The Scale of Flywheel Research

Under the MEST program, the US Government spent about 20 million dollars on flywheel R&D during the years 1975-1981.[2] Elsewhere in the world, the

[2] Data extracted from references [26]-[28].

scale of research in 1977[3] was estimated by Rabenhorst to have been in excess of $3 million per year on the basis of communications with colleagues in various countries [16].

In terms of applications, the American program focussed mainly on vehicles, with minimal effort directed toward stationary energy-storage-application development. In other countries in which flywheel research was taking place, there was a more balanced distribution of effort. For example, in 1980, the West German company Maschinenfabrik Augsburg Nurnburg (MAN) was developing a steel-flywheel-storage system for diesel-bus installation [17], while the French Societe National Industrielle Aerospatiale was applying its satellite flywheel technology to earth-bound, stationary applications [18]. The results of an ambitious Italian National Research Council sponsored flywheel-testing program, reported in 1982 [19], were based on a variety of rotors suitable for moving or stationary applications.

The beginning of Canadian research in this area was marked by the publication of analytical system studies during the mid to late '70s by Flanagan et al. of which [20] and [21] are representative references. These led eventually to the awarding of several Canadian Government contracts to the University of Ottawa, beginning with a materials study in 1980 [22]. The University of Ottawa Rotor Project was ultimately directed toward the development of a fiber-composite rotor capable of storing 0.75 to 1.0 kWh of usable energy.[4]

---

3 For the countries France, W Germany, Italy, Japan, S Africa, and the UK combined. Switzerland and Russia were mentioned but, although there was evidence of flywheel research in Russia at least, no figures were given for either country.

4 Usable energy is defined as the energy available between the maximum and minimum operating speeds. The minimum speed is usually 50% of the maximum.

1.2 Thesis Objectives

The objectives of this thesis are primarily experimental in nature, broadly based, and tightly integrated into an R&D rotor-development program requiring the continual development and refurbishment of a sophisticated test laboratory. The establishment of the test laboratory, in this case, assumes additional significance because the equipment was to become a permanent test facility; therefore, the developmental aspects of this thesis are of primary importance in the following list of objectives:

1. Establish a high-speed spin-test facility (STF) capable of both destructive and nondestructive testing of high-energy-density fiber-composite rotors and rotor components.
2. Test ESR component performance and dynamic behavior.
3. Determine fiber-composite material strengths under centrifugal loading (biaxial tensile strengths).
4. Collect and interpret performance and dynamic-response data for 1.0 and 1.33-plus kWh composite-ring, high-energy-density rotors.

In Chapter II, these objectives are considered further within the context of the University of Ottawa Rotor Project.

1.3 Literature Survey

The bulk of composite-flywheel spin-test literature has been generated by US MEST program contractors and published in the proceedings of three Flywheel Technology Symposia [23,24,25] and six Annual Contractors' Review Meetings [26,27,28,29,30,31].

The results of this survey are concerned primarily with this body of literature and are discussed under the following categories:

1. Spin-test facilities.

2. Published spin-test results.

3. Flywheel dynamics:

1.3.1 Spin-Test Facilities

The majority of organizations engaged in flywheel research were able to do their own spin testing with varying degrees of sophistication, but only a few have offered any equipment or test-procedure details.

In the United States, two laboratories were described in detail in the literature, probably because of their publicly-funded role as test facilities within that country's flywheel research program. The status of Oak Ridge, particularly, as a national laboratory, made it better equipped than Johns Hopkins for that purpose.

For the same probable reason, an Italian facility was the only laboratory outside of the USA to be described in detail.

1. Johns Hopkins University (JHU)

In general, the JHU Flywheel Test Laboratory (FTL) is the most ambitious of the surveyed test facilities [32]. Its equipment includes:

- TEST CHAMBERS AND VACUUM SYSTEMS

  Four spin-test chambers: two horizontal-axis and two vertical-axis cylinders, designed for a range in rotor sizes from less than one kilowatt-hour to many kilowatt-hours, and for stationary and mobile rotor-installation applications. Of the four chambers, two are equipped with air motors, one is set up for testing rotor/dynamometer systems, and the fourth was to be powered by a 125-hp dynamometer.

Vacuum is maintained by mechanical-diffusion and mechanical-blower pump combinations, or by mechanical pumps alone.

- INSTRUMENTATION AND CONTROL

Conventional turbine speed control with electromagnetic braking and an anti-resonance device for controlling whirl in the typically long quill shafts used by FTL in two of its chambers.

Video recording with microcomputer-generated alphanumerics (date, time, speed, and energy) and high-speed still cameras.

Eddy-current displacement-probe system for monitoring x-y motion (in one plane) and an accelerometer mounted on the turbine body for z-motion detection.

2. Union Carbide

Union Carbide's 2-kWh-capable Oak Ridge Flywheel Evaluation Laboratory (ORFEL) [33] became operational in 1979 [34] with the following features:

- TEST CHAMBER AND VACUUM SYSTEM

One vertical-axis cylinder equipped with an impulse air turbine and an unspecified, but probably mechanical-diffusion combination, pumping system.

- INSTRUMENTATION AND CONTROL

Conventional turbine speed controller/tachometer; 60,000-rpm turbine with bidirectional torque capability.

Standard 30-Hz scan-rate video monitoring with stroboscopic illumination.

Eddy-current and electrooptical displacement measuring transducers; pyrometer for rotor-temperature measurement.

Torque-measuring equipment to measure momentum transfer to containment during flywheel failures.

3. Politecnico di Torino

The original paper describing the design and construction of this Italian spin-test facility was not available in English. However, some facility details are available in the cited reference [19]:

- TEST CHAMBER AND VACUUM SYSTEM

  A vertical-axis cylinder with asynchronous electric motors for rotor energies exceeding 2 kWh and an ultimate vacuum-pressure capability of 7.5 mTorr; rotary - booster pump combination.

- INSTRUMENTATION AND CONTROL

  Variable-frequency converter electric-motor speed controls. Video monitor with stroboscopic illumination; tachometer.

4. Comments

The FTL at Johns Hopkins was established for fiber-composite burst (materials) and long-term, utility-type rotor testing.

ORFEL was set up specifically to do burst, containment, and cyclic testing for the MEST program. Its cyclic-testing capability was used to cycle two small rotors 10,000 times between 50 and 100% of their maximum operating speeds. This facility conducted most of the important spin tests for the US program.

The flywheel laboratory at the Politecnico di Torino is sponsored by the Italian National Research Council to investigate a variety of flywheel materials in composite and bare-filament form. The selection of an electric-motor drive was likely dictated by high power and torque requirements.

In general, the vertical-axis cylindrical spin-pit with a heavy, crane-removable lid has been the most commonly used type of chamber, offering relatively simpler containment arrangements, but suffering from the real disadvantages of lid hoisting/lowering and the lack of access to the rotor with the lid in place.

ORFEL has the best rotor-tracking equipment and is able to monitor not only the motion of the rotor arbor, but the motion of the ring radially and axially with respect to the arbor.

The papers on these three facilities each contain some reference to an in-house rotor-balancing capability, but only ORFEL describes routine, in-chamber, high-speed balancing, without specifying the method used.

1.3.2 Published Spin-Test Results

The surveyed literature contains test results and/or rotor design parameters published by or on behalf of thirteen organizations.[5] These details are summarized in Table 1.2 to give the reader an appreciation of the depth and diversity of fiber-composite flywheel research.

In the table, these rotors are divided into the following types:

1. A1: Flat metal disk.
2. A2: Tapered metal disk.
3. B1: Flat composite disk.
4. B2: Tapered composite disk.
5. C1: Composite-disk hub/composite rim.
6. C2: Composite-spoke hub/composite rim.
7. D1: Metal hub/composite rim.

---

[5] Profit and nonprofit corporations, research institutes, and universities.

Table 1.2: Published Spin–Test Results

A summary of spin–test data from the literature survey.

Type	Builder	Ident	Materials	Mass (kg)	Inertia (kg-m2)	Speed (rpm)	Energy (kWh)	Density (Wh/kg)	Ref
A1	Oerlikon	GyBus	4340	1500.0	498.0	3000	6.8	4.5	[1]
A1	Garrett	ACT–1	4340	595.0	24.43	11,000	4.5	7.6	[3]
A1	Garrett	R–32	4340	335.6	10.72	14,000	3.0	8.9	[3]
A1	Garrett	USPS	4340	15.1	0.069	36,000	0.134	8.9	[34]
A1	Garrett	Pinto	4340	71.4	5.27	11,000	0.97	13.6	[35]
A2	Rockwell	M'COM	4340	1172.0	N/A	N/A	30.0	25.6	[6]
A2	GE	GEBus	4340	624.0	79.46	11,500	16.0	25.6	[7]
A2	MAN	MAN–1	4340	226.0	6.84	12,000	1.5	6.6	[17]
B1	GE	GED	S2L	10.6	0.206	24,600	0.19	17.9	[37]
B1	OU	S2L–19	S2L	10.5	0.277	23,082	0.23	21.3	[8]
B2	Rockwell	IPACS	N/A	27.2	0.899	35,000	1.68	61.7	[36]
B2	Fokker	N/A	E–glass	17.0	0.450	26,200	0.47	27.6	[9]
C1	OU	FW1–1	SMC/C	40.9	1.78	19,100	0.99	24.2	[10]
C1	OU	FW2–1	S2L/C	34.4	1.41	25,000	1.34	39.0	[10]
C1	GE	GE–F	S2L/C	10.1	0.192	27,300	0.218	21.6	[37]
C2	Brobeck	GFE	Kev	55.8	2.92	32,725	4.95	88.7	[38]
C2	Garrett	G–3	C/Kev	10.1	0.482	23,640	0.410	40.6	[12]
D1	Garrett	NTEV	Al/Kev	22.7	2.57	16,000	1.0	44.0	[35]
D1	OU	FW3–1	Al/S2/C	37.8	1.89	21,900	1.38	36.5	[10]
D1	Garrett	EPPV	Al/Kev	20.6	1.05	25,000	1.0	48.5	[2]
D1	Garrett	ESU	Al/Kev	6.6	0.093	42,000	0.250	37.8	[39]

Legend:
- 4340 – ASTM 4340 Steel
- S2L – S2–glass laminate
- SMC/C – SMC hub, carbon ring
- Kev – Kevlar
- C/Kev – Carbon hub, Kevlar ring
- Al/S2/C – Aluminum hub, S2–glass inner, carbon outer rings
- Density – Energy density (Watt–hours/kilogram)
- N/A – Not available

1.3.3 Flywheel Dynamics

The first published model derived specifically for, and tested against, a flywheel pendulously suspended from a flexible quill shaft is that of Thomson et al. [41]. This two–degrees–of–freedom model represents an improvement over that of an earlier model by Den Hartog [42] in that the upper end of the shaft is treated as flexibly mounted while Den Hartog's is rigidly clamped.

The object of Thomson's model was to predict speeds at which forward or retrograde whirling modes would be excited. These were compared with a number of tests with "substantial agreement".

The governing equation for the two-degree model that was used in the Den Hartog/Thomson scheme was coded at the University of Ottawa, by McRae [43], with shaft length as parameter, and was used to determine the length of quill shaft that would best avoid whirl resonances for a particular rotor.

More complex models were developed by Bert and Ramunujam during the US MEST program [44]. The first model comprises a massless shaft connecting four lumped masses, three with two degrees of freedom and the fourth with one, for a total of seven. The second model substitutes a distributed-mass (so-called Euler beam) shaft for the massless shaft and becomes a combined distributed/lumped parameter model with an infinite number of degrees of freedom. These models were coded and run with and without forcing functions for several actual rotor designs. Only one set of data was available for comparison with the model and was in good agreement. Additional data are needed to test the accuracy of these models.

Another variation on the modeling of Den Hartog/Thomson is that of Olszewski [38]. In this case, the model was used to predict whirl maps for each rotor tested at the Union Carbide Oak Ridge Laboratory in order to predict first critical speeds and other possible resonance points. The model was forced to conform with test data by varying the "effective shaft length".

1.4 Thesis Overview

A background of flywheel research in general has been given. The thesis objectives have been described and a pertinent review of the literature given.

In the following chapters, details of STF development and spin tests are described. Chapter II is devoted exclusively to the development of the Spin-Test Facility, while Chapter III describes the evolution of the Facility's test procedures.

The 100-Wh and 1-kWh rotor test reports in Chapters IV and V, respectively, are all structured in the following manner:

1. Introduction
2. Procedure
3. Results and Discussion

Frequently, the Introduction is common to several experiments and includes a description of the purpose and scope of the investigation, as well as its most significant outcome. The Procedure section states the general outline of the performance of the test and describes any special measurement methods or apparatus used. The final section, Results and Discussion, gives the results in tabular or graphical form with an estimate of experimental error, and a comparison of the results with theoretical values and/or relevant results of other investigators. Attention is also drawn to any pertinent limitations.

A general summary of all tests and conclusions drawn therefrom is given in Chapter VI.

Chapter II

SPIN-TEST LABORATORY

This chapter describes the laboratory (Spin-Test Facility or STF) that was developed by the author in order to perform both destructive and nondestructive tests with high-energy-density, fiber-composite rotors and their components, and to perform material ultimate-strength measurements. The facility is the only one of its kind and capability in Canada and is unique, with respect to some aspects of its design and objectives, in comparison with the few similar laboratories in North America. Before describing the laboratory, an overview of its development and integration into the Energy-Storage Rotor Program is in order.

2.1 STF Development and ESR Program Overview

2.1.1 The Flywheel Project, 1979-83

The University of Ottawa Flywheel Project began with a 1980 National Research Council of Canada (NRC) contract to assess 1.0-kWh (usable energy with a 2:1 speed range) high-energy-density fiber-composite rotor designs and to develop a corresponding manufacturing and materials data base [22,45]. Coincidentally, installation of a spin-test chamber began modestly [46] with Natural Sciences and Engineering and Research Council (NSERC) support.

During the next two years, as a filament-winding and composite-materials testing laboratory was being established, Spin-Test Facility development continued with the installation of the original air turbine and drive shaft [47], and the addition of steel containment rings and rudimentary monitoring equipment [43]. As the STF matured, spin testing began with isotropic materials (plexiglas) to prove the system, and continued with various other tests [43].

The plexiglas tests were generally successful in that failure speeds were sufficiently predictable to verify commonly-used stress equations. The results of these tests are summarized in Table 2.1, where the failure stress in each case falls within the limits of 48.3 – 75.8 MPa given for methylmethacrylate in the CRC Handbook [48]. The drive system, however, was prone to misalignment because of its length (see Figure 2.1), usually resulting in high-speed resonances. Coupled with the lack of both external damping in the drive system and an in-house balancing capability, these problems made successful spin tests something of a random exercise. In the end, the high speeds required for the longitudinal failure of radially-thin, small-diameter composite rings proved unattainable due to system resonances, and larger-diameter rings could not be driven to failure because of rotor imbalance.

By 1983, the STF had reached the level of development described in reference [49], as summarized below:

- VACUUM TEST CHAMBER

  A turbine/drive shaft assembly mounted vertically in a 1.0-m-diameter by 1.5-m-long tank with a heavy welded-in support structure for mild steel containment rings [43] and a vertically-hinged, front-closing door. The chamber could be evacuated to 100 milliTorr by a single two-stage mechanical pump in an hour.

Table 2.1: Summary of Early Plexiglass Tests

Spin–test results for plexiglass disks of three different diameters, based on eq. (1) of Chapter 4 with $r = 20.7$ mm, $\nu = 0.25$, and $\rho = 1190$ kg/m^3.

Outside Diameter (cm)	Axial Thickness (cm)	Failure Speed (rpm)	Ultimate Stress (MPa)
30.48	0.95	15,930	61.8
		14,450	50.9
		12,830	40.1
		16,000	62.4
		15,150	55.9
		16,960	70.1
17.78	0.95	29,190	69.3
		27,220	60.3
		24,140	47.4
		25,340	52.2
		26,830	58.5
		23,990	46.8
26.27	2.54	17,950	58.2
		16,790	50.9

Note: the ultimate stress is the stress at failure speed at the hole radius, calculated with eq. (1), page 70, and then multiplied by two (maximum hole effect).

INSTRUMENTATION AND CONTROL

An electro–pneumatic throttle for acceleration and a simple solenoid valve for braking.

A turbine tachometer for rotor speed, averaged over one second, to within 20 rpm.

A video cassette recorder for recording the tachometer display, the rotor image and control–room and chamber audio.

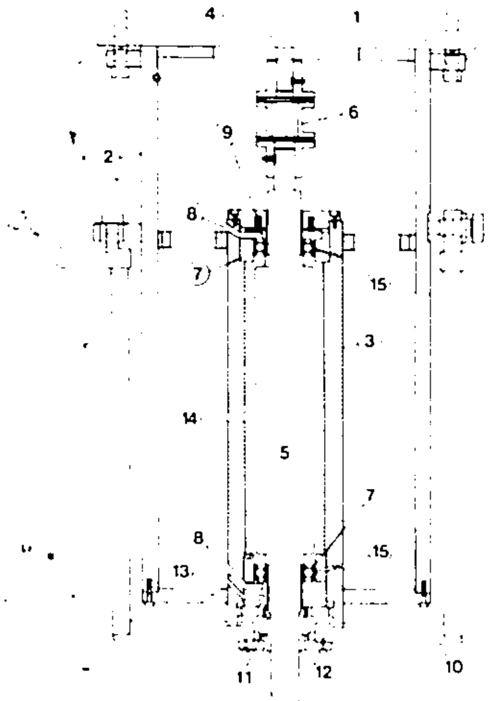

Figure 2.1: Original Turbine Installation. Legend: (1) turbine, (2) main housing, (3) centering column, (4) turbine shaft, (5) drive shaft, (6) flexible housing, (7) bearings, (8) mist lubrication port, (9) bearing preload springs, (10) turbine well, (11) lip seal, (12) cooling-fin collar, (13) cool-air port, (14) exhaust ports, and (15) thermocouple ports.

- TESTING

During the 1981-83 period, 60 spin tests, broken down by type in Table 2.2, were carried out.

The bulk of these tests (32) were ultimate-speed (or burst) tests to measure failure stress in plexiglas (methylmethacrylate) disks and rings of different dimensions. The objectives of these tests were to gain test experience, to verify stress theory, and to test the system's ability to produce consistent results.

Table 2.2: Summary of Early Spin Tests by Type

Rotor Type	Material	Diameter (cm)	Objective	No. of Tests
9.5-mm disk	Plexiglas	30.48	Burst	17
9.5-mm disk	Plexiglas	17.78	Burst	7
2.54-cm disk	Plexiglas	26.67	Burst	2
6.4-mm ring	Plexiglas	12.07	Burst	6
Simulator(1)	Plexi/Al	13.97	Dynamics	3
Star-Hub	Aluminum	28.67	Dynamics	4
Bar-Hub	E-glass	55.88	Burst	5
2.54-cm disk	Nylon	26.67	Dynamics	16

Notes: (1) The simulator was an aluminum and plexiglas combination simulating the star-hub rotor's mass and inertia.

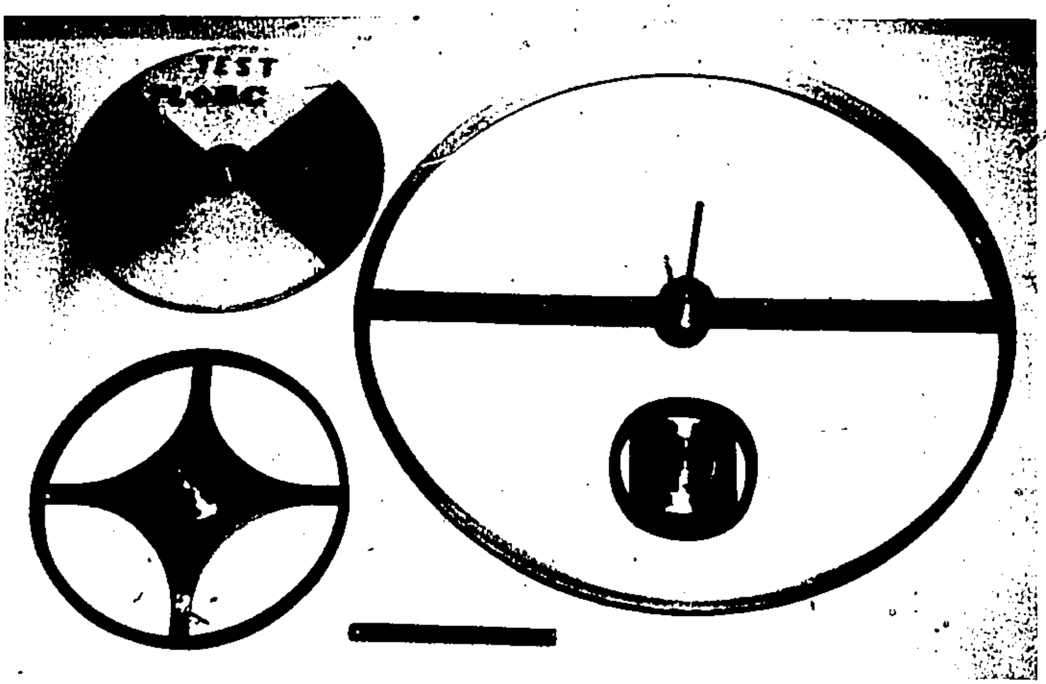

Figure 2.2: Early Test Rotors. Counter-clockwise from the top left: 30-cm plexiglas disk, star-hub with carbon ring, square-hub with plexiglas ring, and bar-hub with E-glass ring. The scale rule is 15 cm.

The remainder of these tests included: ring/bar-hub tests, attempts to fail a 55.9-cm-diameter E-glass ring on an E-glass bar hub; star-hub tests, precursors to tests in which 26.7-cm-diameter thin carbon rings were to be failed circumferentially on these hubs (see Figure 2.2 on page 19); and others, such as the simulator series, which unintentionally demonstrated the system's deficiencies at higher speeds.

2.1.2 Research Period, 1983-85

- FACILITY DEVELOPMENT (OBJECTIVE 1)

Fuelled with NRC Phase I contract funding and continued NSERC support, STF redesign and monitoring-system installation became a primary program objective during this period. Most of the drive difficulties discussed above were eliminated with an air-turbine that minimized the occurrence of resonances by reducing the number of couplings to one and by shrinking the overall drive length. Although the external shaft damper on this unit quietened expected resonances, it unexpectedly produced another form of resonance (oil whip) that was tolerable once it was understood. The new drive system not only simplified spin-testing operations, but in combination with advanced instrumentation and the ability to dynamically balance rotors, it ensured that failure stresses could be confidently attributed to spin motion alone, as opposed to a combination of spinning and whirling.[6]

To eliminate the risk of air-induced vibrations, an improved vacuum system was installed in the form of a mechanical-pump-backed Roots blower. This improved the pumping rate as well as the tank ultimate pressure.

Improvements in the STF's capability for safely spinning rotors at high speeds would have been incomplete without the means of measuring and recording their motions. This was accomplished with a monitoring system

---

[6] Whirling is the motion of the spin axis about its undeflected position.

based on non-contacting, eddy-current proximity transducers.

Finally, in support of high-speed spin testing, an in-house rotor balancing capability was developed [50,51].

SPIN TESTS. (OBJECTIVES 2, 3, & 4)

As STF improvements were incorporated, spin tests of small isotropic (aluminum) system-commissioning rotors were conducted to test system capabilities and methods of mating components [52]. During this time, two simulators (small test rotors) were spun regularly to their maximum speed in order to test rotor balance and to observe system dynamics.

When the STF was declared operational, the first material test was carried out: an ultimate-speed (burst) test of a sheet molding compound (SMC) hub, later verified by a second SMC test. An alternative composite-hub material, an S2-glass laminate lay-up, was similarly tested. As will be described in detail later, the first of the laminated hubs did not fail because the material was much stronger than expected, placing its failure speed well outside of the turbine's speed range. A subsequent test, with a hub weakened by a central hole to reduce its failure speed, was successful.

A prototype composite-hub rotor (E/XAS carbon ring on an SMC hub) was built so that the ring would fail transversely to the fiber direction, that is, the ring was made sufficiently thick so that it would fail radially while the stresses in the hub, hub attachment, and in the ring circumferential direction were still well below failure levels. Considered to be the most important of all program tests, the objective of the ring-radial-strength (RRS) rotor test was to evaluate overall rotor design, including: filament winding technology; residual, interfacial-pressure, and inertial stress analyses; rotor-component compatibility; assembly; and all test procedures developed prior to this test.

The flex-rim attachment (FRA)[7] was implicitly tested during each of these experiments, the test being to detect any rotor motion that could be "blamed" on the FRA, and to watch for any sign of incompatibility between the FRA and the hub.

A second set of tests under Objective 2 was performed to determine the intrinsic stability of two metal-hub rotor designs. These were conducted with flexible-rim hub (FRH) and spring-spoke hub (SSH) prototypes, first with single S2-glass rings and later with biannular S2-glass and E/XAS carbon rings.

Finally, four full-scale preproduction-prototype, 1-kWh ESRs were built and three of these were tested to their maximum operating speeds to observe and record rotor response. These rotors are identified as follows:

- FW1-1: SMC disk hub, bolted shaft attachment, and E/XAS carbon ring
- FW2-1: S2-glass laminate hub, bolted shaft attachment, and E/XAS carbon ring
- FW3-1: flexible-rim hub, biannular S2-glass - E/XAS-carbon rings
- FW3-2: flexible-rim hub, biannular S2-glass - E/XAS-carbon rings
- FW3-3: flexible-rim hub, biannular S2-glass - E/XAS-carbon rings
- FW4-1: spring-spoke hub, biannular S2-glass - E/XAS-carbon rings

- RESEARCH RESULTS

The redesigned and reequipped Spin-Test Facility met all expectations for carrying out the planned research. The ultimate-speed (burst) tests of composite-hub materials provided the requisite ultimate-strength data for the design of composite-hub flywheels.

---

[7] The bolt points on the FRA are designed to move radially with the composite hub as centrifugal forces cause radial deformation in both, thereby maintaining radial compatibility of the bolt holes in both components over the rotor's speed range.

The flexible-rim attachment concept was proven, as was the unprecedented through-drilling of composite hubs for the FRA bolts, by virtue of the fact that no resonances occurred that could be attributed to the FRAs, and the fact that one of the FRAs withstood a stress level 2.65 times its design maximum by remaining intact, although yielding considerably.

The prototype metal-hub rotors were tested well beyond the maximum design speeds of their full-size counterparts. Only an inadvertently weakened ring prevented the spring-spoke hub rotor from reaching its overspeed limit of 30,000 rpm, while the FRH rotor attained its limit of 35,000 rpm on several occasions.

Three of the four large rotors were tested to their maximum design speeds. Although FW3-1 suffered a radial failure in its carbon ring just as it reached maximum, it was rebuilt, derated, and run successfully to its reduced maximum speed of 20,000 rpm several times. Subsequently, a redesigned ring system was tested on the original FW3-1 hub and resulted in an S2-glass ring failure at 97% of design speed. Sufficient vibration data were collected to show that the first three rotor designs were intrinsically stable under dynamic conditions. FW4-1 had unacceptably large radial runout and tilt, making it impossible to balance for high-speed testing.

2.2 *Spin-Test Facility*

As an introduction to the detailed description of the laboratory equipment in the following section, this section gives the layout of the facility and a system overview.

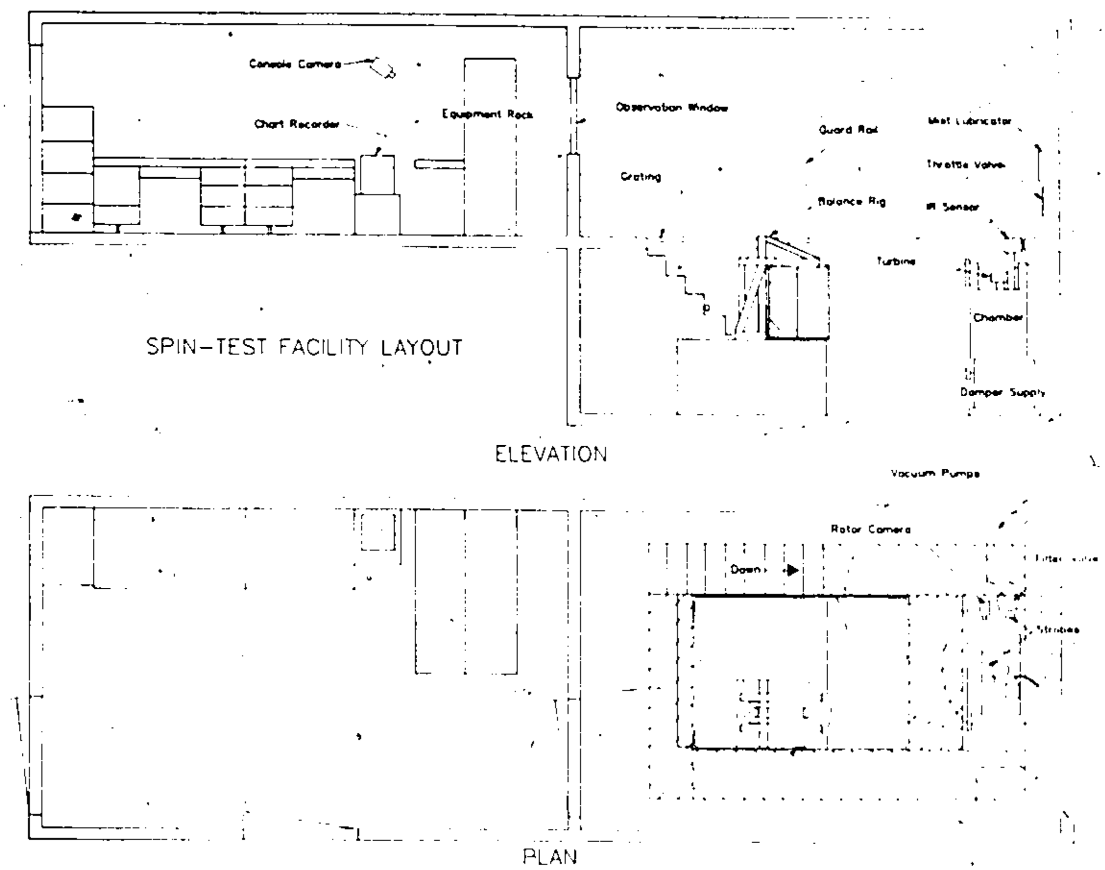

Figure 2.3: University of Ottawa Spin–Test Facility Layout

2.2.1 Laboratory Layout

The layout of the laboratory is shown in Figure 2.3, where the following details are emphasized:

1. The control room is separated from the chamber room by acoustic insulation.
2. The chamber itself is below the control–room level.
3. Although the gradual changeover to in situ balancing has been completed, the vertical–axis balance rig is conveniently located for special balance procedures or experiments [50].

4. A gantry for lifting rotors or other heavy objects, including the chamber itself, is permanently located in the chamber room.
5. The full-flow ventilation system has been sealed off and a wall-heater unit and ceiling fan installed to maintain constant temperature in the chamber area.
6. The control room doubles as an office with the control console to one side.

2.2.2 *Control Room and Test Chamber*

The main pieces of equipment in the laboratory are shown in Figure 2.4. Figure 2.5 is a schematic presentation of the various elements of the laboratory and their interrelationship.

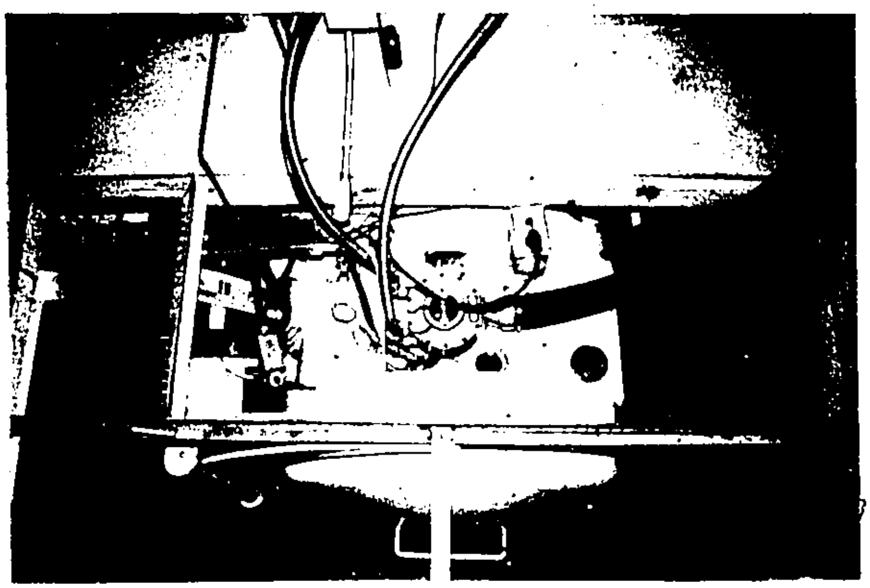

Figure 2.4: Control and Chamber Rooms. Top: control room; bottom: chamber.

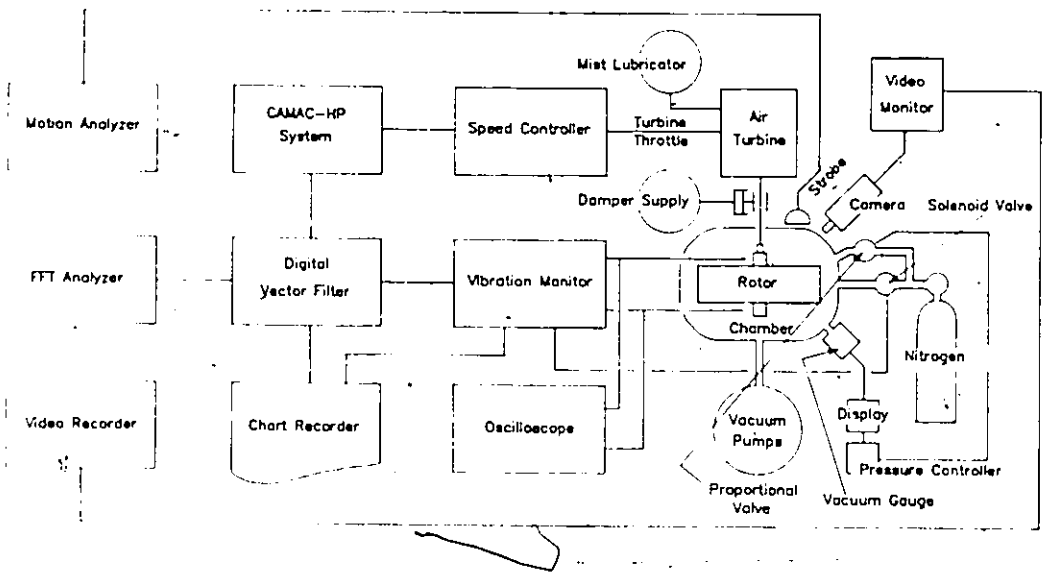

Figure 2.5: Schematic of Laboratory Equipment

2.2.2.1 Equipment List

1. CHAMBER

   Fabricated in-house from a 76-cm section of 1.2-m-diameter, 16-mm-thick A285 steel, the vacuum chamber has a welded rear end-cap and a flanged front door, both being dished to withstand external pressure [45].

2. AIR TURBINE

   Barbour Stockwell 2702, four-inch, bidirectional, impulse air turbine, providing 10 hp and 2.6 ft-lb torque at 35,000 rpm when supplied with 100-psig, 125-scfm air. Turbine air is exhausted outdoors via a cell-exhaust system. This has the secondary benefit of quietening the turbine's operation significantly.

3. DAMPER SUPPLY UNIT

Barbour Stockwell SOL-124. This device circulates variable-pressure oil to the shaft-damper section of the turbine.

4. DAMPER PRESSURE CONTROLLER

A modification to the damper supply enables the operator to adjust the oil pressure from the control room. A mechanical pressure gauge on the SOL-124 unit is viewed from the control room via television.

5. TURBINE THROTTLE VALVE

Valtek Mark Two, electric – fluidic control valve.

6. BRAKE VALVE

A solenoid valve. The flow of air in the brake line is regulated by a manually-operated globe valve.

7. MIST LUBRICATION UNIT

Norgren 13-203 Mist Lubricator. This device continually bathes the turbine bearings in a cool oil mist.

8. DAMPER-OIL THERMOCOUPLES

Analogic K-type thermocouples installed in the damper-oil inlet and outlet lines.

9. VACUUM PUMPS

Edwards High Vacuum EH250 Roots blower and E2M18 two-stage rotary-vane pump.

10. VACUUM GAUGES

Granville-Phillips 275 Pirani gauge and Vacuum General CMT 80-6B capacitance manometer.

11. PRESSURE CONTROLLER

Vacuum General 80-1 controller and 79-6A magnetically-actuated proportioning valve.

12. TRACKING FILTER

Bently Nevada DVF2; Series 9000 proximity transducer system.

13. VIBRATION MONITOR

Bently Nevada 9000 Series monitor with two dual vibration monitor cards (four channels), power supply and annunciator relays.

14. OSCILLOSCOPE

Tektronix 5111A storage oscilloscope with 5A20N differential amplifier, 5A15N amplifier, and 5B10N time base. Tektronix C5C camera.

15. TELEVISION MONITORS

Electrohome EVM1719 (17 inch) and RCA TC1109 (9 inch).

16. TELEVISION CAMERAS

Two Sony AVC 3200 and one RCA TC 2000.

17. VIDEO RECORDERS

Sony SL-5800 and SLZ300 video cassette recorders.

18. VIDEO MIXER

Vivcon Industries V27SP Inserter/Splitter.

19. AUDIO MIXER

Sony MX-510.

20. SIGNAL ANALYZER

Ono Sokki CF-920 mini-FFT analyzer.

21. ROTOR-TEMPERATURE SENSOR

Ircon Inc. Modline 8000 Series infrared sensor, range 20 – 200 degrees C.

22. ROTOR ILLUMINATION

Bruel and Kjaer Type 4911 Motion Analyzer with two lamps.

23. CHART RECORDERS

NEC San-Ei 8K20 six-channel, thermal pen. Gould 2400 four-channel, thermal pen, two thermocouple amplifiers.

24. TURBINE CONTROLS

Barbour Stockwell 107-B Tachometer and 105-E Speed Control.

25. COMPUTER

CAMAC System with Digital LSI 11/23 microcomputer, LeCroy 8212 Digitizer, Kinetic Systems 3080 8-bit output register, Winchester 16.5-M hard disk. Intermediate HP-1000 L Series Model 5 minicomputer.

26. TERMINAL

TeleVideo 925 terminal.

2.2.3 System Overview

A systematic approach is taken to describe the operation of the Spin-Test Facility which is represented by the functional block diagram in Figure 2.6.

Within the chamber system there are the means for sustaining a moderately high vacuum; for containing rotor fragments; for accessing optical, infrared, and electrical signals; and for supporting the drive system.

The drive system, defined to include the turbine and rotor, interfaces with the audio-visual monitoring system, the vibration monitoring system, and the vacuum system. By means of the audio-visual system, the operator sees and manually controls the rotor speed. If amplitude limits are exceeded, the vibration system can be enabled to shut down the drive system. This also applies

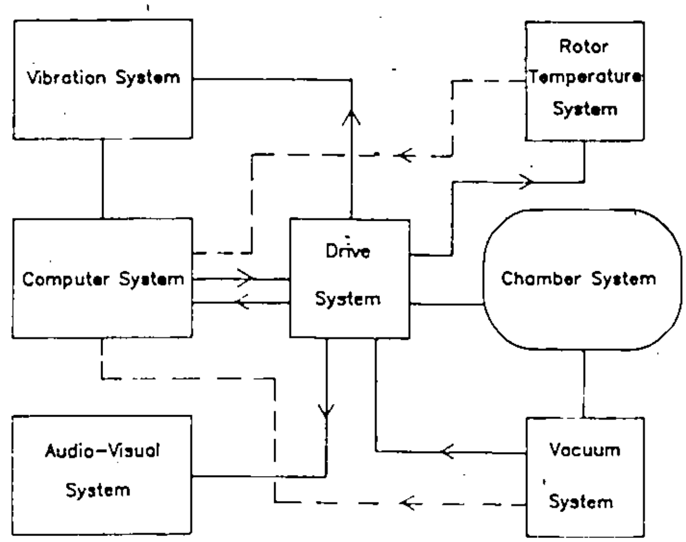

Figure 2.6: Functional Block Diagram of STF. The broken lines denote future capabilities. The arrows indicate data or control flows.

to the vacuum system if the pressure in the chamber rises above a preset level. Finally, the computer system supports software for cyclic (on-off) control of the turbine and vibration, speed, and time data logging.

The vacuum system maintains chamber pressure, feeds back pressure data, and maintains preset chamber pressure levels when required.

The computer system, comprising local and mainframe computers, stores vibration data (and has the capability of storing temperature and vacuum data as well) while the temperature-monitoring system remotely senses the rotor's temperature.

The vibration-monitoring system, in addition to logging and analyzing vibration data, interfaces with the audio-visual system by means of the video recording of the rotor, vibration parameters, and oscilloscope waveforms.

2.3 Laboratory Equipment and Specifications

2.3.1 Chamber System

Figure 2.7 illustrates the principal features of the chamber.

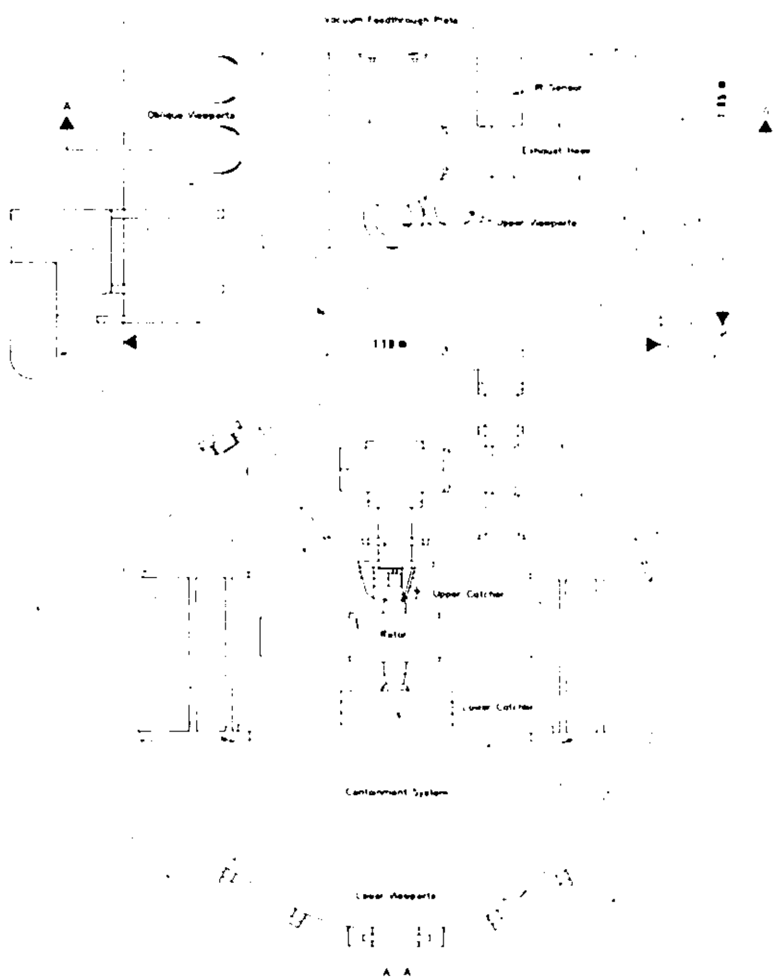

Figure 2.7: Chamber

The spin chamber has a volume of approximately 3 cubic meters. Its four I-beam legs are solidly anchored with 2.5–cm studs welded to steel plates imbedded in the concrete floor which, in turn, is vibration-isolated from the building. This anchoring system constrains spin-axis motion to within one minute of arc, making it unnecessary to relevel the turbine each time the door is opened.

The chamber has seven optical viewports with plexiglas windows used for up to two television cameras and two strobe lamps at one time. A calcium fluoride port is used for the infrared sensor port. The proximity transducers communicate to the chamber exterior via instrument feedthroughs screwed into an aluminum plate which in turn is bolted to the rear wall of the turbine box. All windows, the vacuum feedthrough plate, and the door are sealed with O-rings. The turbine is bolted to a horizontal, 5-cm-thick steel plate that forms the floor of the box-like chamber modification that was required in order to accommodate it. It is sealed to this plate with ordinary gasket material that permits levelling of the turbine by adjusting the nuts on four mounting studs. The turbine has an integral rotating shaft seal that is either a rubber lip seal for destructive tests, or a carbon-face seal for nondestructive tests. The remaining chamber openings are: two purge ports, three vacuum-gauge ports, and the outlet port to the vacuum pumps.

Inside the chamber, 20-mm-thick curved, mild-steel containment plates are supported by a welded-in structure that is visible in Figure 2.8. The lower portion of the integral containment support has a 13-mm catcher plate bolted to it. This plate supports the lower catcher and the lower transducer support (Figure 2.8). The upper catcher and the transducer support are bolted to the bottom of the turbine plate.

The catcher system prevents the rotor from contacting the transducers during "mild" excursions and saves the rotor and chamber in the event of

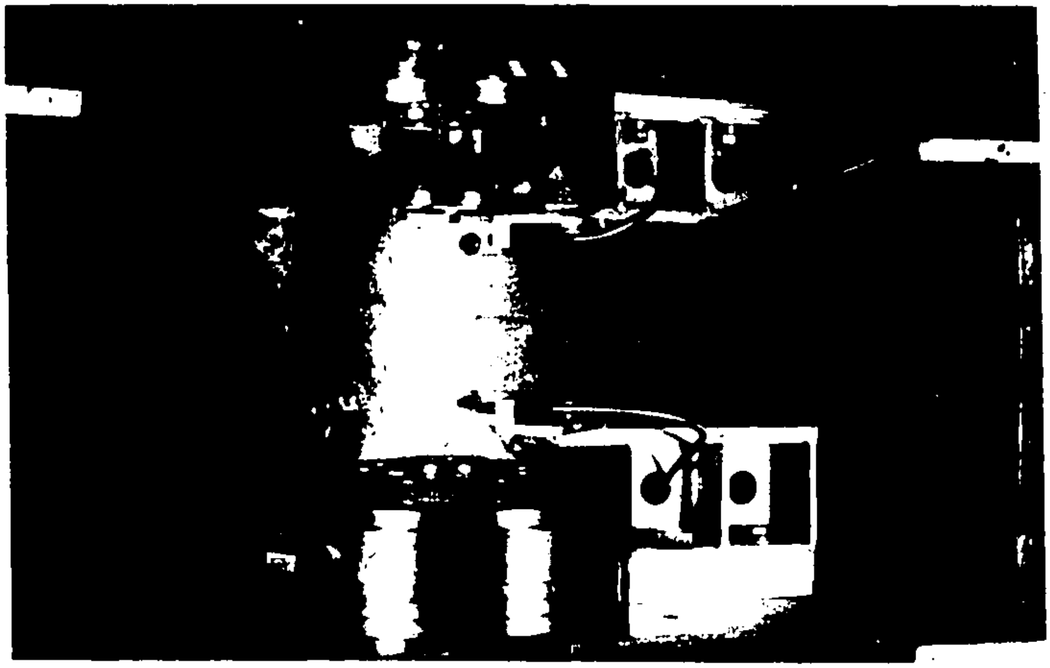

Figure 2.8: Catcher and Transducer Installation. The lower catcher is bolted to the catcher plate which is fastened to the lower containment support. The upper containment support is visible behind the upper catcher.

"extreme" rotor excursions. On several occasions, small and large rotors have contacted the catcher(s) with no damage resulting because the event occurred at low speed. During one high-speed, small-rotor test involving only the upper catcher and transducers, rotor contact did destroy the probes but the catcher limited the excursion and saved the rotor. During test FW3-1/1, an imbalance in the large rotor brought it into contact with the catchers, destroying the transducers and eventually breaking the shaft. The catcher system in this case saved the rotor with a few superficial gouges in the hub and, more importantly, prevented major damage to the chamber itself.

2.3.2 Drive System

Experience with the original drive system dictated that its successor incorporate external shaft damping and have as few couplings as possible. The Barbour Stockwell 2702, four-inch, bidirectional, impulse air turbine (Figure 2.9) satisfies these requirements. In order to accommodate the shaft-damping system, the spindle (or quill) shaft mounts inside the turbine rotor, thus reducing the overall axial length of the drive system and eliminating all but one coupling.

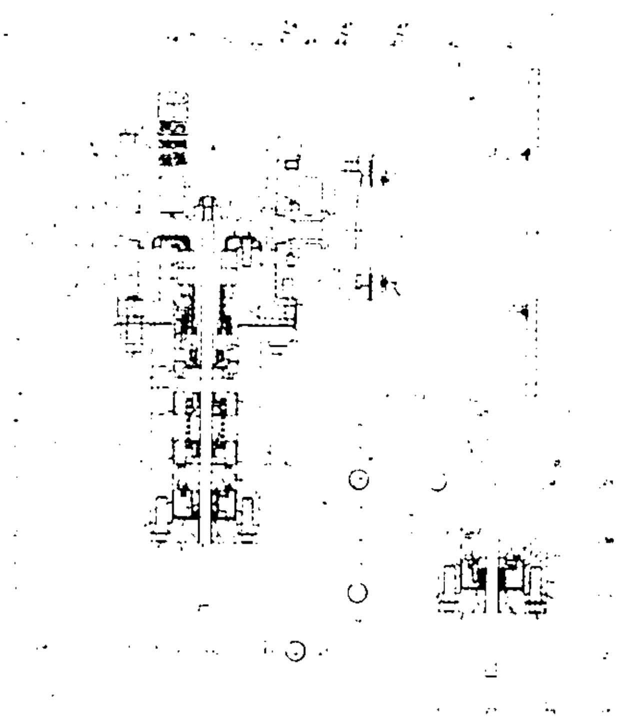

Figure 2.9: Four-Inch Bidirectional Turbine Section

The horizontal 5-cm plate that forms the floor of the turbine well supports the turbine and contains three viewports. To facilitate removal and replacement of the turbine, studs rather than bolts are used to secure the turbine and quick-disconnect couplings are used for air and oil lines. Mobil DTE797 oil or equivalent is supplied to and scavenged from the shaft damper by a Barb-

Figure 2.10: Turbine Installation. One of the two viewports to the left of the turbine has a strobe lamp on it. The IR sensor is to the right. In order to fit this turbine to the chamber, the old (circular) turbine well was cut out and a new one, resembling a box, was welded in its place (Figure 2.7 on page 32).

our Stockwell SOL-124 hydraulic system. The supply oil pressure is remotely adjustable with a battery-powered dc motor-driven valve. This arrangement was installed because of the requirement to be able to increase damping quickly while going through a critical speed and to decrease it when not required, to minimize the oil resonant whip effect. Thermocouples are installed in the damper-oil inlet and outlet lines as close as possible to the turbine damper body in order to record the temperature rise of the oil as it passes through the damper. Dry air is supplied to the turbine by a Canadian Air Compressor Airscrew Model 8 compressor at 100 psig and 125 scfm located in the Colonel By Building, approximately 150 m from the turbine. It is carried by a 5-cm-diameter pipe and passes through a Balston compressed air filter before entering the turbine.

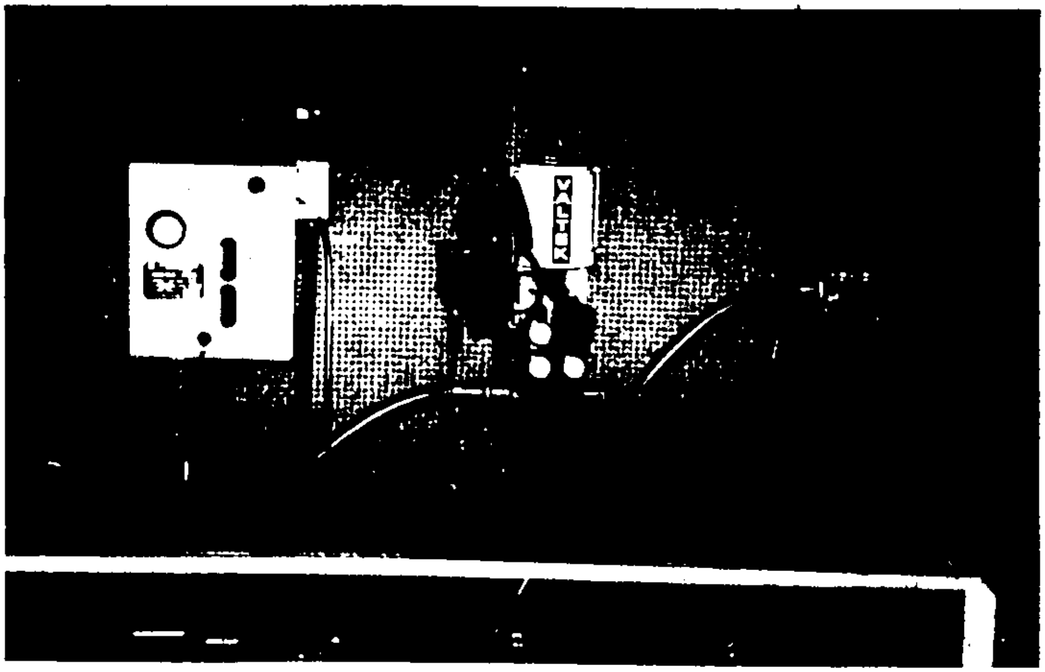

Figure 2.11: Valtek Unit. The turbine throttle valve is flanked by the mist lubricator (L) and two solenoid valves (R). The upper solenoid valve, just to the left of a globe valve, is the brake valve; the lower one is the main drive air cutoff valve.

Air to the turbine is regulated by a Valtek Mark Two, electric-pneumatic control valve (Figure 2.11). This proportioning valve is controlled by a potentiometer (throttle) on the turbine control panel (Figure 2.12). The Barbour Stockwell 105-E speed controller operates in a governed or ungoverned mode, the governed speed being set on a thumbwheel selector as a percent of the turbine's maximum safe speed. The box in the upper left corner of Figure 2.12 is the Barbour Stockwell 107-B Tachometer and Overspeed Control which contains a relay for shutting down supply air when the set speed is reached.

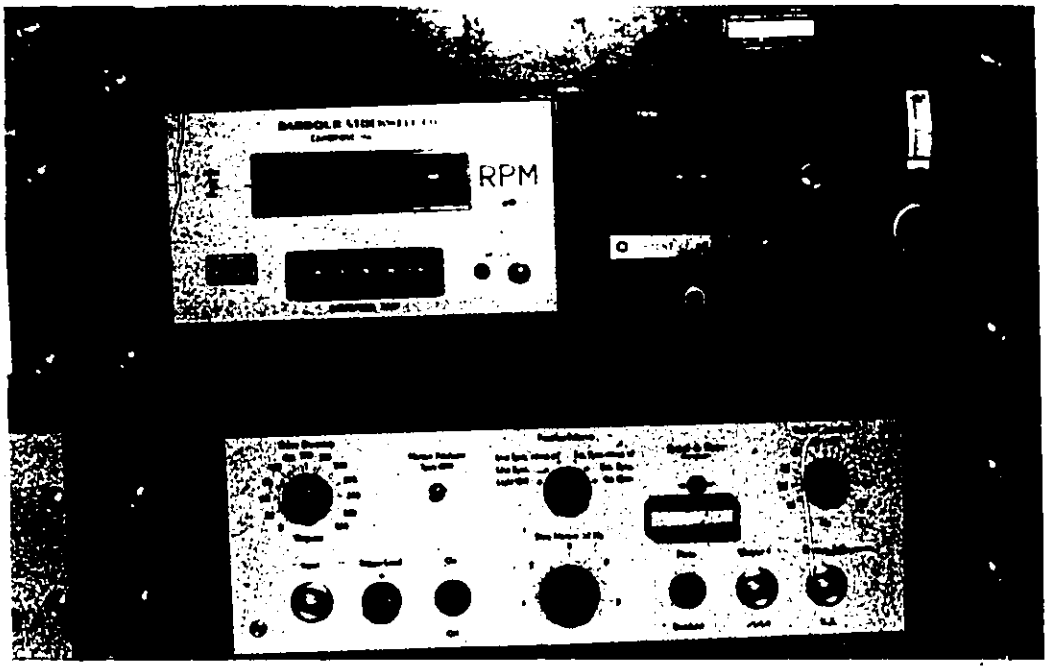

Figure 2.12: Turbine Panel. The turbine tachometer and overspeed trip control box occupies the left half of the turbine panel. The turbine throttle is the potentiometer on the right. The motion analyzer controller is below.

A solenoid switch and manually-adjusted globe valve control brake air supply. A main drive solenoid cutoff valve is interconnected with the vacuum pressure gauge and vibration monitor in order to shut down the turbine if pressure and amplitude limits are exceeded. These features were installed to permit unattended operation of the system.

The brake and drive air solenoids are interconnected such that selecting "brake" turns off the main drive solenoid, and vice versa, as shown in Figure 2.13, the schematic of the interconnect system.

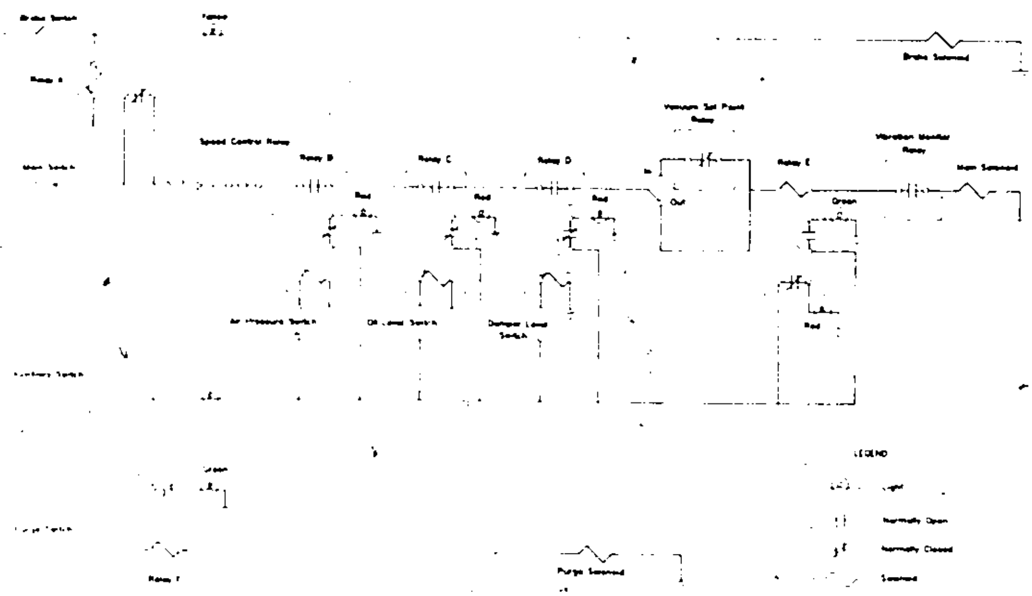

Figure 2.13: Interconnect Wiring Diagram

2.3.3 Vacuum System

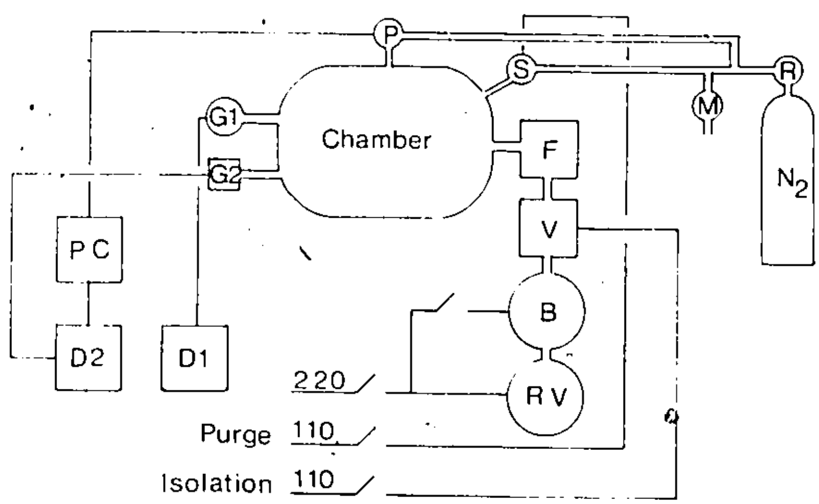

Figure 2.14: Schematic of Vacuum System. Legend: (F) filter, (V) electropneumatic valve, (B) Roots blower, (RV) rotary-vane pump, (G1) Pirani sensor, (G2) capacitance manometer, (D1) Pirani display, (D2) manometer display, (PC) pressure controller, (P) proportioning valve, (S) solenoid valve, (M) manual valve, (R) pressure regulator, and (N2) compressed nitrogen.

2.3.3.1 Pumps

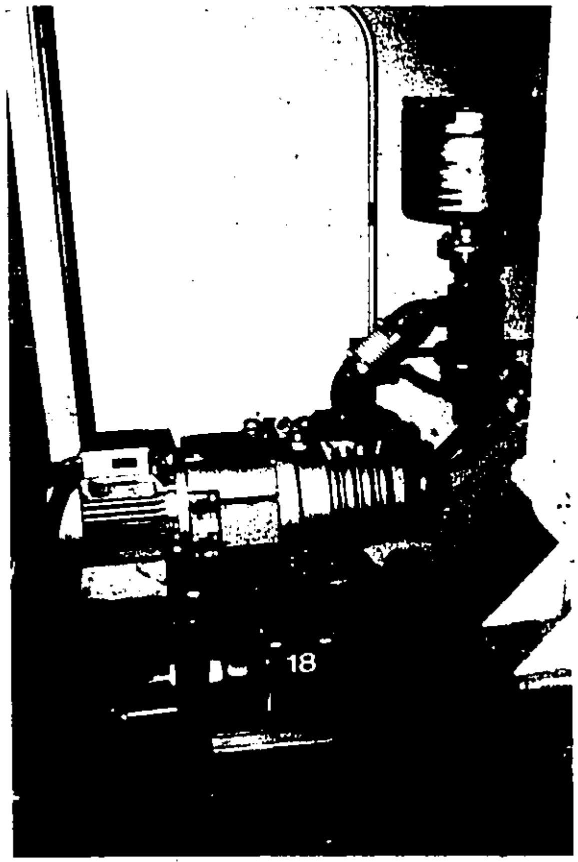

Figure 2.15: Vacuum–Pump Installation. Bottom to top: two–stage rotary pump, Roots blower, pneumatic valve, and inlet trap.

The complete vacuum system is shown schematically in Figure 2.14 on page 39. An Edwards High Vacuum Roots blower (EH250), backed by an Edwards E2M18 two–stage, rotary–vane pump (Figure 2.15) and connected to the chamber via an Edwards IT100 inlet trap and a Varian 1252 pneumatic valve, produces a tank pressure of 30 milliTorr in 20 minutes. The path between the chamber and pumps was made as short and straight as possible, in accordance with good vacuum practice.

The ultimate system pressure, with all leaks within the means of the author to repair sealed and the vacuum gauge calibrated, is 20 milliTorr. This pres–

sure is attributed to pumping limitations, to residual small real leaks, to virtual leaks (outgassing from crevasses, paint, oil, and composite materials), and to shaft-seal leakage. This ultimate pressure is reached after one hour of pumping time.

2.3.3.2 Gauges and Pressure Controller

The less accurate but full-range (atmosphere to tank ultimate) gauge used is a Granville-Phillips 275 Pirani type. A more sensitive Vacuum General CMT 80-6B capacitance manometer provides accurate pressure data from 1 Torr down to the tank ultimate. Moreover, this gauge supplies a signal to the Vacuum General 80-1 pressure controller which, in turn, operates a 79-6A magnetically-actuated proportioning valve to maintain chamber pressure at a preset level. As illustrated in Figure 2.14 on page 39, the pressure transducers are positioned as far as possible from the pump outlet.

The two reasons for installing the pressure controller were: to maintain a tank pressure above ultimate by bleeding in nitrogen, thus ensuring a nonexplosive atmosphere, and to measure aerodynamic drag and heating effects at different chamber pressures.

The vacuum gauge displays, pressure controller, and pump controls are shown in Figure 2.16.

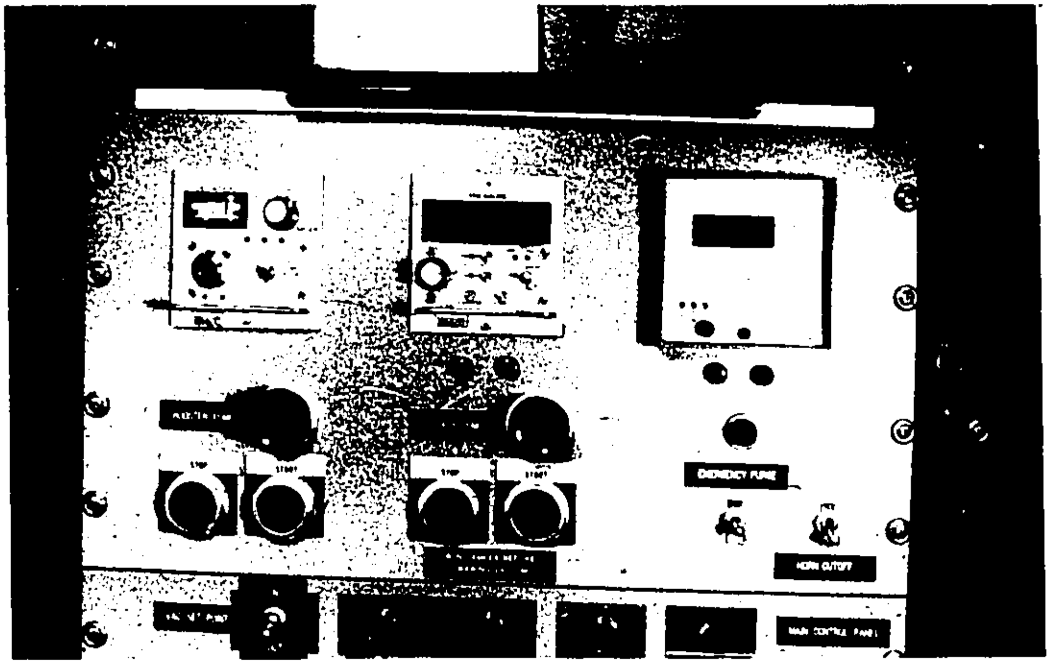

Figure 2.16: Vacuum Control Panel. Left to right: pressure controller, Vacuum General and Granville-Phillips displays. The displays have banana-plug receptacles beneath them.

2.3.3.3 Nitrogen-Purging System

The graphite-oxygen mixture resulting from a carbon-ring failure is potentially explosive. To minimize the possibility of explosion, nitrogen is bled into the chamber, by means of the proportioning valve, for one hour prior to test.

The chamber can be rapidly brought to atmospheric pressure by means of the 1.9-cm line between the nitrogen bottles and the chamber shown schematically in Figure 2.14 on page 39.

2.3.3.4 Vibration Monitoring System

Figure 2.17 is a schematic representation of the vibration monitoring and data acquisition system.

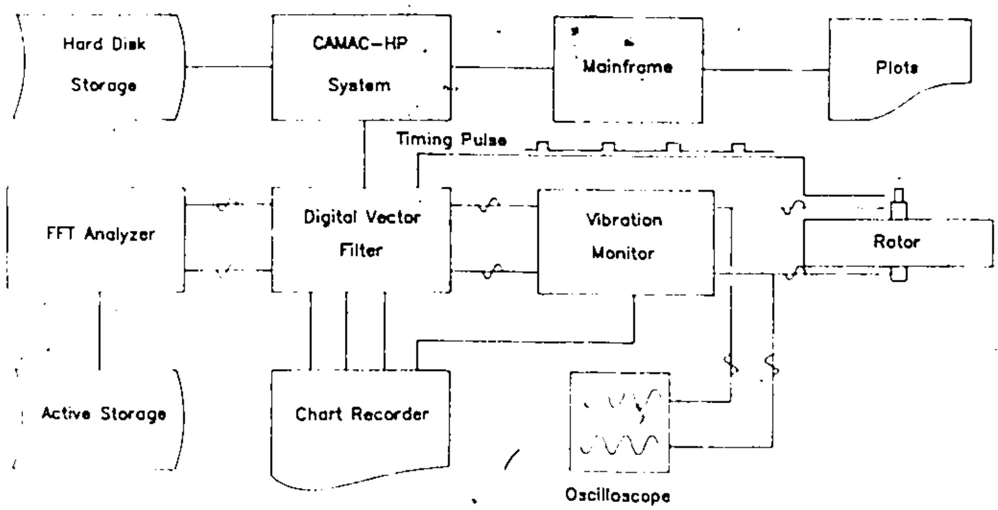

Figure 2.17: Vibration–Monitoring and Data–Acquisition System Schematic

- MONITORING SYSTEM

A Bently Nevada 9000 Series system comprising a rack, power supply, relay modules, display module, and two dual-channel monitors is located in the control console above the DVF2 (Figure 2.18). This unit powers the displacement transducers, monitors their condition, displays unfiltered amplitudes, generates dc voltages proportional to the unfiltered amplitudes, and activates interlock or annunciator relays according to preset alert or danger levels.

The displacement transducer installation is shown in Figure 2.19.

- TRACKING FILTER

A Bently Nevada DVF2 (Digital Vector Filter, Two-Channel), shown in Figure 2.18, filters the vibration signals from transducers in planes 2.5 cm above and below the rotor, with either a 120-rpm or 12-rpm bandpass, and displays filtered, unfiltered, or notch amplitudes, phase angles, and rpm. The DVF2 accepts displacement, velocity, and acceleration inputs, and displays

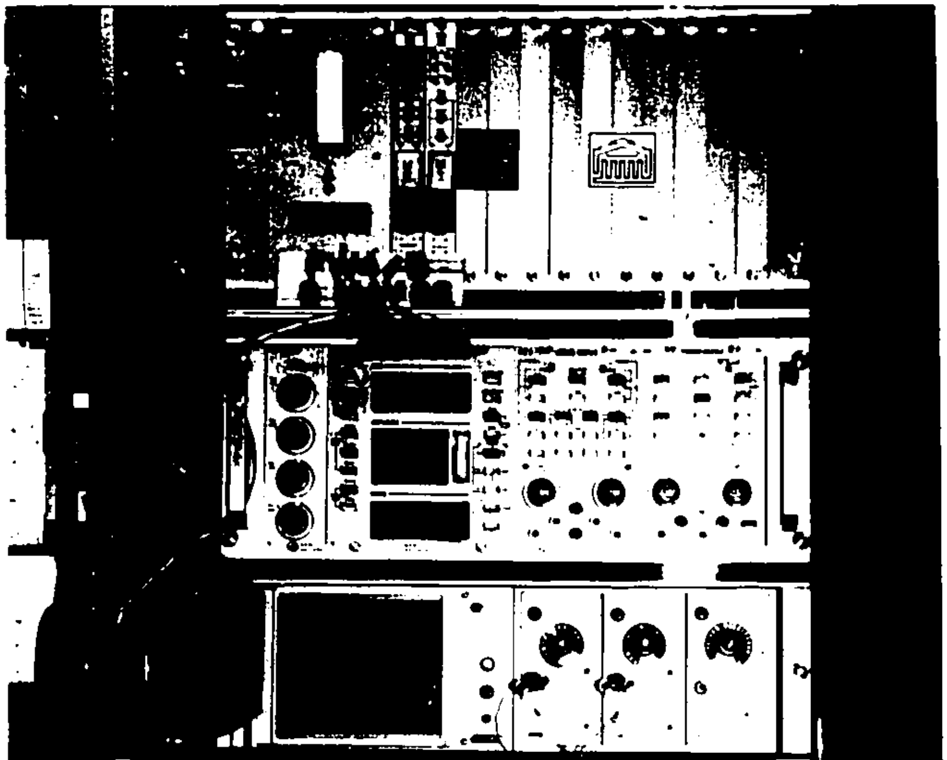

Figure 2.18: Right Console. Top: vibration monitor crate. Center: DVF2. Bottom: oscilloscope. The test/date plate and time of day clock are in the center.

amplitude units in English (mils) or metric (micrometers). It also produces proportional dc rpm, filtered amplitude, and phase angle voltages.

Since it is essential to maintain a fixed phase reference for rotor balancing, the timing signal for the DVF2 is derived, via a third transducer, from a notch in the upper, narrow section of the arbor. In the early phases of STF development, aluminum tape was used instead of a notch but this practice was abandoned because it did not produce a pulse large enough to be distinguished from the sinusoidal rotor-motion signal that was also being seen by the DVF2 timing circuit e.g., during whirling caused by oil resonance. The arbor timing pulse was also used to fire the motion-analyzer strobe lamps, but was later replaced with a signal derived from

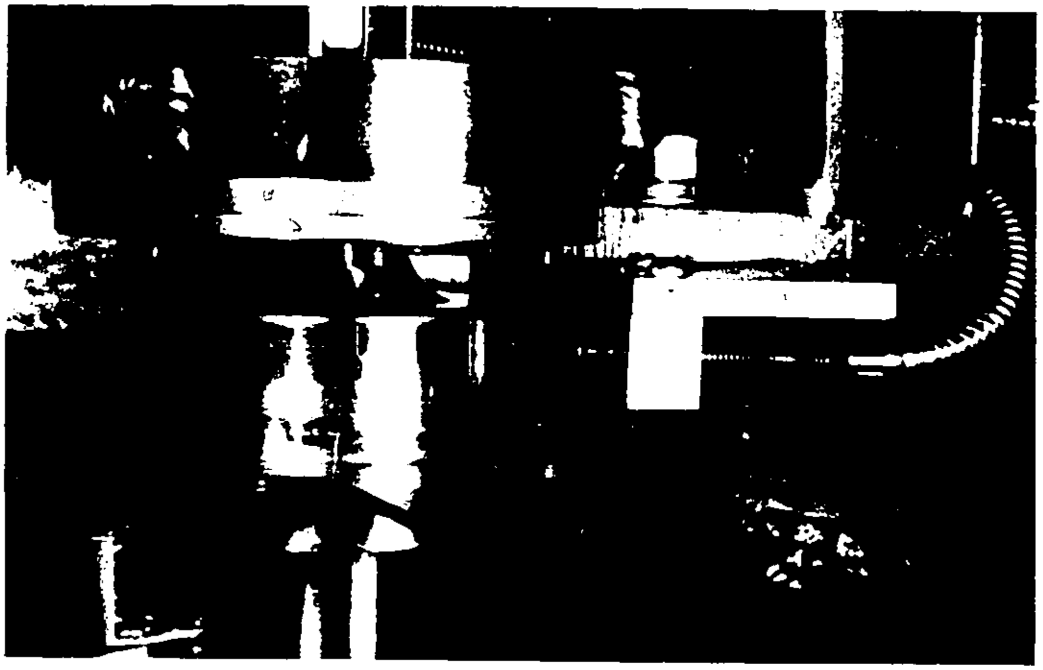

Figure 2.19: Displacement-Transducer Installation. One of the two upper-plane orthogonally-mounted transducers. The nominal probe gap is 1.10 mm. Note the upper catcher and the burnished target surface. The rotor is FW4-1. The timing notch is just visible above the catcher.

the six-pulse-per-revolution turbine tachometer by means of a divide-by-six circuit.[8] This was installed in order to have a square, once-per-revolution timing signal free of any noise.

Any rotor operating at a low speed (100 rpm) exhibits an apparent amplitude and phase angle due to shaft bow, misalignment, tolerance build up, and electrical noise. The DVF2 has an internal compensatory circuit to null this illusory motion, at low speed, in order to produce a more accurate representation of the rotor's actual displacement and phase angle at higher speeds.

---

8 Courtesy of Ben Carrara and Mohammed Master, Department of Electrical Engineering, University of Ottawa.

- SIGNAL ANALYZER

An Ono Sokki CF-920 mini FFT is used to analyze and store vibration spectra, in two channels, during tests. This device stores 30 records in active memory and 130 records per floppy disk. Data are stored directly onto disk at frequent intervals (200 rpm) during tests. The low acceleration rate required for this is quite compatible with the low-acceleration-rate strategy employed for most tests. While data are being recorded, the FFT CRT displays spectra for both channels, in near real time, providing additional data for decision making.

Post-test, stored data are down-loaded to the Amdahl mainframe by means of the HP1000 minicomputer for plotting, although intermediate plots are obtainable with a Graphtec WX4731 plotter connected directly to the Ono Sokki.

- CHART RECORDERS

The primary chart recorder, an NEC San-Ei 8K20, six-channel, thermal-pen device, is located centrally in the equipment rack (Figure 2.20) and is used to record unfiltered and filtered amplitudes, phase angles, and rotor speed. A second chart recorder (Gould 2400 four-channel, thermal-pen unit provides two addition channels for analog recording of vibration signals and two thermocouple channels for damper-oil temperature measurement.

- OSCILLOSCOPES

A Tektronix 5111A dual-channel, storage oscilloscope with 5A15N amplifier, 5A20N differential amplifier, and 5B10N time base is located below the DVF2. It either displays the rotor's orbit in one plane, or the sinusoidal waveforms for both planes. In either case, the oscilloscope CRT is included in the video insert (see below). In addition, a Tektronix C5C camera may

Figure 2.20: Center Console. The San-Ei chart recorder is located above the turbine control panel.

be used to record orbit or waveform images from the storage oscilloscope.

2.3.4 Audio-Visual (AV) Monitoring System

Figure 2.21 gives a schematic representation of the AV system components and their functions.

One Sony AVC 3200 camera is used to view the rotor and a second views the DVF2 display and oscilloscope CRT. The two views are combined by means of a Vivcon Industries V27SP inserter/splitter. Control-room and chamber audio are mixed with a Sony MX510 audio mixer and the resultant audio/video recorded on videotape with a Sony SL-5800 VCR. This recorder

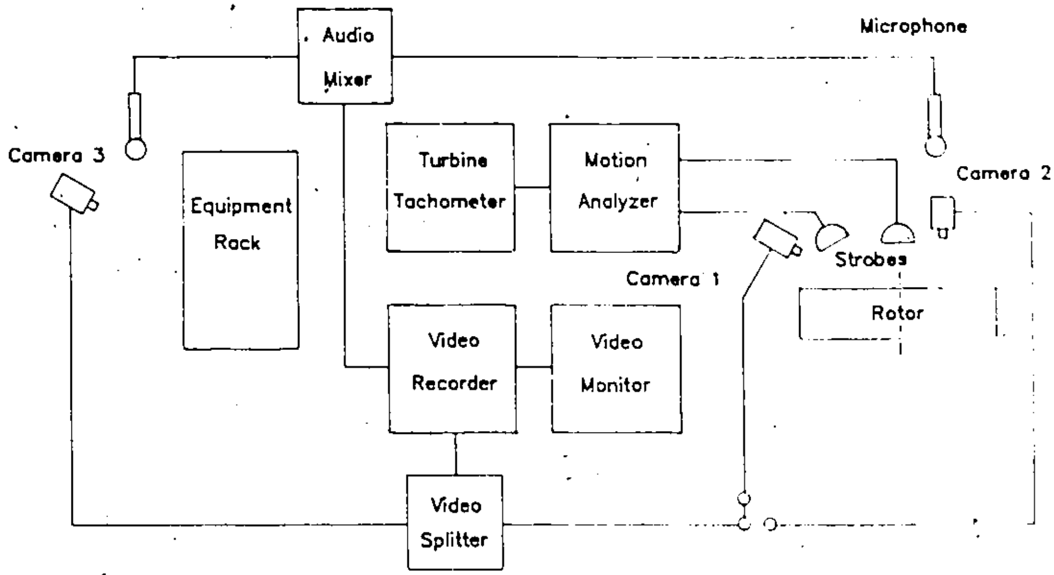

Figure 2.21: Audio–Visual System Schematic

excellent slow–motion and stop–frame features, enabling the quality still photography shown in Figure 2.22.

A third camera (RCA TC 2000) with a rack–mounted vidicon tube is used for macrophotography of rotors from the topside, vertical–axis viewport. A second VCR (Sony SLZ300) can be used for second–camera recording.

Video images are viewed with an Electrohome EVM1719, 17–inch monitor with audio–amplifier option, mounted in the equipment rack and/or with a nine–inch, RCA TC1109.

The rotor is illuminated by a pair of strobe lamps controlled by a Bruel and Kjaer Type 4911 motion analyzer. This device not only "freezes" rotor motion but, with phase control, allows inspection of any part of the rotor in the camera's field. The reference signal to the analyzer, as stated previously, is derived from the turbine tachometer.

Figure 2.22: Video Monitor Display. A still photograph of FW3-1 at 17,049 rpm on August 21, 1985, at 3:03 pm.

2.3.5 Temperature Monitor System

The rotor's temperature is remotely measured with an Ircon Inc. Modline 8000 Series infrared sensor, as shown schematically in Figure 2.23. The sensor itself (Figure 2.10 on page 36) is mounted on a column containing primary and backup calcium fluoride windows. These windows are virtually transparent in the sensor's 7.75 to 8.05 micron spectral response region.

The viewed area of the sensor is a 2.5-cm-diameter spot, 20 to 30 cm from the rotation axis. The sensor lens is located 50 cm above the rotor and has a temperature range of 20 to 200 degrees C. Temperature is displayed in analog form by the controller which also produces a proportional dc voltage for recording purposes.

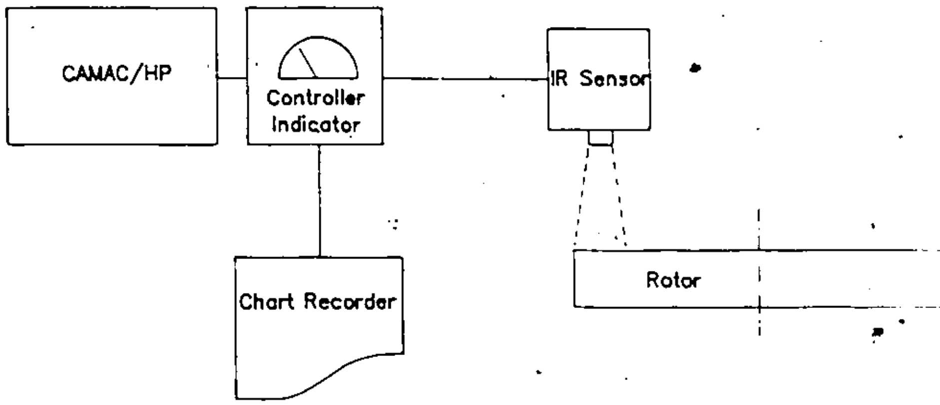

Figure 2.23: Schematic of Rotor–Temperature Measurement System.

2.3.6 Computer System

The STF computer system is shown schematically in Figure 2.24. During high-speed tests, the LeCroy 8212 digitizer, controlled by a Digital LSI 11/23 micro-computer, digitizes analog filtered–amplitude, rpm, and phase data from the DVF2 dc outputs and stores these on a Winchester hard disk. Post-test, these data are down-loaded to the Amdahl mainframe.

Control software is also available for cyclic testing of rotors. In this mode, the microcomputer switches drive and brake solenoids by means of a Kinetic Systems 3080 eight-bit output register.

The micro- and minicomputers are located in the adjacent Fuels Research Laboratory and accessed from the STF control room with a TeleVideo 925 terminal.

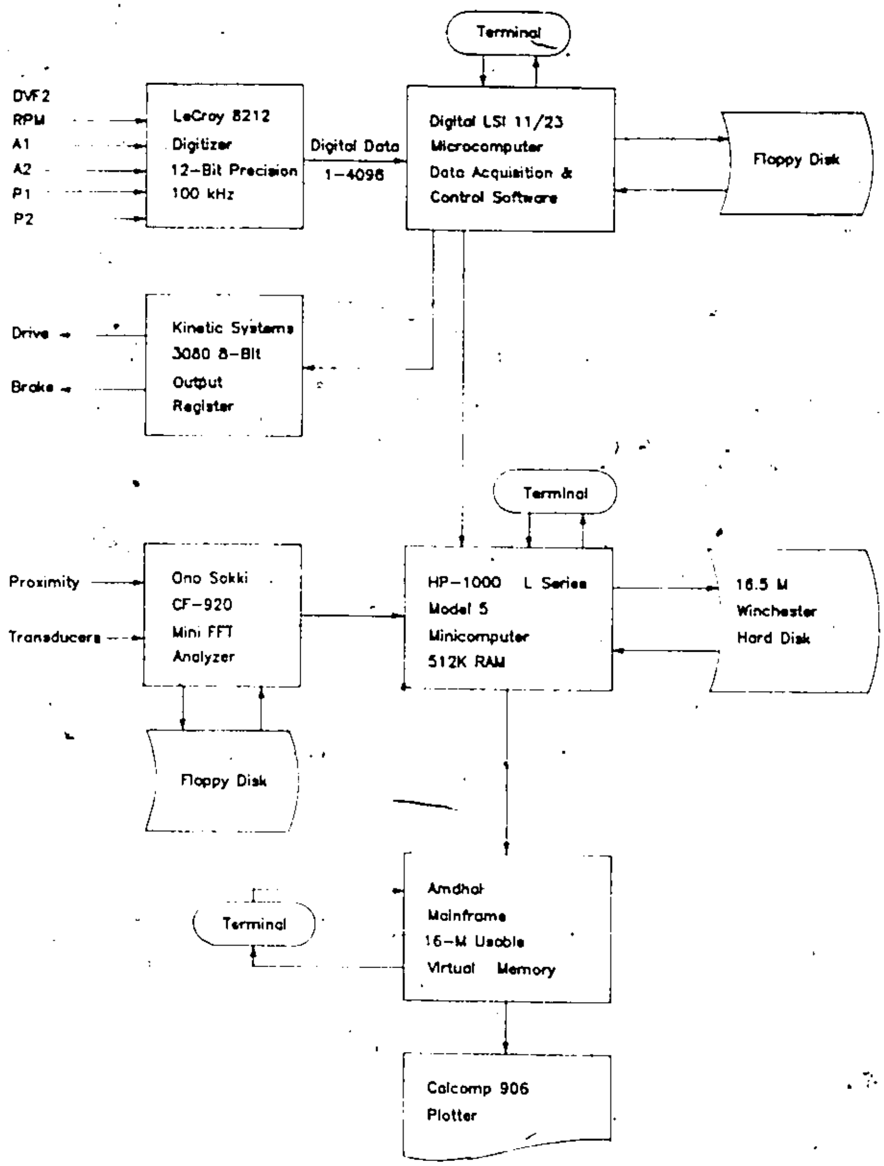

Figure 2.24: Schematic of Computer System

2.4 Summary

In this chapter, an overview of the Rotor Project prior to the research period for this thesis has revealed that the Spin-Test Facility required a significant upgrading in order to support the testing required by the Project. In spite of the deficiencies that centered on the drive and monitoring systems, a substantial number of tests were run, producing useful data and invaluable operator experience.

The outline of the research period was written in terms of the thesis objectives which, briefly again, are:

1. STF development
2. ESR component tests
3. Material-strength tests
4. Large ESR performance tests

In summary, STF development met or exceeded the Project requirements in terms of speed, vibration-control, and data collection; all ESR component tests and material-strength tests were carried out successfully; and all of the large ESR tests were performed satisfactorily. However, one of the four rotor designs was not tested to high speeds due to tilt and eccentricity imparted by the hub. The minimal damage resulting from a 1.3-kWh-rotor failure attests both to the soundness of the STF development and the safe-failure-mode design philosophy adopted in the Project.

Finally, a detailed equipment list and system description were given to familiarize the reader with STF capabilities. Although not fully exploited by the research for this thesis, the laboratory will, as an on-going research facility, be utilized to its fullest, performing rotor drag and heating, cyclic stressing, and other experiments in the future.

Chapter III

GENERAL TEST PROCEDURES

Necessarily, rotor-testing procedures evolved during the development of the Spin-Test Facility. As new equipment was added, as higher rotor speeds were attained, and as rotors grew in size and energy-storage capacity, procedures were defined or redefined in order to maximize the amount of information extracted from each test. In this chapter, each aspect bearing on the procedure for spin testing a rotor is examined, from manufacture, to assembly, installation, balancing, and finally to the spin test itself.

3.1 Component Manufacture and Rotor Assembly

While the author participated to some extent in component manufacture and rotor assembly, these activities were the primary responsibility of others in the Project and are reported here as necessary background.

Rotor-design philosophy for this project, as spelled out in reference [45] was to build a fiber-composite rotor with the following parameters:

1. Usable energy storage of 0.75 to 1.0 kWh with a 2:1 speed ratio.
2. Maximum design speed of 25,000 rpm.
3. Maximum outside diameter of 61 cm.
4. Swept volume of 0.025 cubic meters.
5. Mass of 30 to 32 kg.

To meet these objectives, four rotor designs were selected from among several dozen candidates on the basis of perceived stability, cost, and manufacturability [53]. Rotor stability requires that interfacial pressure be maintained between hubs and rings, and between rings and rings. It also requires that radially dilating bolted components not produce intolerable stress levels throughout the speed range (compatibility requirement). More attention will be given to this subject in Chapter IV, but it is important to note here that these design requirements called for the highest precision machining available in order to minimize tolerance buildup.

Rotor assembly likewise called for stringent procedures in order to reduce misalignment between components to a minimum. The way in which these concerns were addressed is summarized in the following three generalized assembly histories.

1. COMPOSITE HUBS

The 100-Wh composite rotor (SMC or S2L) was a 27-cm-diameter by 2.5-cm-thick disk of material bolted to a single flex-rim attachment (FRA) with four bolts. The FRA in turn was attached to the arbor with four screws. The arbor/FRA components and bolts were fabricated by an outside contractor.

To center the FRA on the arbor, a shoulder was machined onto the FRA and a corresponding depression into the arbor. The holes in the hub were located with a jig and were drilled in from both sides to prevent hub delamination. Locktite (R) was used on all threads and the FRA bolts were tensioned sufficiently to compensate for the Poisson effect in the hub.

A 7.940-mm (nominal) quill shaft was fit into the 8.174-mm (nominal) bore in the arbor and secured with three self-locking set screws. To ensure minimum tilt, the rotor was clamped in a four-jawed chuck and the end of the shaft brought to zero deflection by adjusting the set screws. This rotor was then ready for installation in the test chamber.

2. METAL HUBS

The 100-Wh metal-hub rotors could not be tested to speed unsupported as the smaller FRA had been (Test FRA-1), nor was it desirable to do so because the behavior of the ring on the hub was an important part of the test. Consequently, a 2.5-cm-thick S2-glass ring was thermally-fit onto the hub.

The arbor pierces the hub in this case, simplifying the centering problem. For radial compatibility, a thermal fit between hub and arbor was also used, with a short tapered section to facilitate removal of the arbor. A large nut secured the thermally-fit arbor to the hub; an intermediate Belleville washer was used to compensate for the Poisson effect in the hub and, again, Locktite (R) was applied to the threads.

For this rotor, concentricity depends upon machining accuracy which is not a problem for the arbor as much as for the FRH itself. The FRH, being machined on a numerically-controlled mill, presented special problems because the thin rim and spokes can be easily deflected by the milling tool. Thus, while the hub outside diameter and central bore could be made fairly concentric, the shape and location of the quadrants are more difficult to control, resulting in some off-specification thicknesses.

The ring or rings were fitted to the FRH by cooling the hub in liquid nitrogen, the same technique used to fit arbor and hub together. The hub and ring(s) were set on parallel faces, while the hub warmed up, to ensure no tilting of the ring with respect to the hub. Prior to assembly, all rings required machining of at least the outside diameter.

The spring-spoke hub (SSH) rotor assembly is similar to that of the FRH for the arbor and hub but, prior to that step, the hub itself is assembled inside a ring (or rings). The procedure for installing the spring spoke plates in the thermally-fitted, grooved aluminum inset ring for SSH-1 is illustrated in Figure 3.1. Once assembled, the small metal-hub rotors are ready for installation in the chamber.

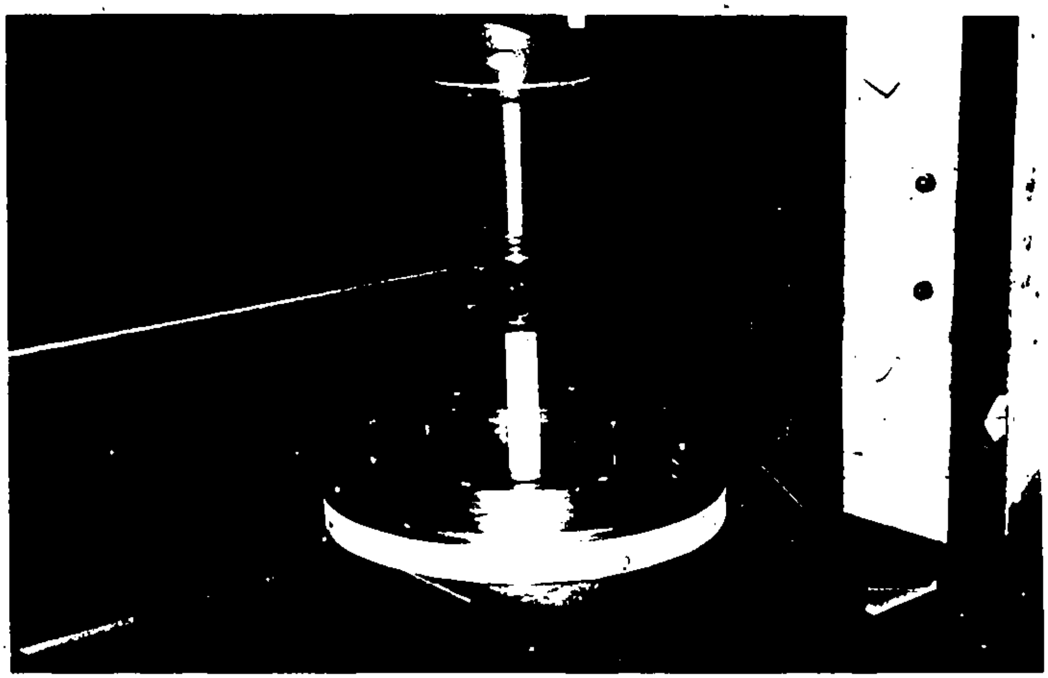

Figure 3.1: Rotor SSH-1 Assembly. The SSH spoke plates, made from maraging steel, then heat-treated, must be compressed as shown in order to fit into the ring.

3. LARGE ROTORS

The same principles apply to the assembly of the large rotors, but with one additional complicating feature. Because of the real possibility (later to become a reality) that a large rotor could go out of balance and break its shaft, saving the rotor and protecting the chamber was given serious consideration.

The small rotors are constrained from moving more than 1 mm laterally by an upper catcher located just below the end of the quill shaft. The catcher comprises a bearing support and bearing with an inner race giving 1.02-mm radial clearance to the arbor. This constraint is sufficient to protect the transducers from light contacts by the arbor.

In addition to this system, the large rotors are each equipped with a lower fitting (termed a lower arbor) comprising a second displacement transducer target and conical end piece that rotates with 1.127-mm clearance inside the lower-catcher system.

The addition of the lower arbor to the metal-hub rotors was no problem, the components having matching centering shoulders and bores, but it did pose new problems for the composite hubs. In the latter case, a second FRA is bolted to the lower arbor, which is then bolted to the hub. Again, stud tension is set to compensate for the Poisson effect and all threads are coated with Locktite (R).

Whereas the small composite-hub rotors' diameters and thicknesses are small enough that variations in thickness are inconsequential, in the large rotors, they are of consequence. FW1-1 and FW2-1 required shims between the FRA and hub to correct for tilt between the arbor and carbon ring.

The axial thickness of the large composite-hub rotors and the use of two FRAs also introduces possibilities for misalignment between upper and lower arbors. Post-assembly grinding of the arbors was experimented with [51] as a means of eliminating the effect of misalignment on the rotor-monitoring system. This proved unnecessary in the end, however, when the tracking-filter capabilities for nulling out this type of artifact were employed.

3.2 Rotor Installation

Prior to rotor installation, the turbine damper is inspected for wear, and journal bearings and seals replaced as necessary. The turbine is then bolted into place and the verticality of its spin axis checked with a precision level. The threaded end of the quill shaft, which passes through the seal, three journal bearings, and the turbine rotor bore, is polished with fine sandpaper and thoroughly cleaned to prevent jamming by metallic particles when inserted. The well-lubricated shaft is then secured to the turbine rotor with a self-locking nut.

As mentioned above, the small rotors were always attached to the shaft before installation. For the large rotors, this was not practical and the attachment was made to the shaft after it had been installed in the turbine. This was accomplished, as shown in Figure 3.2, by inflating an inner tube beneath the rotor. With the rotor secured to the shaft by its set screws, the tube is deflated and removed. The rotor's tilt is then checked and adjusted by varying the torque on the three set screws.

With the large rotor installed, the lower catcher is bolted into position on the catcher plate and adjusted for 1.27 mm of radial clearance with the lower arbor. Finally, the lower transducer support is bolted into position and gaps adjusted to nominal values of 1.10 mm for the upper and 1.15 mm for the lower transducers.

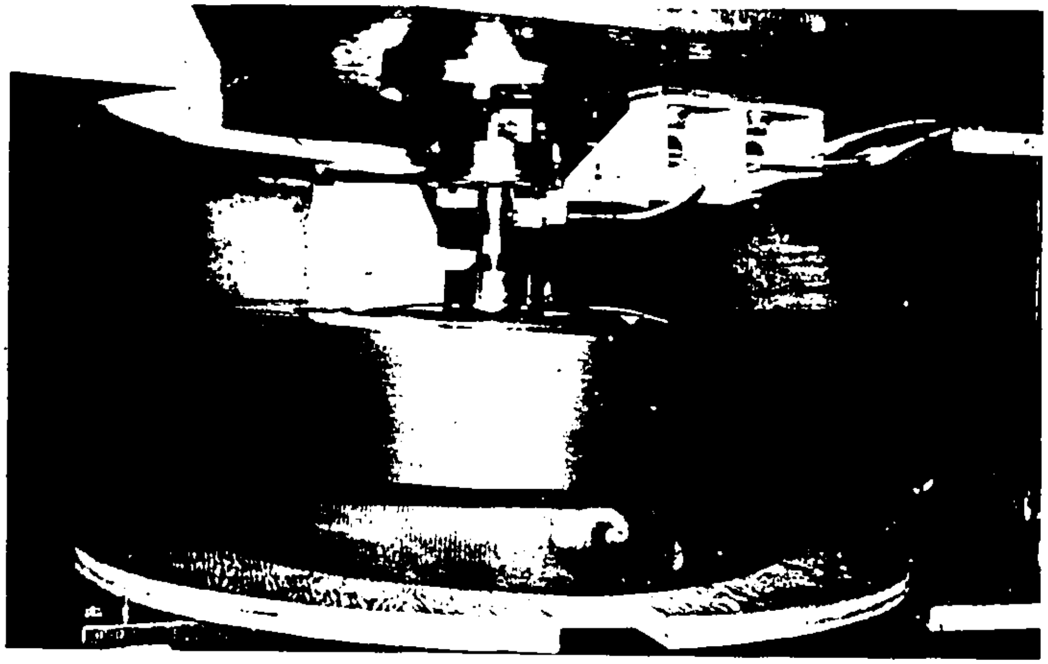

Figure 3.2: Raising Large Rotors. FW4-1 rests on a partially-inflated inner tube. The rotor has another 5 cm to travel before the set screws align with the groove in the quill shaft.

3.3 Balancing

The 100-Wh rotors' imbalance was determined using a single-plane, influence-coefficient method. Metal-tape correction weights were applied to the inside of the metal hubs, and material was removed from the outer edge of the composite-disk rotors.

With the 1-kWh rotors, there is sufficient balance-plane separation to permit application of moment correction weights. This requires that the static imbalance be removed first, using the static-couple derivation method which averages data from both planes [51]. With a pure moment imbalance remaining, as demonstrated by the residual amplitudes in the two planes being equal and 180 degrees out of phase, a two-plane influence-coefficient method can be used. Moment correction weights in the form of brass or copper plugs glued into holes near the edge of the composite hub and lead tape applied to the inner surface of the metal hubs were used.

All rotors were balanced at speeds well above first critical speed, usually 3000 rpm. For the large FRH rotor FW3, balance runs were carried out under vacuum after it was observed that the large, paddle-like spokes tended to produce aerodynamic excitation.

3.4 Testing

With the rotor balanced, transducer clearances and the security of their mountings checked, the viewports cleaned, and any loose objects removed, the door was bolted shut. Before drawing a vacuum, the damper pump was run briefly to put positive pressure on the rotating damper seal, and the vacuum pump fluid levels were inspected.

While the chamber was being evacuated, final checks were made of recording equipment, recording and sensitivity levels, air and oil quick-disconnects couplings, spin-axis verticality, control settings, turbine lubrication, and the nitrogen-purge system. If the test involved carbon fibers, the vacuum pressure controller was set at 30 milliTorr, a few milliTorr above the chamber's ultimate pressure, in order to allow nitrogen to bleed into the chamber, thus removing any residual oxygen. Usually, one hour was allowed at this pressure before spinning began.

Rotor speed is controlled manually by adjusting the throttle potentiometer (Figure 2.12 on page 38), and the first observation to be made is of the rotor's response at balance speed, under vacuum, to compare with its ambient-pressure response. By the end of the research period, data were being recorded as noted below:

1. Chart Recorders

a. Filtered and unfiltered amplitudes.

b. Speed and phase angles.

c. Chamber pressure.

d. Damper-oil and rotor temperatures.

2. Video/Audio (see Figure 2.22 on page 49)

a. Rotor image.

b. DVF2 display (rpm, amplitude, phase angle).

c. Test data plate (test number, date).

d. Time of day.

e. Oscilloscope orbit or waveform display of rotor motion.

f. Control-room commentary and turbine audio.

3. Signal Analyzer (FFT)

a. Digitized spectral data for both planes at 200-rpm intervals.

4. CAMAC System

a. Filtered amplitude, two channels.

b. Phase angle, two channels.

c. Rotational speed (rpm).

d. Elapsed time.

The instruments that give the operator the most immediate feedback on the rotor's performance are the chart recorders and oscilloscope; the chart recorder gives prompt indications of amplitude trends and the oscilloscope display magnifies every perturbation of the rotor by a factor of 5000.

A rotor's first high-speed test required at least three people:

1. one to manually control the rotor drive system,

2. one to control the data-acquisition system and data-collection sequence, and

3. one to assess overall rotor dynamic response from the various displays.

The last individual was also responsible for reading checklists, particularly in the event of an emergency such as gross rotor imbalance or shaft failure.

At rotor failure, or upon reaching a limiting amplitude or the desired maximum speed, the brake air valve was opened, automatically closing the drive-air main valve (see the interconnect wiring diagram, Figure 2.13 on page 39). The electric-pneumatic valve isolating the pumps from the chamber either would have been closed at burst by an amplitude-activated relay, or by the operator a short time prior to the expected failure speed.

Following the burst tests, the chamber was not disturbed for a few hours to allow the dust to settle before opening the door. All data, including debris, were properly identified for later retrieval and examination.

3.5 Instrument Accuracy/Calibration

Tachometers

Two tachometers are used for speed measurement: a DVF1 and a DVF2, both manufactured by Bently Nevada Corporation, Minden, Nevada, who provide the following rpm accuracy specifications:

- DVF1: 0 to 36,000 rpm, +/- 1 rpm; 36,000 to 72,000 rpm, +/- 1%
- DVF2: 0 to 10,000 rpm, +/- 1 rpm; 10,000 to 100,000 rpm, +/-0.01%

The DVF1 (an obsolete unit) was donated by the manufacturer and served until the purchased DVF2 was installed. Only one material test was based on the DVF1 tachometer.

The turbine, DVF1, and DVF2 tachometers were checked against the CAMAC's internal 6250-Hz pulse generator with the results appearing in Table 3.1.

Table 3.1: Tachometer Calibration Results

CAMAC (rpm)	Turbine (rpm)	Error (%)	DVF1 (rpm)	Error (%)	DVF2 (rpm)	Error (%)
54,358	54,360	0.00	53,645	1.31	54,333	0.05
48,344	48,340	0.01	47,761	1.21	48,340	0.01
42,345	42,345	0.00	41,975	0.87	42,342	0.01
36,333	36,330	0.00	36,112	0.61	36,332	0.00
30,322	30,320	0.01	30,142	0.59	30,323	0.00
24,311	24,310	0.00	24,270	0.17	24,315	0.02
18,300	18,300	0.00	18,224	0.42	18,300	0.00

This table supports the manufacturer's specification for the DVF2 throughout the evaluated range and for the DVF1 only up to 45,000 rpm.

Amplitude

No amplitude accuracy specification is given by the manufacturer of the DVF2, although each transducer is factory calibrated. Since the instrument was returned for faults on two occasions, and was recalibrated both times, the amplitude accuracy was taken to be that of the digital display, i.e., +/-0.1 mil, high range, and +/-0.01 mil, low range.[9]

Vacuum Pressure

The capacitance manometer was selected, in part, because of its ruggedness and ability to retain its precision (0.15% of reading) over long periods. The only user requirement is the zeroing of the manometer output at a very low pressure (1 nanoTorr) and adjusting the display unit to read the same as the manometer output voltage. The zeroing was carried out once per year on a diffusion pump in the University of Ottawa Department of Physics and

9 The DVF2 displays peak-to-peak amplitude values.

checked with a 5 1/2 digit Hewlett-Packard precision multimeter.

Speed Determination

As described in Section 2.3.5, a video record was made simultaneously of both the rotor and the tracking-filter tachometer display. To determine the speed at which a rotor failure has occurred, the frame-by-frame feature of the video recorder is used to count frames between tachometer updates. The video scan rate is 30 Hz and the DVF2 tachometer update period is one-half second. Therefore, since acceleration rates are held fairly constant, it is possible to fix a failure speed by linear regression.

3.6 *Summary*

In this chapter, the manufacture and assembly of rotors has been reviewed to gain an appreciation of their impact on spin testing. Each rotor in this program has its strengths and weaknesses in terms of potential for misalignment and consequent static/couple imbalance. The composite rotors, for example, require the accurate location of four holes to correctly center the arbor while the arbor for the metal hubs is located by a more-accurately placed central hole. There are other factors that touch upon the purely convenient: for example, the metal-hub rotors are corrected for imbalance by adding weights that can be easily removed. The composites have to have material removed and are therefore permanently affected by their balance corrections.

With the rotor assembled and installed in the chamber, the balance procedure was introduced and then the general test procedures were reviewed. The significance of reviewing these procedures was to demonstrate the care that must be taken in order to carry out safe, successful, high-speed spin tests.

Chapter IV

100-WH-ROTOR TESTS

4.1 Introduction

As set down in Chapter I, the University of Ottawa Energy-Storage Rotor Project objectives were the design, fabrication, and testing of a 1-kWh fiber-composite rotor. To reach this objective, four rotor designs were worked up and, in order to select one of them as the final rotor, five scale-rotor tests were designed with these objectives:

1. Evaluate the flex-rim bolting attachment system for solid composite disks.
2. Prove the feasibility of through-drilling composite-hub material for shaft attachments.
3. Obtain composite-hub biaxial-strength data.
4. Measure the radial strength (i.e., strength radially transverse to the fiber direction) of a circumferentially wound carbon/resin ring under dynamic loading.
5. Acquire and interpret performance and vibration data for specially-designed radially-expanding metallic hubs.
6. Evaluate rotor design, residual stress, and manufacture and assembly procedures and analyses developed through the testing of the prototype rotor.

This chapter is divided according to the three fundamentally different types of rotor tests:

1. composite rotors,

2. metal-hub rotors, and

3. the prototype rotor.

The first segment deals with the tests conducted to obtain the ultimate biaxial strength of SMC and S2-glass laminate (S2L) materials, the second with the ring-radial strength (RRS) prototype rotor test, and the third with the metal-hub experiments. Included in the SMC and S2L segment, there is a test of the flex-rim attachment to characterize its balance quality as a rotor component and its unsupported dynamic behavior. Thus, all experiments in the first two sections were direct or indirect tests of the bolted FRA system.

The immediate result of the prototype-rotor test was an experimentally-determined value for the radial transverse strength of the wet-filament-wound fiber-composite ring. According to the literature, this was the first test of this kind to be conducted. More importantly, this test was an evaluation of the entire ESR program: it was to prove out the design, residual-stress analyses, and manufacturing and assembly techniques. The decision to proceed to final rotor manufacture rested on its outcome.

The metal-hub segment deals with the collection of vibration and performance-evaluation data for the flex-rim and spring-spoke hub (FRH and SSH) rotors in order to determine the intrinsic stability of these designs.

Physical parameters for all rotors tested appear in Table 4.1

Table 4.1: 100-Wh-Rotor Physical Data

Rotor	Diameter (cm)	Mass (kg)	Inertia (1) ($kg-m^2$)
FRA-1	16.00	0.89	0.001
SMC-1	26.04	3.16	0.020
SMC-2	26.77	3.23	0.022
S2L-1	27.98	3.93	0.030
S2L-2	27.94	3.79	0.029
RRS-1	41.93	6.77	0.127
FRH-1	30.55	3.13	0.027
SSH-1	30.55	4.88	0.025
SSH-2	43.25	7.78	0.127

Note: (1) Polar mass moment of inertia.

4.2 Composite-Rotor Tests

4.2.1 Introduction

The composite rotors tested, together with the test objectives, were:

1. FRA-1: dynamic test of an unsupported flex-rim attachment.
2. SMC-1: biaxial strength test of an SMC[10] disk and failure-mode analysis (effect of holes).
3. SMC-2: as for SMC-1, plus effect of fatiguing.
4. S2L-1: biaxial strength test of an S2-glass-laminate[11] disk.
5. S2L-2: as for S2L-1, but with the disk weakened to reduce failure speed.

[10] Supplied by the Owens-Corning Fiberglas Corporation, Granville, Ohio.

[11] Supplied by the Owens-Corning Fiberglas Corporation, Granville, Ohio.

4.2.1.1 Drilling of Composites and FRA Evaluation

Heretofore, the attachment of composite disks to shafts has been by elastomeric bonding. Although this method has served the immediate spin-testing requirements of those using it, there have been bond failures and some suspicion that the elastomer itself causes rotor instability. Notwithstanding the two long-term cyclic tests carried out at ORFEL with elastomerically-bonded arbors [12],[12] the ESR Project opted for bolting since the objective was to build rotors suitable for real-world applications. Although bolting has been studied by at least one other group, General Electric [54], they did not actually test the idea because the great emphasis on achieving the very high burst energy of 80 Wh/kg in the US MEST program precluded such experimentation.

The device invented at the University of Ottawa to minimize the weakening effect of holes is called a flex-rim attachment (FRA), shown in Figure 4.1, and is designed so that the radial displacement of the bolt holes in both the FRA and the hub, due to centrifugal force, will be the same throughout the rotor's speed range. Moreover, the hole diameters and their radial locations in the composite disk are such that the stresses near the holes are less than the stress at the center of the disk because of positional and hole-size effects that occur only in composite materials.

---

12 Two 10-kg rotors were cycled between 50 and 100% of their design maximum speed 10,000 times.

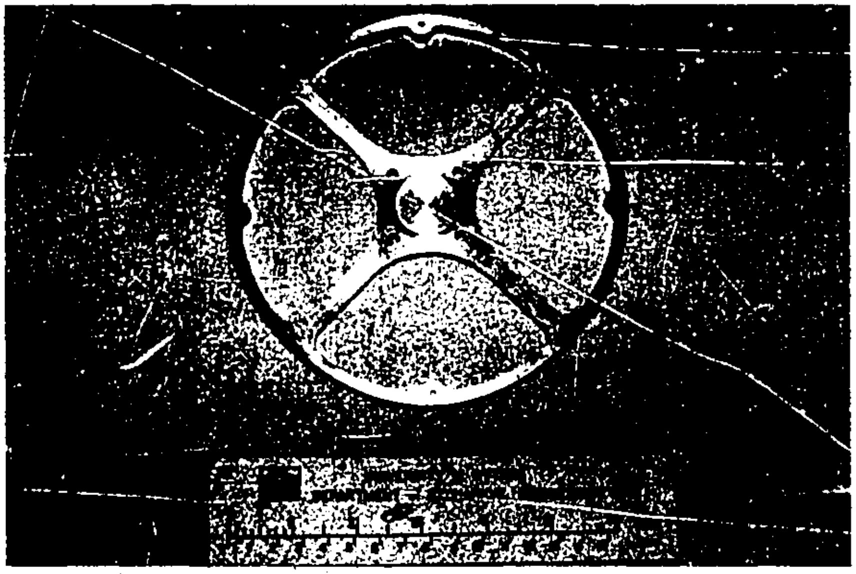

Figure 4.1: Flex–Rim Attachment

4.2.1.2 Biaxial Strength Measurement

It has been shown by Daniel [55] (Figure 4.2) that laminated graphite/epoxy plates are stronger under biaxial stress than they are under uniaxial stress conditions. If S2–glass/epoxy laminates were to behave in the same way, the material supplied by Owens–Corning would prove to be stronger under biaxial loading than its accompanying ultimate tensile strength data.

Support for this idea was found in the work of Nuismer and Whitney [56] who performed a series of tensile tests on carbon/epoxy and S2–glass/epoxy laminates with round, through–the–specimen holes of varying diameters. Table 4.2 summarizes the data taken from Figures 9 and 11 of their monograph and illustrates how similarly the two (0,+/–45,90)2s laminates behave. This parallel behavior justifies the application of Daniel's carbon–laminate hole-size data to S2–glass laminates with the same layup sequence.

Extrapolating Daniel's data in Figure 4.2, the strength reduction expected for a 3.175–mm (0.125–in.) diameter hole, in a material biaxially stressed is 0.88. At

Table 4.2: Hole-Size Effects in S2-Glass and Carbon Laminates

The relative strength of the material appears in the four columns headed by the hole radii in inches.

Laminate	0.05"	0.15"	0.30"	0.55"
S2-glass	0.70	0.56	0.50	0.45
Carbon	0.72	0.60	0.55	0.45

the radius of the FRA bolt hole, however, the radial stress is 85% of the circumferential stress, i.e., the stress is not perfectly biaxial. By interpolating linearly between the uniaxial and biaxial strength-reduction curves in Daniel's figure, the strength reduction is 0.86. Therefore, the concentration of stress due to a hole of this diameter in S2-glass laminate is 1/0.86 = 1.16.

The maximum (circumferential) stress at radius r in a disk of radius b is given by eq. (1) [57] (see Note, p.74):

$$\sigma_\theta = \frac{3+\nu}{8}\rho\omega^2 b^2 - \frac{1+3\nu}{8}\rho\omega^2 r^2 \qquad (1)$$

The stress near the 3.175-mm hole at radius r in the laminate is then simply the stress computed at the radial location of the hole, using eq. (1), multiplied by 1.16.

The stress at the center of a spinning disk is given by eq. (2) [57]:

$$\sigma = \frac{3+\nu}{8}\rho\omega^2 b^2 \qquad (2)$$

which is greater than the stress at the FRA holes, as will be shown in the Results section.

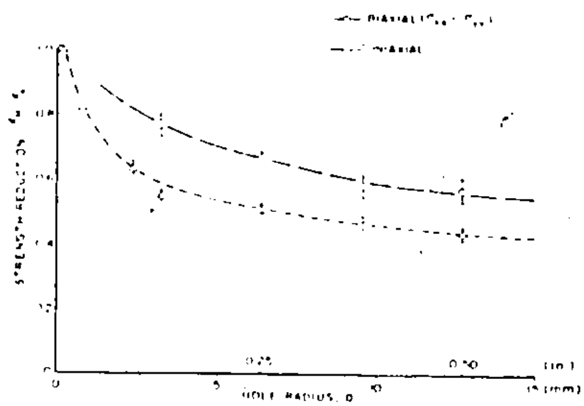

Figure 4.2: Daniel's Results. Strength reduction as a function of hole radius for (0,+/−45,90)2s graphite/epoxy plates with circular holes under uniaxial and 1:1 biaxial loading [55].

Although composed of short (2.5–cm) glass fibers randomly oriented in a resin matrix, the effect of hole drilling in SMC material was assumed to be the same as for the laminate material. However, in contrast with the laminate material, the SMC's uniaxial tensile strength is greater than its biaxial strength.[13] Nonetheless, the stress in the SMC specimen was calculated in the same way as for the stress in the laminated material.

4.2.2 FRA Component Test

[13] According to uniaxial strength data provided by Owens-Corning.

4.2.2.1 Procedure

A locally-manufactured flex-rim attachment and arbor were assembled (Figure 4.3) and attached to a quill shaft. Prior to installation, the FRA was measured along four diameters for comparison with its post-test measurement to check for permanent deformation. The assembled rotor was attached to a quill shaft which was set perpendicular to the FRA plane by adjustment of the arbor set screws. Rotor and shaft were then installed in the chamber as described in Section 3.2 and balanced using a single-plane, trial-weight technique.

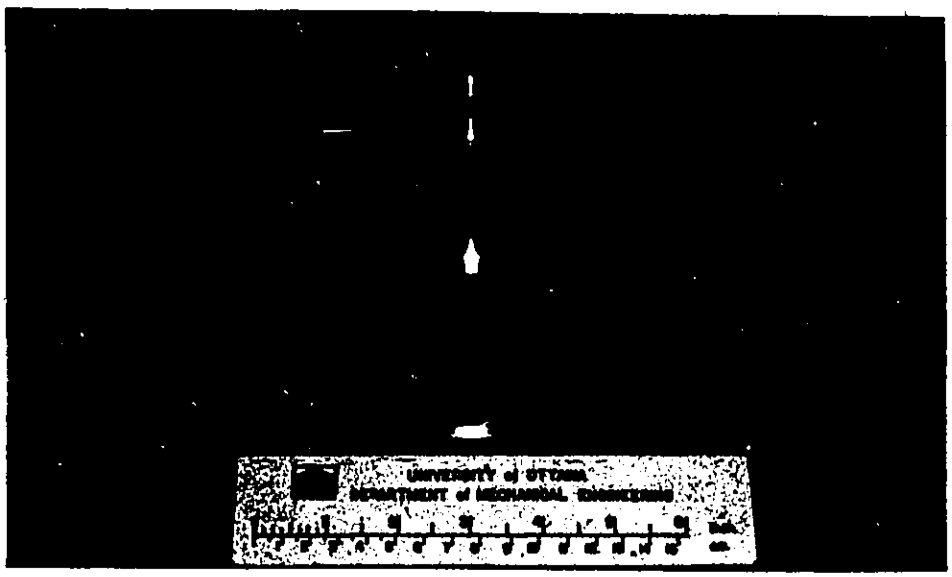

Figure 4.3: Assembled FRA-1 Rotor

The requirement for this test was that FRA-1 be brought slowly to its maximum unsupported speed of 25,000 rpm and its amplitude closely monitored. At this stage in the program, it was not known how accurately the FRA could be manufactured and, consequently, how much imbalance and rim-stiffness variation would be introduced into the component as a result. Consequently, the test objective was two-fold: observation of rotor imbalance to ensure equal flexing of the rim in each quadrant and post-test examination for plastic deformation. Since it was also possible that each rotor component would have to be individually balanced, a secondary test objective was to determine whether or not this was the case.

4.2.2.2 Results and Discussion

The rotor required a very small balance correction (0.035 g-cm). As in all of the 100-Wh rotor tests, the filtered amplitude and phase angle versus speed data (Bode plots) were manually logged from the videotape record, entered into the mainframe computer, and plotted. Figure 4.4 shows the FRA-1 rotor exhibiting a classical first critical-speed resonance at 2200 rpm. Other than passing through a maximum of resonance amplitude between 4 and 7 thousand rpm, of which the only evidence is the videorecorded random firing of the strobe lamps and the attendant false rotor motion, the rotor behaved very well.

The small balance correction required, the constant low amplitude throughout the speed range, plus the absence of plastic deformation proved this component ready for attachment to and further testing on composite rotors.

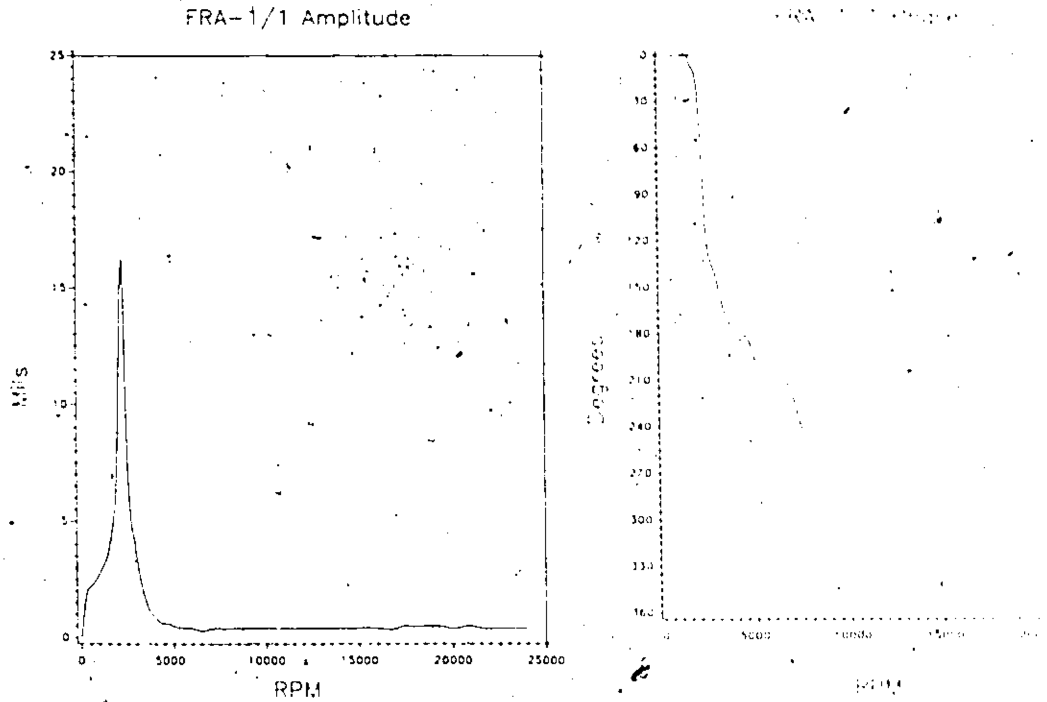

Figure 4.4: Bode Plot for Test FRA-1/1

4.2.2.3 Note on Stress Equations

The derivation of the three stress equations used herein (pp. 71 and 82), as described by Timoshenko, assumes that the disk thickness is small compared with its radius so that circumferential and tangential stress variations with thickness are ignorable. The equation is derived in the usual manner by considering the equilibrium of an elemental section of the disk in polar coordinates.

4.2.3 SMC Rotor Tests

4.2.3.1 Procedure

Test specimens were rough cut from separate SMC plates, utilizing their most uniform cross-section regions. The rotors were then turned to their final diameter, drilled for the FRA bolts, and bolted to the FRA/arbor assembly. Attachment to the quill shaft and chamber installation were as for FRA-1/1.

The test plan for SMC-1 was to accelerate at about 200 rpm/s to the anticipated failure speed of 34,450 rpm. When the disk did not fail by the time it reached the overspeed trip setting of 40,000 rpm, it was brought to rest and a second attempt made.

For SMC-2, 1000 "deep" cycles (7290 to 32,720 rpm) were planned to test the material strength reduction to 69% as predicted by the method of Mandell [58].

Cycling of the rotor was to be carried out using the CAMAC mini-computer system: the computer software was designed to start the rotor from rest, open the brake valve (thus closing the main drive valve) at the preset upper speed, close the brake (opening the drive valve) at the lower speed, and so on, and to bring the rotor to rest after the requisite number of cycles. Acceleration was manually set on the turbine throttle valve and deceleration on a globe valve in the brake line.

After 18 cycles, a decision was taken to proceed with the burst test because the rotor had began to show a growing instability due to oil resonance in the damper journal bearings.

For both ultimate strength (burst) tests, the primary measurement was the failure speed, as recorded by the console camera. For SMC-1, the tachometer of record was the DVF1; for SMC-2, it was the DVF2.

FRA-hub compatibility was to be assessed by direct observation, by chart-recorded rotor response, and by examination of the FRA post-test, if it survived the test.

The effect of through-drilling the composite specimens was to be determined by failure analysis, i.e., reassembling the fragments. (This proved to be impossible with the undifferentiated SMC-1 debris, so SMC-2 was painted to assist in fragment identification.)

4.2.3.2 Results and Discussion

The results for rotors SMC-1 and -2 are tabulated in Table 4.3. Before and after photos of the two rotors are shown in Figure 4.5.

Table 4.3: Results for SMC Rotor Tests

The predicted failure speeds and stresses, compared with actual failure speeds and stresses.

Rotor	Failure Speed(1) (rpm)	Stresses(2) Rad'l (MPa)	Stresses(2) Theta (MPa)	Stresses(2) Center (MPa)	Predicted Failure (rpm)	Predicted Center (MPa)
SMC-1	40,316	163.6	201.3	212.8	34,450	155.3(3)
SMC-2	39,792	173.1	209.8	219.1	39,227	212.8 4

Notes: (1) Linear regression over the last four seconds.
(2) Rad'l = radial stress and Theta = circumferential stress at the FRA bolt-holes calculated as described in Section 4.2.1. Center = central stress. The uncertainty is less than +/-0.05 MPa for SMC-2, but +/-0.4 MPa for SMC-1 due to the large rpm error in the DVF1.
(3) Manufacturer's ultimate tensile strength.

The predicted failure speed of SMC-1 was based on the ultimate tensile strength (UTS) supplied by the manufacturer.

The failure of the rotor to burst at the expected speed was later clarified by the study of hole-size effects that is discussed in Sections 4.2.1.1 and 4.2.1.2. From the instrument-error analysis described in Chapter [illegible], the uncertainties in the measured failure speeds were +/-403 and +/-40[illegible] rpm, respectively.

The stress uncertainty was calculated using techniques recommended by Baird [59] for the products of variables. Dimensional data were taken to be

Figure 4.5: SMC Rotors Before and After Test. Top: SMC-1 before test; debris in the chamber. Bottom: SMC-2 before test; surviving components reassembled after test.

accurate to 0.001 inches, rpm as stated above, Poisson's ratio to within 0.01, and density to within 1 kg per cubic meter. According to Baird, the dominant source of error in the stress computation is due to the speed-squared term. The contribution of this amounts to 0.002 × angular velocity squared, for the DVF2 and 0.02 times for the DVF1.

The failure mode analysis was difficult because there was no way of identifying which part of the disk the fragments had come from. The presence of pieces with bolt holes was, however, encouraging. Painting the upper and low-

Figure 4.6: Bode Plots for SMC-1 and SMC-2 Tests

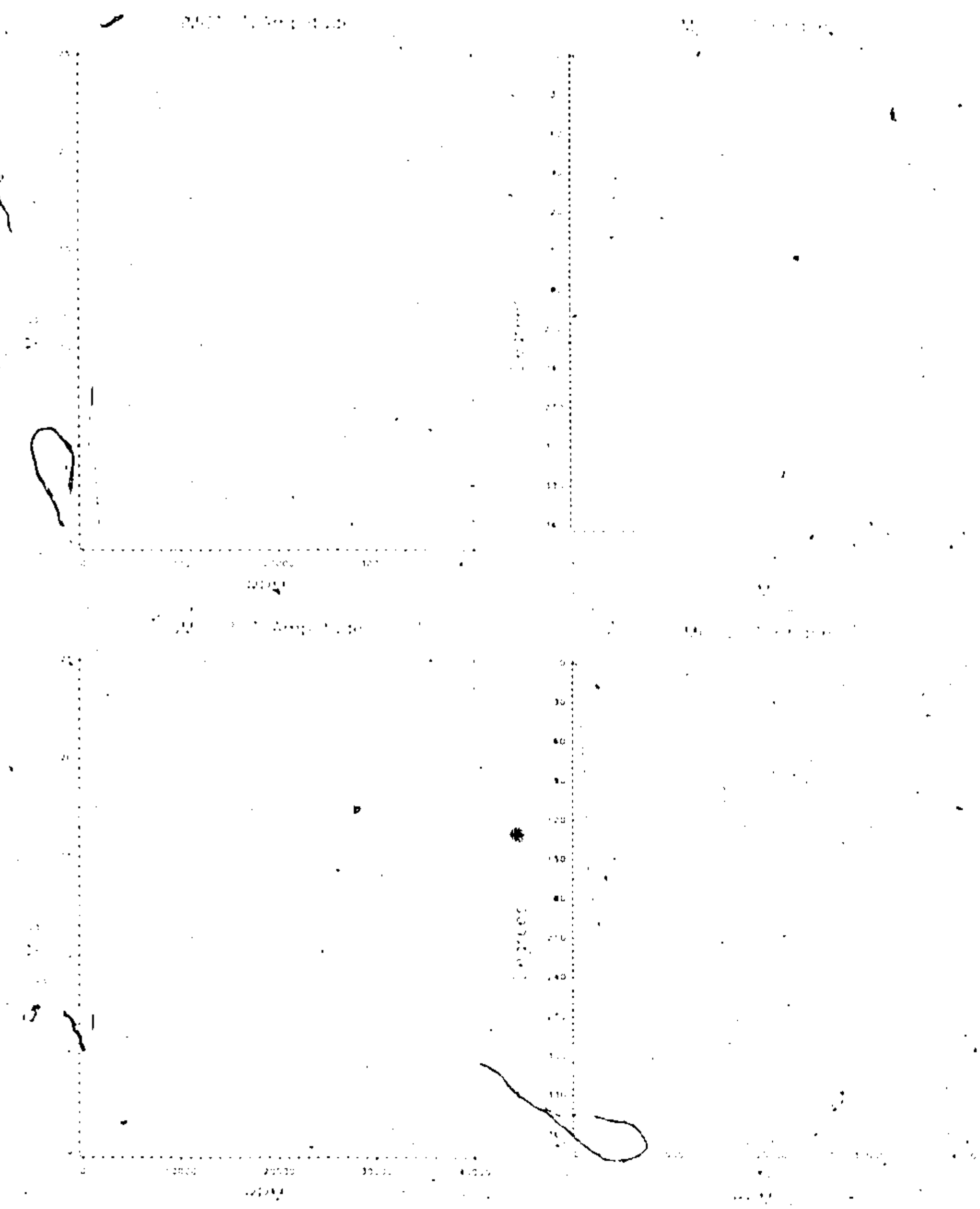

er surfaces of the disk by quadrants greatly assisted in the piecing together of the fragments of SMC-2, as can be judged in Figure 4.5 on page 77, where the rotor is seen before and after the test. The SMC-2 fragments that were recovered appear to have been part of larger pieces that survived the disk failure, but then delaminated upon hitting the containment wall.

In both SMC tests, the FRA remained intact and attached to the arbor. The smooth run up to failure, evidenced by the filtered amplitude versus speed Bode plots in Figure 4.6 on page 78 for both tests, plus the relatively light damage to the FRAs, indicates that radial compatibility between FRA and disk was maintained.

The distinct peaks and accompanying phase shifts for SMC-1 and -2 mark the critical speeds of the turbine-rotor system. The first critical speeds are more readily ascertained from the next set of plots which go from zero to 3000 rpm (Figure 4.7) and are labelled CRIT.

The critical speeds for all 100-Wh rotors are tabulated at the end of this chapter and are found by drawing a vertical line through the 90-degree point on the phase angle curve.

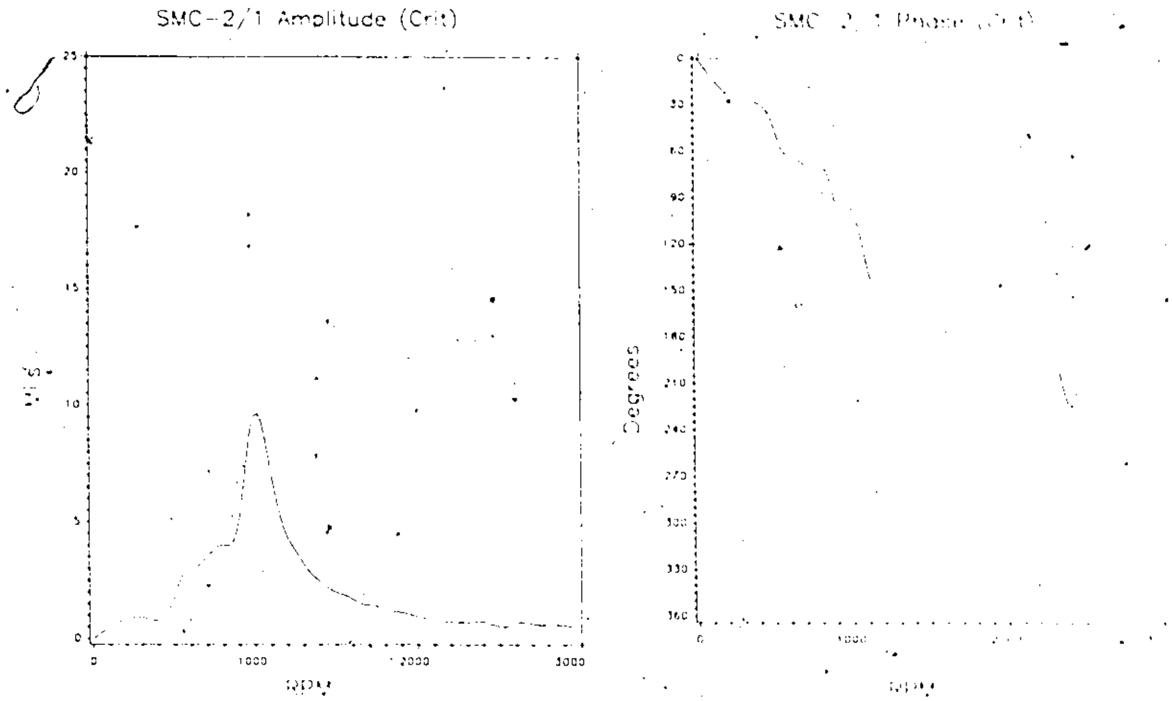

Figure 4.7: First Critical Speed for SMC-2

4.2.4 S2-Glass Laminate (S2L) Rotor Tests

4.2.4.1 Procedure

The S2L rotors were prepared and balanced as the SMC specimens had been, with the exception that S2L-2 was weakened with a 2.54-cm diameter central hole.

It was planned that S2L-1 be cycled between 8850 and 39,560 rpm if the initial runup was trouble-free: if 10 cycles went smoothly, then 100 cycles were to be attempted.[14] As before, the CAMAC system was to be used to control the test.

---

[14] Unlike the SMC-2 attempt to measure fatigue strength, this exercise was experiential only.

Through 13 cycles, the rotor amplitude showed a tendency to grow during deceleration, prompting an immediate attempt to fail the disk.

The rotor survived two trips to 57,000 rpm without failing and, equally significantly, yielding, but not to the point of rupturing the FRA or the bolts.

The first attempt was aborted when the overspeed trip setting of 57,000 rpm was reached. The second attempt was aborted when the rotor amplitude exceeded the safe limit set on the vibration monitor, although the filtered amplitude, as shown in Figure 4.8, was not excessive. The limiting amplitude in this case was the unfiltered one, to which the filtered, or "1X" amplitude made little contribution.

Rotor SL2-2, with its central hole, was installed in the chamber without benefit of a catcher plate to collect the debris so that the rotor could be viewed from below in order to observe possible delamination. The rotor was to be spun slowly to failure speed based, this time, on the highest known value of uniaxial tensile strength for S2-glass laminate material (see Table 4.4) and the hole-size effect discussed in Section 4.2.1.1.

4.2.4.2 Results and Discussion

The results for rotors S2L-1 and -2 are tabulated in Table 4.4, which may be compared with the SMC results; the before and after photos for S2L-2 appear in Figure 4.9.

Classically, the maximum stress in a spinning disk , with a central hole of radius a, and whose radius is b, is given by eq. (3) [57]:

$$\sigma_\theta = \frac{3+\nu}{8} \rho\omega^2 \left(b^2 + a^2 + \frac{a^2 b^2}{r^2} - \frac{1+3\nu}{3+\nu} r^2\right) \qquad (3)$$

Figure 4.8: Bode Plots for S2L-1/1 and S2L-1/2

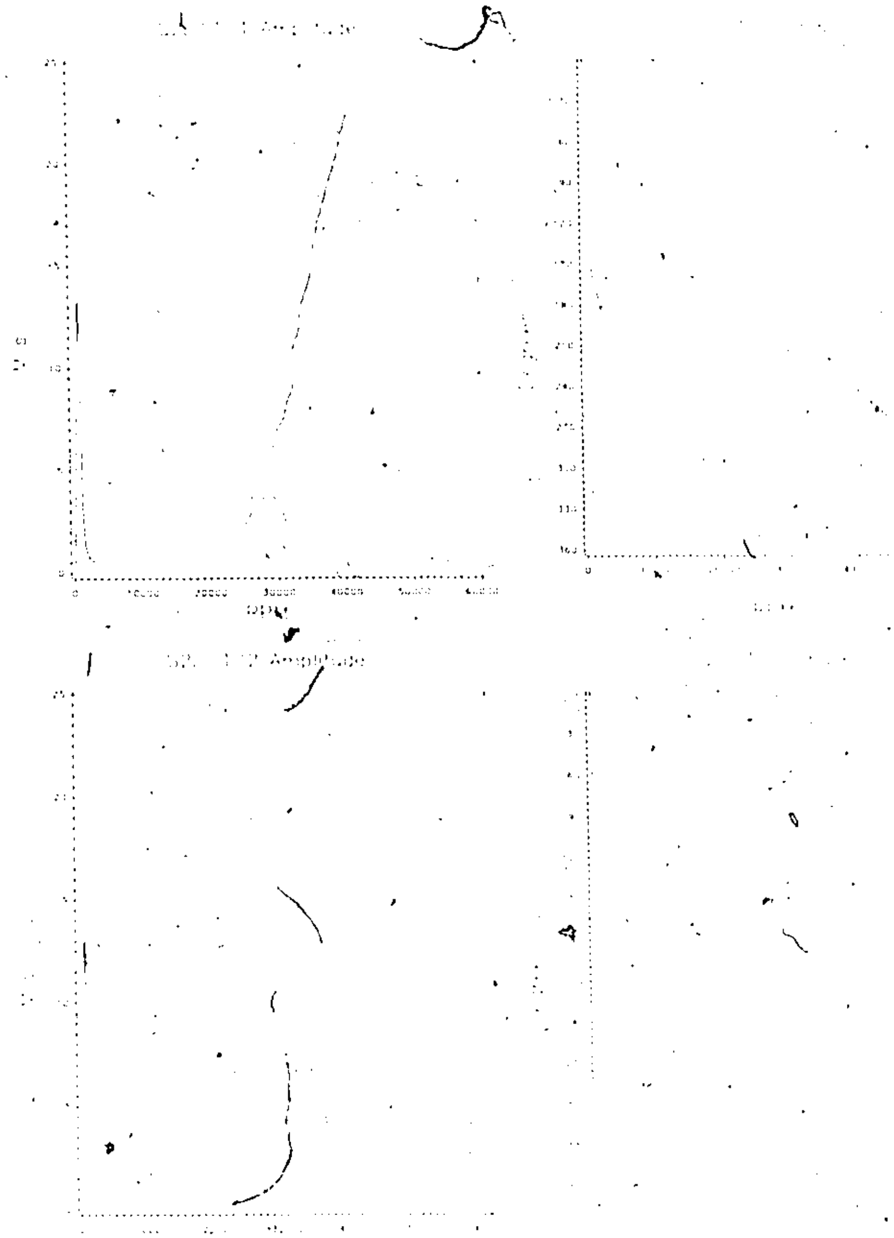

Table 4.4: Results for S2L Rotor Tests

The predicted failure speeds and stresses, compared with actual failure speeds and stresses.

Rotor	Failure Speed(1) (rpm)	Stresses(2) Rad'l (MPa)	Theta (MPa)	Center (MPa)	Predicted Failure (rpm)	Center (MPa)
S2L-1	57,118(3)	433.1	508.9	525.9	51,476	427.0(5)
S2l-2	51,711	343.6	433.9	863.3(4)	47,908	728.8(6)

Notes: (1) Linear regression over the last four seconds.
(2) Rad'l = radial stress and Theta = circumferential stress at the FRA bolt holes. The uncertainty is +/-0.1 MPa.
(3) Rotor did not fail.
(4) Circumferential stress at the edge of the central 2.54-cm-diameter hole.
(5) Manufacturer's ultimate tensile strength.
(6) Published value [8].

Figure 4.9: S2L-2 Rotor, Pre- and Post-Test

In order to observe the effect of the central hole, i.e., possible delamination of the rotor, a camera was placed at one of the lower viewports to give the view seen in Figure 4.11 on page 81. The video frame in this figure shows minor delaminations at 51,522 rpm, but nothing that would suggest a delamination failure.

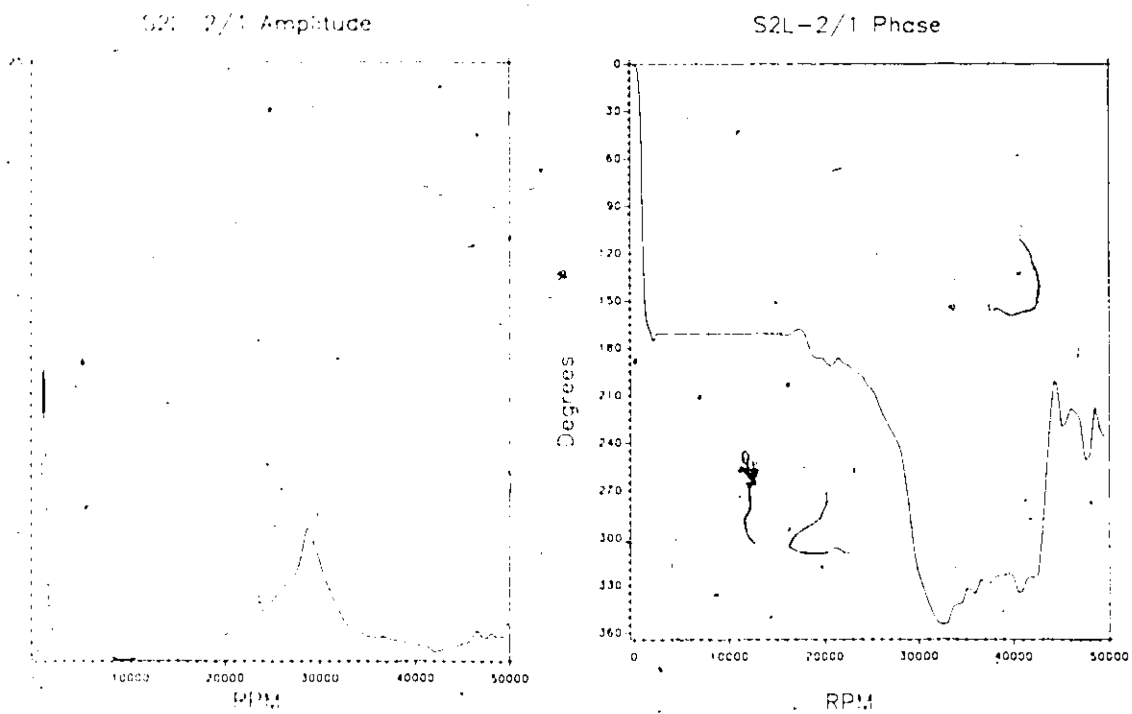

Figure 4.10: Bode Plot for Test S2L-2/1

Figure 4.11: Minor Delamination of Rotor S2L-2

The extrapolated failure speed yields a tangential stress, at the edge of the

Figure 4.12: Low-Speed Bode Plots for S2L-1 and S2L-2

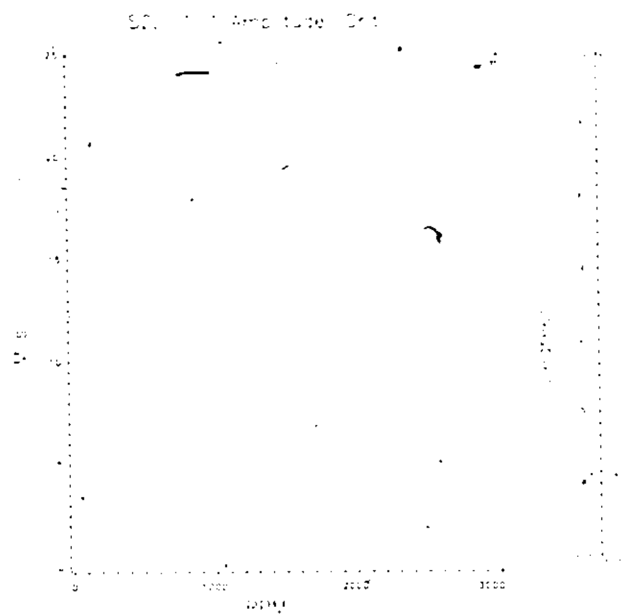

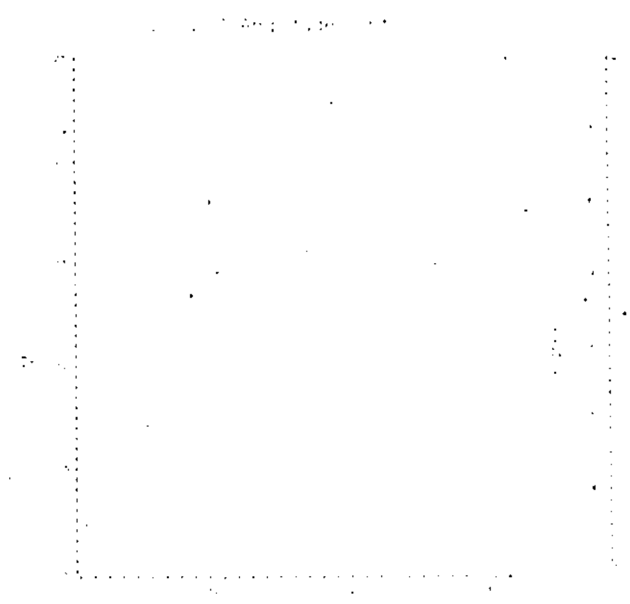

central hole, shown in Table 4.4 on page 83. To have produced this stress at the center of S2L-1 would have required a rotor speed of at least 73,000 rpm, well beyond the 60,000 rpm safe limit specified by the turbine manufacturer.

The Bode plots for the two S2L rotors are presented in Figure 4.8 on page 82 and Figure 4.10 on page 84, where the filtered-amplitude response is seen to be similar to that of the SMC rotors. Again, the critical-speed resonances are accompanied by phase-angle changes, the sharpness of the resonance being related to the magnitude of the phase change. The effect of stressing the FRA during S2L-1/1 appears in the plot of S2L-1/2, taking the form of a broadened second-critical resonance and indeterminate phase change. Since the FRA was plastically deformed during the first cycle, its unbalanced condition evidently had some effect on the internal damping of the rotor. The first-critical speeds are found from the plots of the first 3000 rpm in Figure 4.12 on page 85.

4.2.5 Ring Radial Strength

4.2.5.1 Introduction

The objectives of testing the ring radial strength prototype composite-hub, carbon-ring rotor (RRS-1) were:

1. Determine the radial location and value of the ring's radial strength.
2. Evaluate the rotor's dynamic performance.
3. Test a lightweight containment device.
4. Evaluate the FRA's performance.

The radial and circumferential stresses and displacements in a rotating ring mounted with known interfacial pressure on a disk are given in an appropriate form in reference [49] but are too lengthy to be reproduced here. For the carbon-fiber/resin ring used in this test (ID, 26.7 cm; OD, 41.9 cm; thickness, 2.5 cm), the predicted radial strength is 35.5 MPa (including a residual stress of 10.0 MPa) at 47.6% of the inner to outer radius distance. This stress was predicted to occur at 30,300 rpm.

4.2.5.2 Procedure

A 2.54-cm axially thick E/XAS carbon/epoxy ring was wound in the Project materials laboratory and machined to the final dimensions listed in Table 4.1 on page 67. The SMC hub for this rotor was prepared in the same manner as the SMC rotors (Section 4.2.2) and, before mating with the ring, was statically balanced in the spin-test chamber. Rotor assembly was effected by cooling the SMC hub in liquid nitrogen.

The assembled rotor (including FRA, arbor, and aligned quill shaft) was installed in the chamber and balanced.

The carbon/epoxy ring was painted white in alternate quadrants on the upper surface in order to accentuate the crack. The RCA video camera was mounted above one of the vertical ports 20 cm from the ring surface. With a 25-mm lens, the region of the ring visible on the television monitor was 10 by 13 cm, the center of this region being at the predicted radius of the circumferential crack. To contain the rotor within a confined circular portion of the oval-shaped chamber containment, a lightweight steel can was built and taped into place beneath the rotor.

In order to slowly increase the ring radial stress, the rotor was accelerated at a very low rate (80 rpm/s). At 25,000 rpm, as the rotor became unstable, its apparent motion became exaggerated for the reasons described in Section 2.3.3.4, confusing interpretation of the rotor's motion.

The test was finally stopped at 29,000 rpm when the rotor began contacting the upper catcher. Because the rotor became unstable at the threshold of the failure-speed region, it was believed there was a possibility that the ring had failed. There being no surface manifestations of failure, the ring was X-rayed.[15] Apart from clearly showing all of the balance holes in the hub, the X-radiographs offered no proof that any failure had initiated in the ring (Figure 4.13), so the rotor was rebalanced and spun a second time.

For the second test, an electronic divide-by-six circuit was installed in order to derive the speed and strobe timing signals from the six-pulse-per-revolution turbine rotor tachometer system. This ensured that the strobe light would remain synchronized with the turbine rotor, and that the DVF2 tachometer would not be confused by extraneous signals, should the oil-whip phenomenon recur.[16]

---

[15] Commercial Products Division of AECL.

[16] The DVF2 tachometer can now be driven either by the turbine or rotor

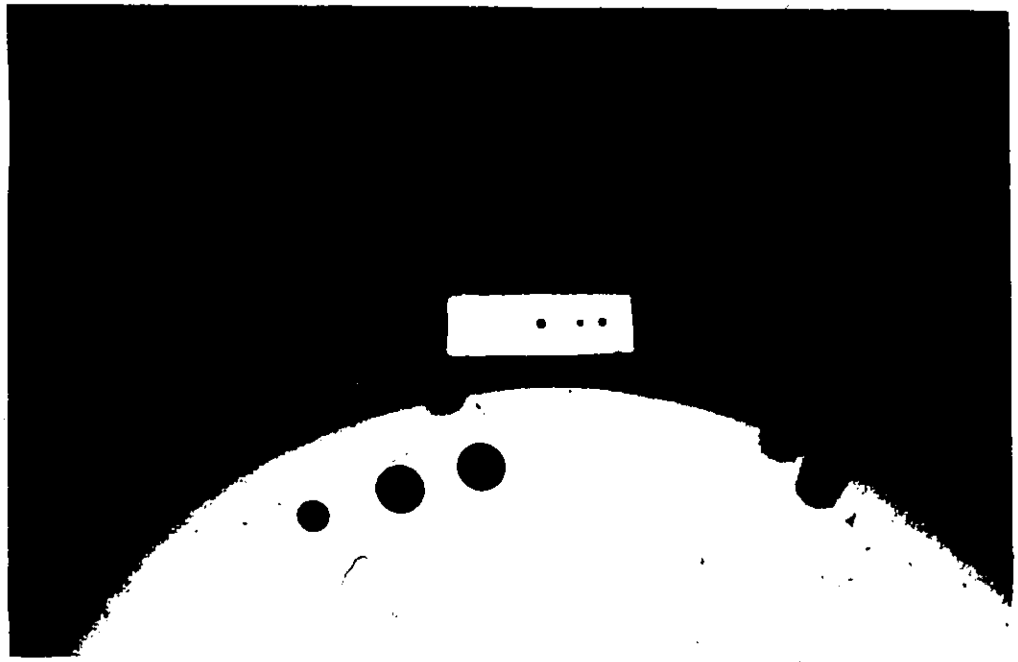

Figure 4.13: Radiograph of Rotor After Test RRS–1/1. The light areas are regions of greater absorption. The black spots are balance–correction holes, the radially–oriented rectangles being preassembly hub balance–correction holes. A flaw–size reference target rests on the ring where no flaws of any kind are seen.

4.2.5.3 Results and Discussion

During the second test of RRS–1, the ring cracked at frame 13 of 30,945 rpm (Figure 4.14) and, within two seconds, (1000 revolutions) the FRA bolts sheared, allowing the rotor to fall into the lightweight containment where it came to rest 150 seconds later (Figure 4.15).

The radial location and speed of failure (Table 4.5) were computed with Project stress–analysis software [8]. The induced stress was calculated using eq. (C.4.10) in reference [49] with the uncertainty computed as before. The radial stress in the ring at failure comprises inertial loading (32.0 MPa), the residual stress (10.0 MPa) [60], and the interfacial pressure (–5.5 MPa).

Rotor Response

---

timing signals.

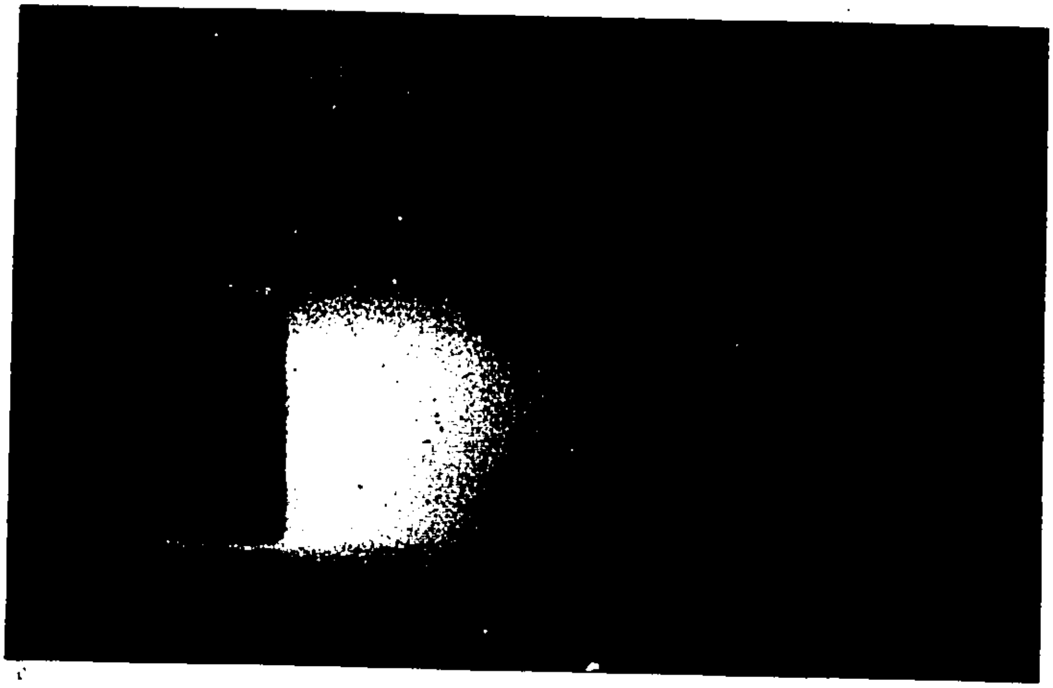

Figure 4.14: RRS–1 Ring Failure

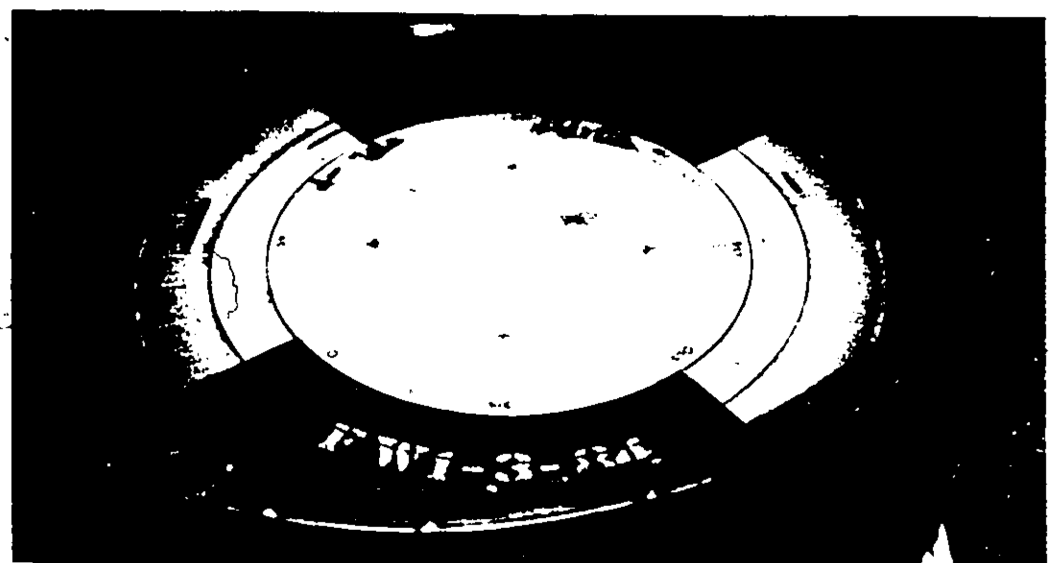

Figure 4.15: Failed RRS–1 in Lightweight Container

The filtered amplitude and phase angle responses for rotor RRS–1 are shown in Figure 4.16. As with the previous plots, these were mechanically produced from manually–logged data.

Table 4.5: Results for the RRS-1 Test

The predicted failure speed and stress, and crack location compared with the actual failure speed and stress, and crack location.

	Speed (rpm)	Stress (MPa)	Radius (%)
Predicted	30,300	35.5	0.476
Actual	30,957	36.5	0.435

As in the responses of SMC-1, SMC-2, S2L-1, and S2L-2, a sharp first critical resonance is accompanied by a 180-degree phase shift, the 90-degree position marking the critical speed. Following first critical, the filtered amplitude rises monotonically until 20,000 rpm where it begins to rise more rapidly. The previous three rotors behaved almost identically, showing well-defined second-critical speed resonances in the 27 - 29 thousand rpm range. RRS-1 evidently just passed its second critical when it failed. Although the phase angle behavior of RRS-1 is unusual in executing nearly one-and-a-half revolutions, it does show a typical modal (phase) change as the second critical is passed. The resonance peak appears to be distorted by the approaching ring failure, otherwise, RRS-1 shows no other unexpected or unexplainable behavior.

Figure 4.16: Bode Plots for Test RRS-1/2"

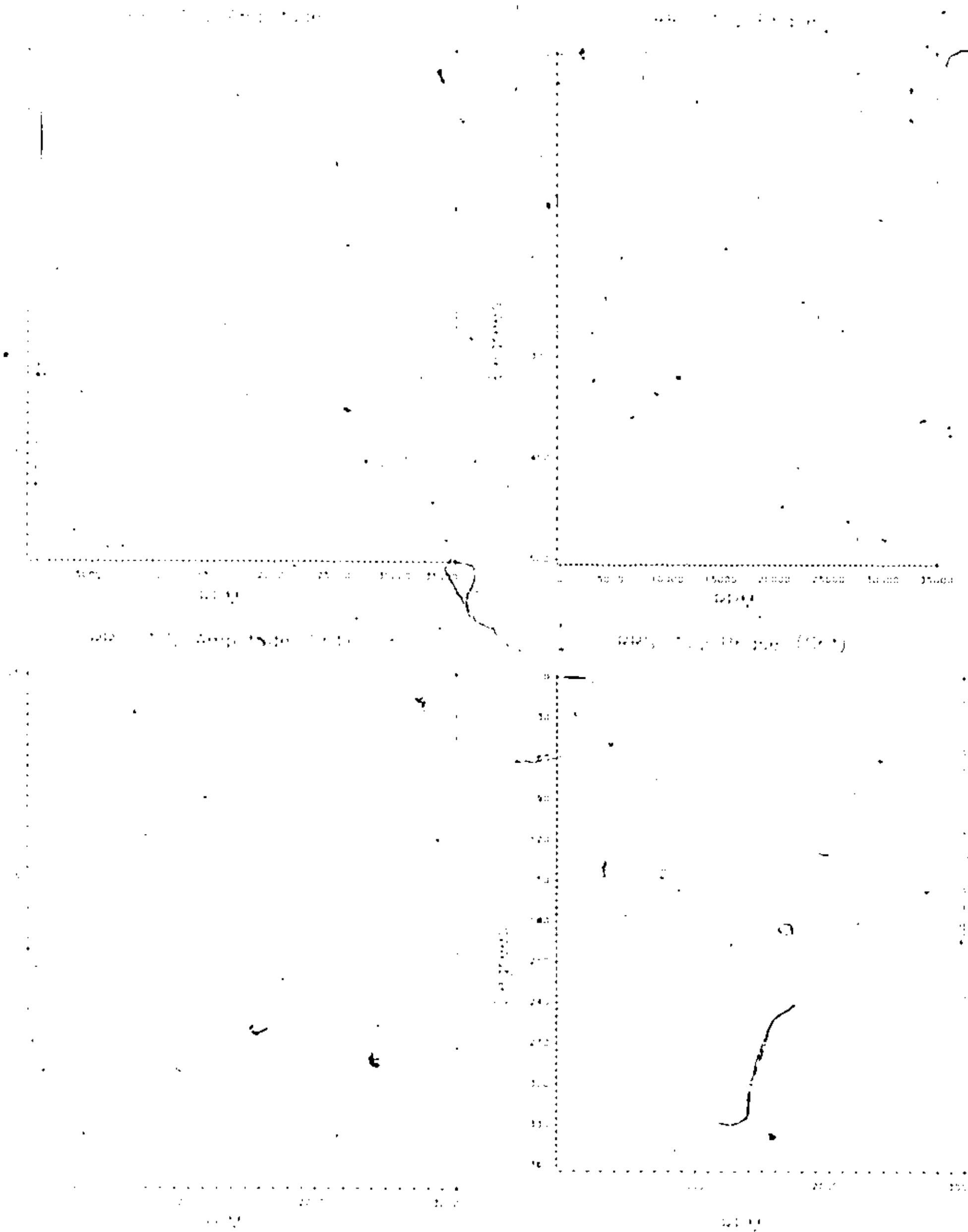

FRA Performance

In the Bode diagrams discussed in the previous section, the filtered amplitude versus speed plot for RRS-1 was similar to all prior FRA-mounted rotor tests up to failure speed.

At failure, the rotor imbalance sheared the FRA bolts, allowing the disk to fall into its containment and leaving the FRA itself intact.

In this test, the FRA performed exactly as intended.

Lightweight Containment

The 3.2-mm-thick mild steel "can" built to catch the rotor was taped to an aluminum catcher tray. This light constraint was sufficient to hold the container in place because the small clearance between rotor and container confined the rotor to mainly circular motion. This small constraint, plus the minimal mass of the container, provides a good indication that the benign failure mode designed into the Ottawa rotors will require significantly less containment mass than the General Electric containment design discussed in Section 1.1.

4.3 Metal-Hub Tests

4.3.1 Introduction

The rotors tested and their test objectives for this phase were:

1. FRH-1: flex-rim hub dynamic evaluation.
2. SSH-1: the same for the spring-spoke hub.

The flex-rim hub (FRH) was designed to maintain contact with its rings, initially by interfacial pressure (shrink fitting), and at speed through the radial growth of the portion of the hub between its spokes. The concern with this design was that, as the ring "lifted off", there might be insufficient restoring force to oppose any perturbation causing the ring to move laterally with respect to the hub. Consequently, part of the rotor's evaluation was the examination of the uniformity of the gap between hub and ring, at speed, in each quadrant.

The spring-spoke hub (SSH), on the other hand, was designed so that a large preload on the aluminum liner from the compressed spokes would be transmitted to the composite rings by the liner maintaining positive pressure at all speeds. The concern with this rotor was the possibility of nonuniform loading on the sixteen spokes. Both rotors are shown in Figure 4.17.

Figure 4.17: Rotors FRH-1 and SSH-1. FRH-1 is at left, SSH-1 at right.

4.3.2 Flex-Rim Hub (FRH) Rotor Test

4.3.2.1 Procedure

The spin tests for rotor FRH-1 were designed to:

1. characterize its stability up to 35,000 rpm and
2. measure the gap between hub and ring at the spoke diameters as a function of speed.

Stability

At the time that these tests were performed, the only frequency analyzing equipment available was the DVF2. The time-consuming procedure for obtaining spectral data with this device required that the rotor be held at a constant speed while the auto-sweep controller caused the internal signal generator to sweep, at an internally-controlled rate, from lower to higher externally-set frequencies. This causes the filter to sweep its 120 (or 12) rpm bandwidth over the spectrum of frequencies generated at that speed. An x-y plotter connected to the DVF2 dc and filtered amplitude output terminals (rpm on x and amplitude on y) records the results, a different x-axis being used for each speed analyzed.

The interfacial pressure created by the diametral difference between hub and ring is sufficient to keep the two components in good contact up to 10,000 rpm [8]. Beyond this speed, the flexible rim of the hub at the spoke locations is constrained from growing radially by the spoke, whereas the rim between the spokes is not, resulting in contact being maintained in the inter-spoke region.

Gap Measurement

To measure the gap between ring and hub, a machinist's rule was fixed above the rotor in the field of view of one of the upper viewports (Figure 4.18) and monitored with a video camera. The 35-mm photograph in this figure was made in an effort to improve resolution of the gap width.

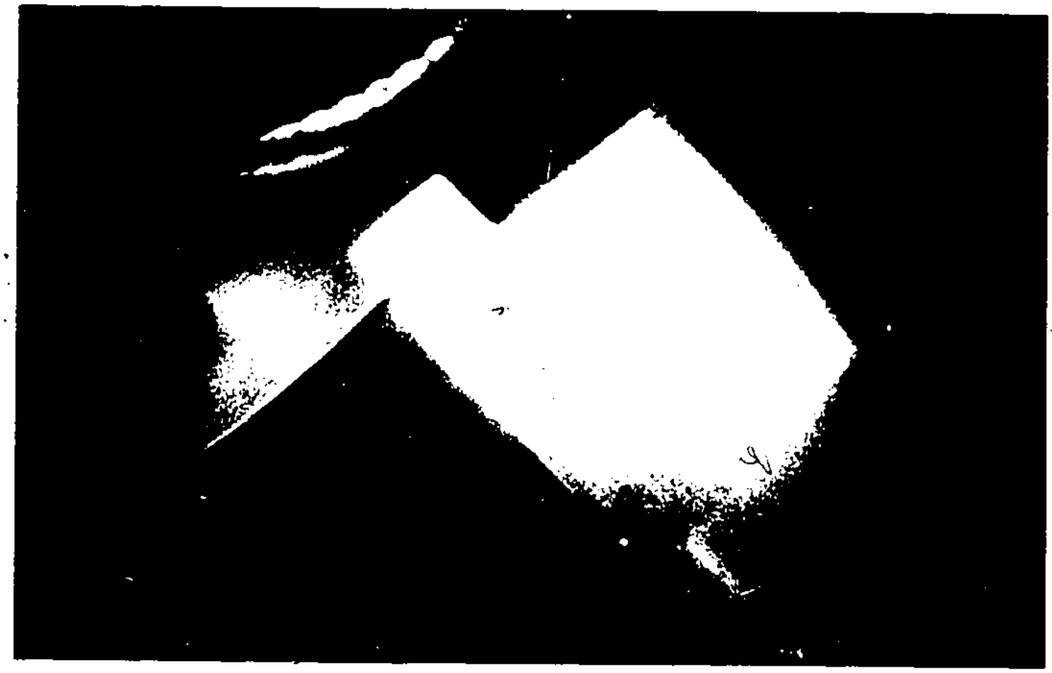

Figure 4.18: FRH–1 Ring–Hub Gap

4.3.2.2 Results and Discussion

Stability

FRH–1 proved to be exceptionally stable over its 0 – 35,000 rpm speed range, achieving its maximum rated speed on seven occasions. The Bode plots in Figure 4.19 document the rotor's filtered amplitude and phase response for Test FRH–1/1 and are similar to the FRA–1 experiment in that the first critical speed is relatively high and marked by a sharp resonance, and the phase angle remains relatively constant in the second mode.

Figure 4.20 is a cascade plot of FRH–1/2 produced in the manner discussed in the previous section. The salient feature of this plot are the "one–times" frequency peaks (hereafter, "1X"), harmonics thereof and oil whip at 10 and 15 thousand rpm. The horizontal axis is the frequency of the vibration spectral components, the vertical axis is the rotor speed at which the scans were made. The low–frequency peak at 30,000 rpm, as will be discussed in the

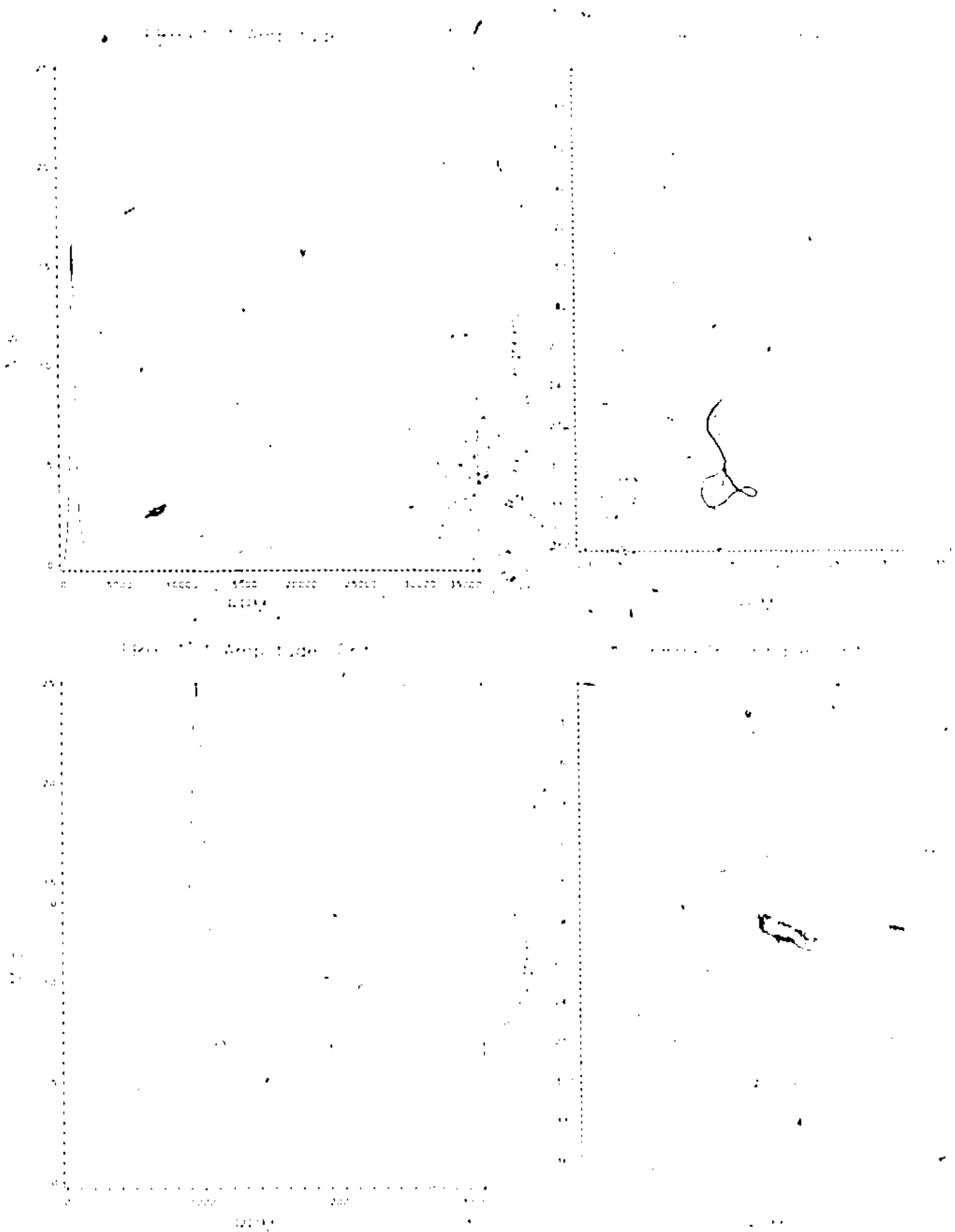

Figure 4.19: High- and Low-Speed Bode Plots, Test FRH-1/1. The plots marked (CRIT) are the expanded view of the critical-speed region.

SSH test, is very likely a moment-induced precessional whirl. As noted on the figure, the rotor became unstable after running at that speed for several minutes.

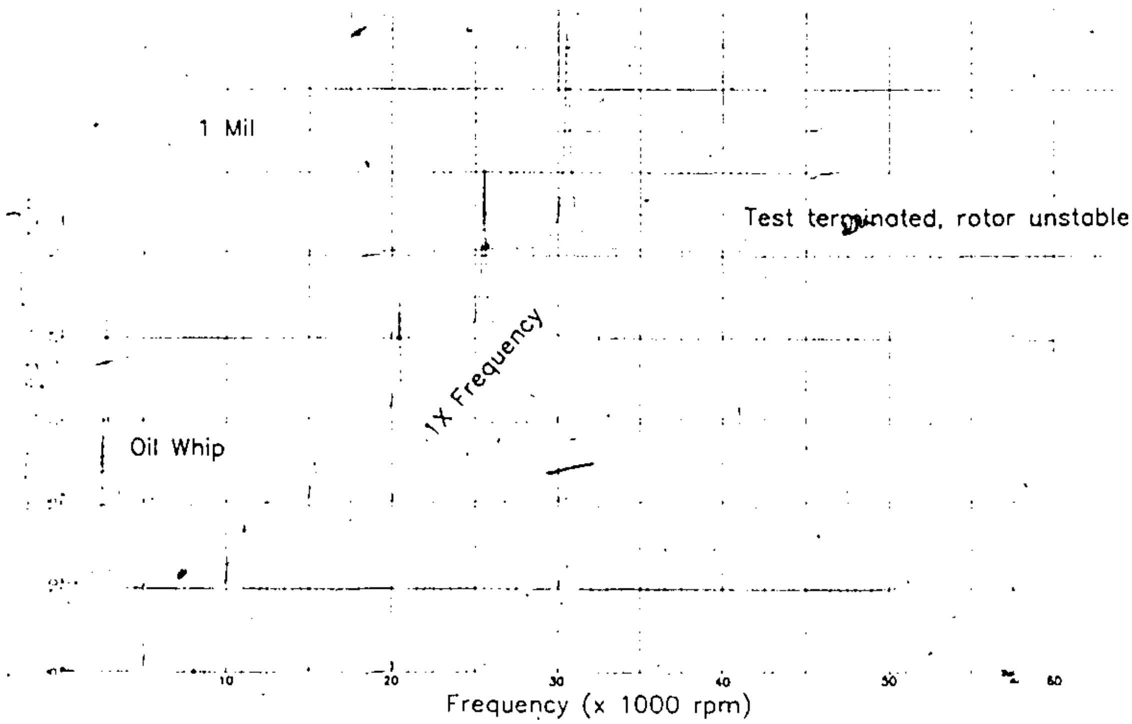

Figure 4.20: Cascade Plot, Test FRH-1/1

The next figure illustrates the rapidity and magnitude of oil-whip onset for a light rotor. This phenomenon, studied in more detail for this system elsewhere [51] typically causes large excursions just above twice first critical and is transient. In this sequence of video scenes, the filtered amplitude is digitally displayed and the unfiltered amplitude is estimated from the oscilloscope. Amplitudes are peak-to-peak and stated in mils.

- 2401 – both amplitudes essentially zero.
- 2548 – filtered amplitude 0.32, unfiltered 2.
- 2597 – filtered amplitude 0.27, unfiltered 5.
- 2670 – filtered amplitude 0.39, unfiltered 8.
- 2912 – filtered amplitude 0.12, unfiltered >8.
- 3735 – filtered amplitude 0.05, unfiltered 7.
- 4241 – filtered amplitude 0.12, unfiltered 3.

Figure 4.21: FRH-1 Oil-Whip Sequence. The video sequence starts at the top left and goes from left to right, and from top to bottom. The final frame is full screen to show the rotor and probes.

- 4506 – filtered amplitude 0.13, unfiltered 0.

The last photograph (4506 rpm) shows the location of the orthogonal displacement transducer supports. The armored cable of one of the transducers is visible alongside the lower left spoke. The second transducer and the keyphasor transducer, in line with and above it, are hidden by the top left spoke.

To summarize, two dynamic phenomena were observed in testing this rotor. At lower speeds, oil whip was in evidence and at higher speed, low-frequency whirling, neither of which can be attributed to rotor design.

Ring–Hub Gap

By slowly accelerating the rotor and watching the hub–ring interface, ring lift–off was detected visually at 20,000 rpm. The gap data are listed in Table 4.6, and plotted as (+) in Figure 4.22. The solid curve fitting the data is a 3.5–power law, which probably says more about the method of measurement than about the laws of physics. The expected square–law–dependent gap (from Project rotor–design software) is plotted as a broken line.

Table 4.6: FRH–1 Gap Data

The estimated ring–hub separation versus speed for FRH–1.

Multiple of 1/64"	Gap Size (mils)	Rotor Speed (rpm)
0.5	7.8	21,400
1.0	15.6	25,500
1.5	23.4	29,500
2.0	31.2	32,000
2.5	39.0	33,900
3.0	46.8	35,100

In addition, the rotor was examined at each spoke location at various speeds in the ring "lift–off" speed range. Within the limits of the gap measurement technique described above, the gaps at each of the spokes were equal. However, the fact that the rotor was so stable makes this observation gratuitous.

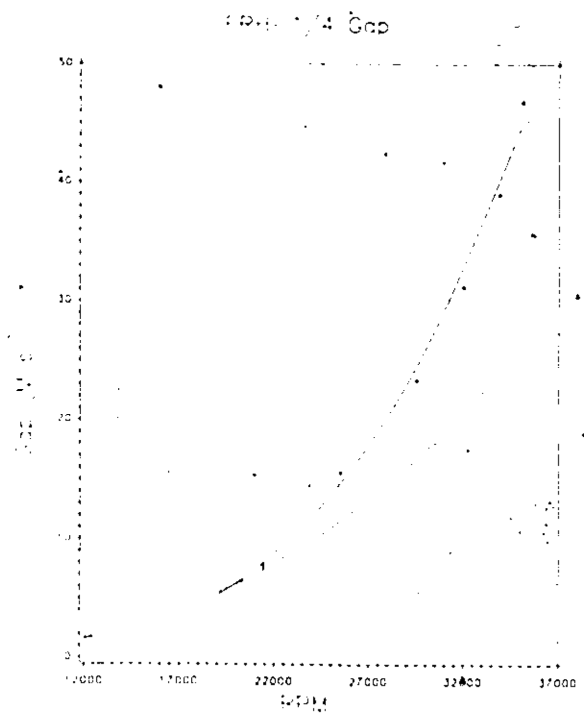

Figure 4.22: Ring–Hub Gap Plots, Test FRH–1/4. Solid line, data curve fit; broken line, theoretical square–law gap dependency; and observational data (+).

4.3.3 Spring-Spoke Hub Test

4.3.3.1 Procedure

The sole objective in testing rotor SSH–1 was the determination of the stability of the design. To that end, two tests were planned: one to obtain spectral data (cascade plot, as described in Section 4.3.1) and the second to obtain filtered amplitude versus speed (Bode) curves up to the rotor's safe maximum speed of 30,000 rpm, although data to 25,000 were acceptable in qualifying the rotor.

Following these tests, SSH–1 was fitted with a 3–kg carbon ring shrunk onto the S2–glass ring in order to study the same hub system with a higher inertia.

The first two tests were conducted with SSH-1, shown in Figure 4.17 on page 94, with a single S2-glass ring (dimensions in Table 4.1 on page 67) and did not proceed to the 30,000-rpm limit because of excessive amplitude growth. Since the glass ring on this rotor was designed for large radial dilation, moreso than in the final design, the amplitude response (Figure 4.23) was not entirely unexpected.

The modified rotor, SSH-2, was also given a maximum speed limit of 30,000 rpm; its test procedure was essentially the same as for SSH-1.

4.3.3.2 Results and Discussion

This rotor did not assemble well on the first attempt, its runout and tilt measuring 11 mils and 0.12 degrees, respectively. The version of SSH-1 shown in Figure 4.17 on page 94 had a poorly seated upper spring-spoke plate because the outside diameter of the arbor seating surface was 5.40 cm compared with the 7.30-cm diameter of the central bushing beneath, resulting in unequal loading in the upper and lower spring plates. This caused unacceptable runout and tilt and was corrected with an arbor target the width of the central bushing.

After balancing, SSH-1 was accelerated slowly in an attempt to reach its maximum safe speed. This attempt, documented in Figure 4.23, was aborted at 28,423 rpm because the amplitude appeared to be rising too quickly. Otherwise, this plot exhibits a well-behaved first-critical resonance, a drop in amplitude at the balance speed, stable behavior between 10 and 22 thousand rpm, and a steep rise in amplitude at shutdown.

The rotor was then rebalanced and the cascade plot in Figure 4.24 was made. This plot does not show the same type of oil-whip resonance as FRH-1, although they are similar in all other respects (excepting the different

Figure 4.23: Low- and High-Speed Bode Plots, Test SSH-1/2

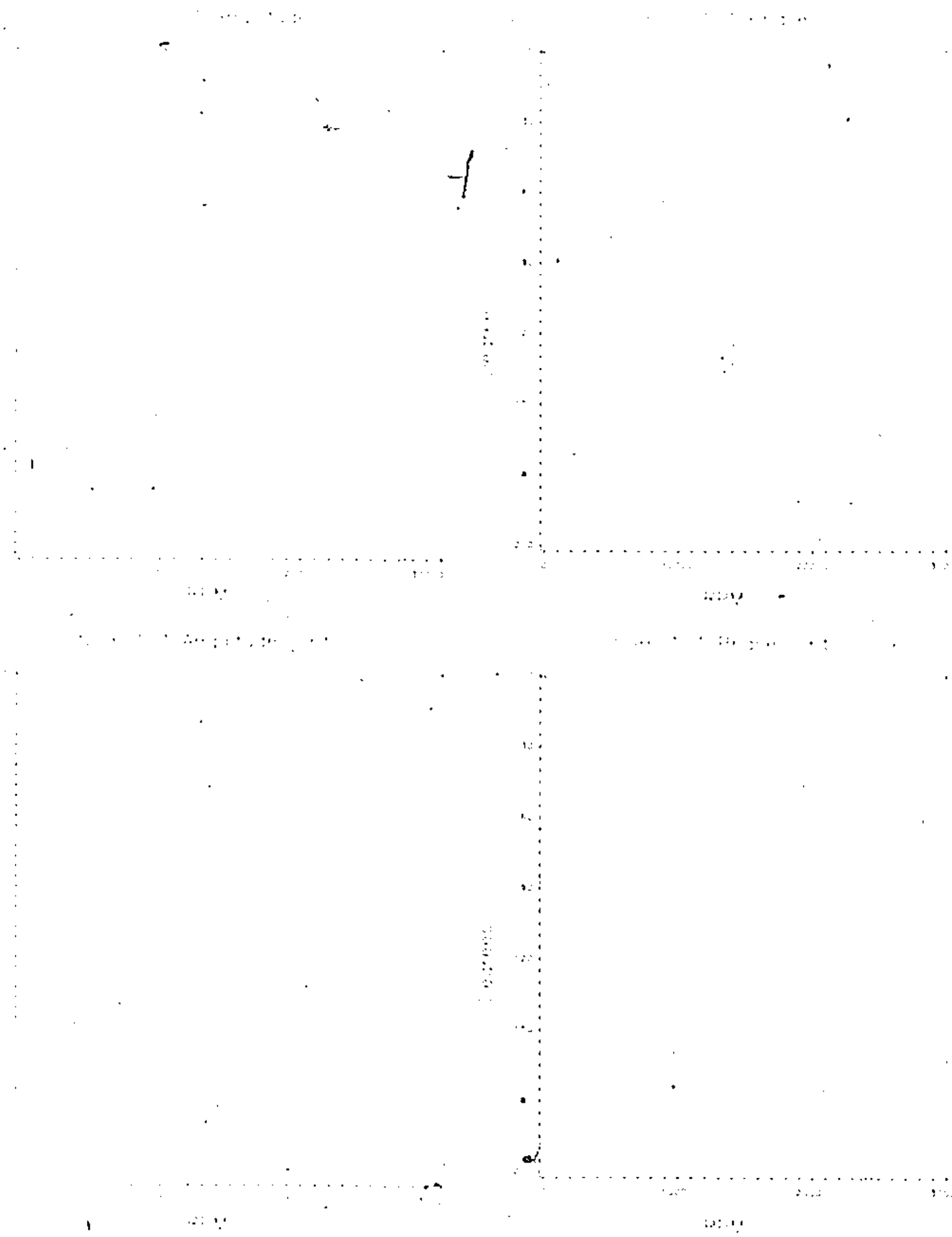

scale on the rpm axis). The 0 – 2500 rpm "noise" at all speeds in this figure is the same as that just developing at 30,000 rpm for FRH-1 in Figure 4.20 on page 98, and is most likely the precessional vibration that is present in the unfiltered signal at 20 and 25 thousand rpm. The precession, shown in Figure 4.25 has frequencies of approximately 21 and 2.5 rpm, respectively, at the indicated rotor speeds of 20 and 25 thousand rpm. This type of rotor motion has been described as retrograde whirl [51], caused by a moment on the rotor. This is not a design-related phenomenon, but rather, a property of axially-thin rotors which do not have two convenient balance planes.

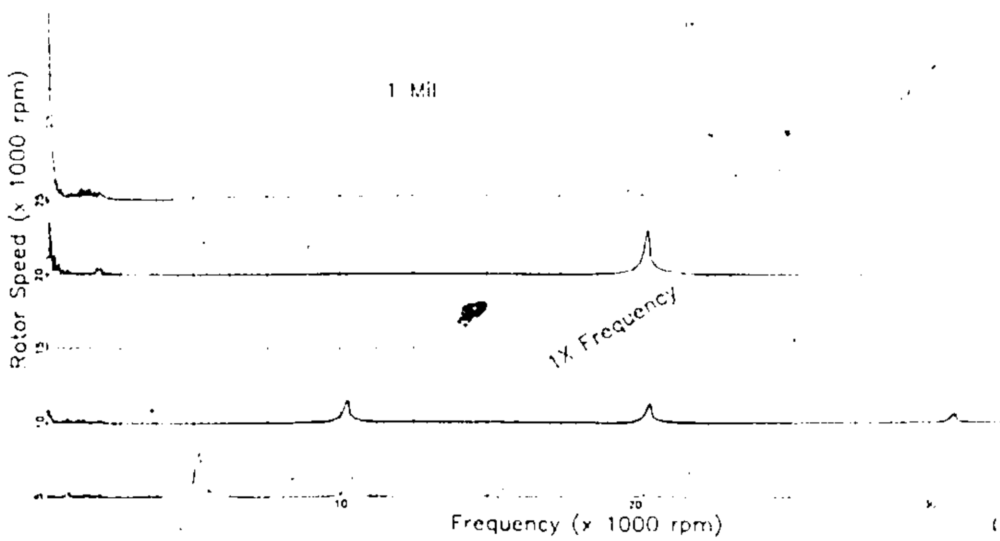

Figure 4.24: Cascade Plot, Test SSH-1/1

A second attempt was made to reach 30,000 rpm, but was aborted at 25,294 for the same reason.

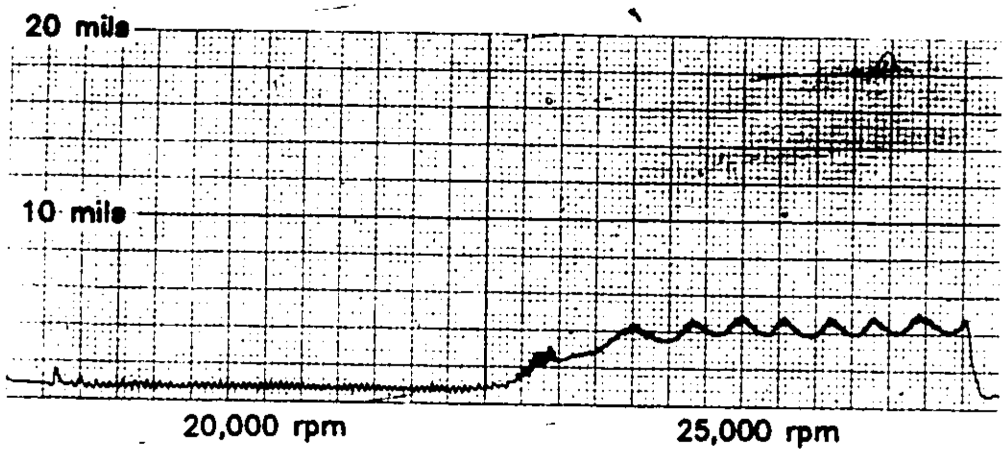

Figure 4.25: SSH-1/2 Unfiltered Amplitude. This trace is the rotor's unfiltered amplitude. The horizontal (time) scale is 4 s/mm, 1 mm being the smallest division.

SSH-2

The response of this rotor on its first and only high-speed test (Figure 4.26) is more like the other rotors than SSH-1. Its amplitude rises linearly with speed, with the exception of a small bump at 20,000 rpm, until the ring fails. The phase-angle behavior is also quite different, increasing immediately to a maximum of 360 degrees where it stays, more or less, until failure. In the absence of any spectral data, an amplitude versus speed plot with filtered and unfiltered data was made (Figure 4.27) and shows that the rotor experienced oil whip throughout most of test.

The onset of whip is clearly marked at 1600 rpm, well above twice first critical speed. It persists until 24,500 rpm where, presumably, the growing rotor imbalance is sufficient to overcome the hydrodynamic forces driving the oil whip. The frequency of the whirl, derived from the unfiltered response peak and analysis of the oscilloscope orbit display, was approximately 1600 rpm throughout.

Figure 4.26: Low- and High-Speed Bode Plots, Test SSH-2/1

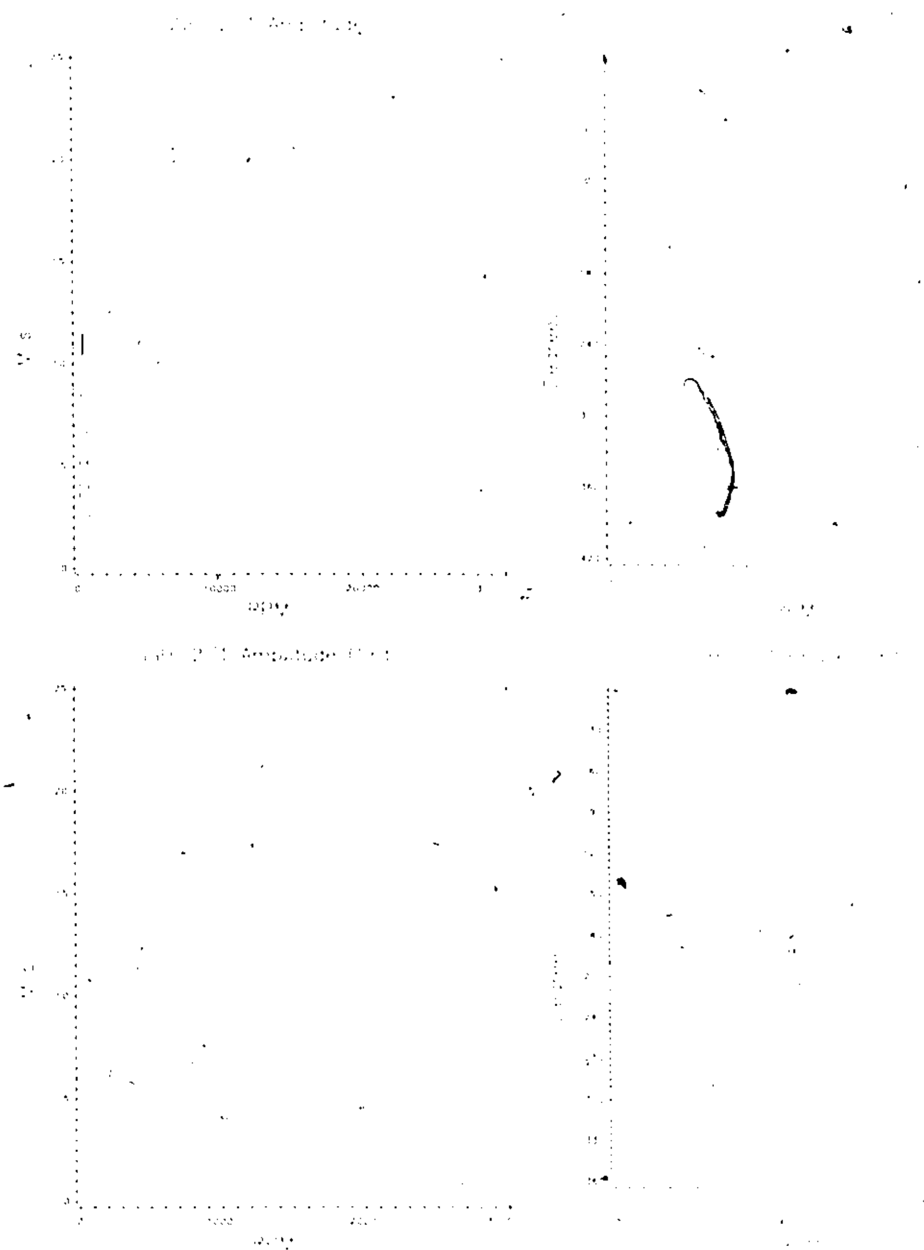

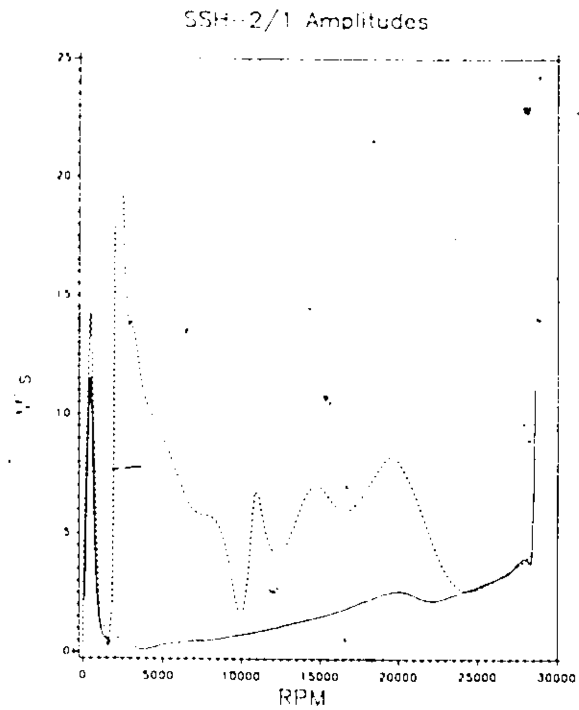

Figure 4.27: Filtered and Unfiltered Amplitude, Test SSH-2/1. The solid line is the filtered-data curve.

In the test of RRS-1 (intentional ring failure, Section 4.3), that rotor took approximately two seconds, from the occurrence of the crack in the ring, to shear the FRA bolts and fall into the container. In the test of SSH-2, approximately one and one-half seconds lapse from the first indication of rotor imbalance until the shaft fails. The similarity of the two failures pointed toward ring failure in SSH-2. It was later determined that the carbon ring on this rotor had been cured according to a schedule known to produce (inferior) transverse radial strengths very close to the stress in the SSH-2 ring at failure.

4.3.4 Summary

This chapter has dealt with the 100-Wh-rotors tests which had as objectives: evaluating the novel FRA system, obtaining biaxial strength data for composite rotors, proving the carbon-ring system, and collecting data for metal-hub rotors. All of these objectives were met; the test data for this phase are summarized in Table 4.7, the critical-speed data from which are plotted against the rotors' masses and inertias in Figure 4.28.

Table 4.7: Summary of 100-Wh-Rotor Test Speed Data

Rotor/ Test	Speeds (rpm) Target	Achieved	1st Critical	2nd Critical
FRA-1/1	24,000	24,000	2200	-
SMC-1/1	34,450	40,318	1000	27,900
SMC-2/1	39,227	39,792	1000	29,000
S2L-1/1	51,476	57,118	850	28,100
S2L-2/1	47,908	51,711	900	29,000
RRS-1/2	30,300	30,957	700	27,100(1)
FRH-1/1	35,000(2)	35,104	920	-
SSH-1/1	30,000(2)	28,423	900	-
SSH-2/1	30,000(2)	28,560	440	-

Notes: (1) Possible second-critical speed.
(2) 25,000 rpm considered successful.

The power-curve fitting to the data (solid curve) gives the following relationships for mass and inertia, respectively:

$$RPM = 2086.7 \ kg^{-0.64}$$

$$RPM = 319.0 \ I^{-0.29}$$

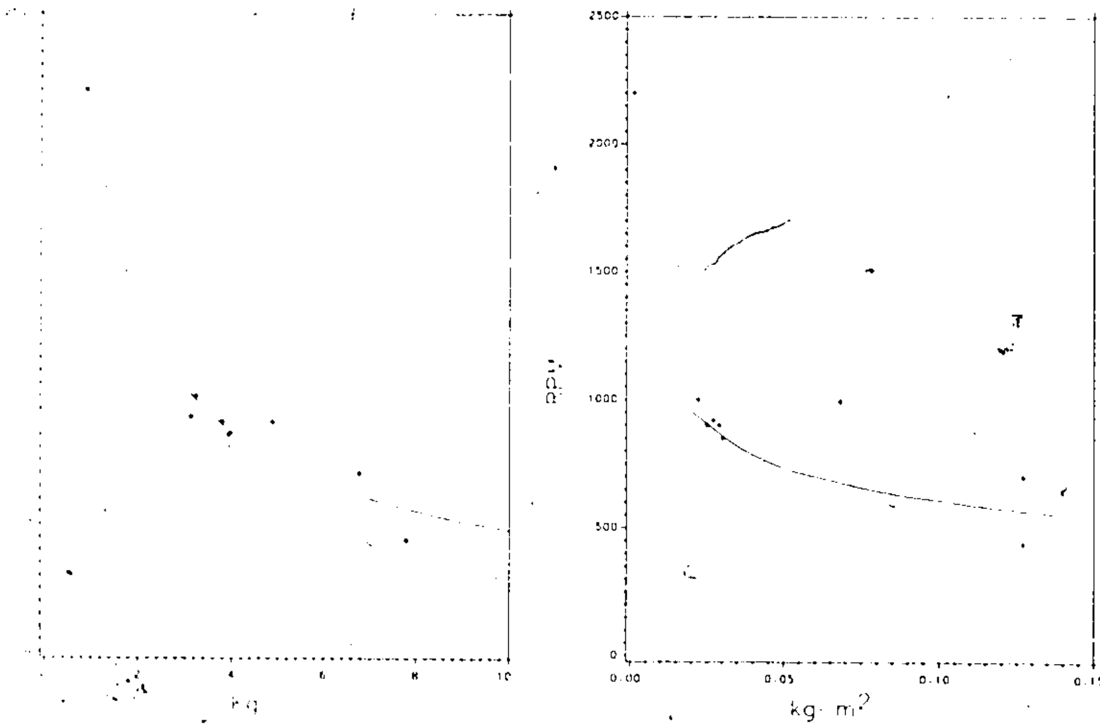

Figure 4.28: Critical Speed Versus Mass and Inertia for 100–Wh Rotors. Speed–mass (L); speed–inertia (R).

The –0.64 power mass dependency approximation of the theoretical –0.5 value reflects both the possible effect of gyrodynamic stiffening of the quill shaft and the error in speed.

The SMC and S2L tests provided material–strength data for the full–size rotors and, indeed, the RRS–1 prototype rotor proved that the ESR Project design philosophy was sound in terms of strength predictability and failure–mode safety.

The high strengths of the SMC and S2L rotors enabled them to reach and pass their second–critical speeds, typified by a resonance peak broader than the first critical and with an accompanying phase–angle change of up to 180 degrees. Although RRS–1 appears to be just passing second critical at failure, according to amplitude data, the phase angle does not behave as convincingly as the SMC and S2L rotors did. Above all, however, the high material strengths recorded (some of the highest ever) and particularly, the high transverse (radial) carbon-ring strength, permitted a major change in the rotor-design philosophy from biannular to single rings for the composite-hub rotors.

The metal-hub rotors' filtered amplitudes were not all that different from each other's, but the phase angles were. FRH-1 mimicked FRA-1 in remaining in mode two (rotation about the center of mass) while SSH-1 does not actually enter mode two until near top speed. SSH-2 exhibited phase behavior similar to that of FRA-1 and FRH-1.

The exercise of estimating the FRH-1 ring-hub gap demonstrates the difficulties associated with the method employed. However, since this test was primarily intended to examine the symmetry of the lifted-off ring regions, collection and analysis of the gap/speed data was motivated more by curiosity than any necessity, and consequently, the variation between results and theory are unimportant. The gaps around the ring, at speed, appeared to be the same in the four quadrants, within the limitations described.

The phenomenon of oil whip was demonstrated in oscilloscope photographs for FRH-1 and in a filtered/unfiltered amplitude plot for SSH-2. The orbit of the rotor, at the low speed in the oscilloscope sequence, was near synchronous. As well, a low-frequency subsynchronous whirl was observed in both the FRH-1 and in the SSH-1 rotors.

In summary, this phase of Project testing was very successful, particularly the RRS-1 prototype rotor test, which paved the way for the final phase, the large-rotor tests.

Chapter V

1-KWH-ROTOR SPIN TESTS

5.1. Introduction

As shown in Chapter IV, none of the four rotor designs were disqualified by the 100-Wh spin tests, so four full-scale, 1-kWh rotors were designed and built. Of these four, three were tested to their maximum operating speeds with the following objectives:

1. To develop dynamic rotor-balancing techniques for large, axially-thick, composite rotors.
2. To drive each rotor to its maximum operating speed, at least once.
3. To collect vibration data in order to characterize each rotor's stability and dynamic behavior.

The four rotor types are shown in Figure 5.1 and their physical data are given in Table 5.1.

FW3 was built in three versions, two of which (FW3-1 and -2) were identical. The three versions were made because the first unit failed at speed and was rebuilt using the same hub and an identical set of glass/carbon rings intended for FW4. Redesignated FW3-2, this rotor was derated to 20,000 from 22,000 rpm and was used for several dynamic experiments [51].

The design and manufacture of the three rotors proceeded from the data collected in Chapter IV: the composite-hub dimensions were based on the biaxial tensile strengths obtained for the SMC and S2-glass laminate materials, and

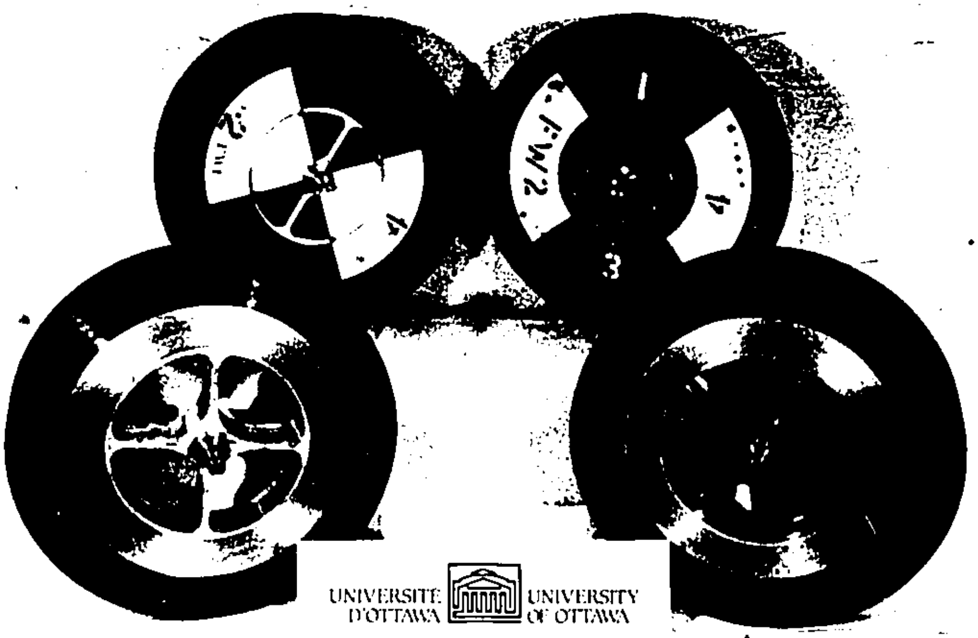

Figure 5.1: Rotors FW1-1, FW2-1, FW3-2, and FW4-1.

the ring dimensions were based on the stress analyses verified by the ring radial strength test.

In this chapter, the test procedure for each rotor was the same and is therefore given only once. Following the procedure section, results and discussion are given by rotor, with a common table of results.

Table 5.1: Design Specifications: 1-kWh Rotors

Dimensions, masses, and polar inertias for the 1-kWh rotors.

Item	FW1-1	FW2-1	FW3-1	FW3-2	FW4-1
Construction					
Hub Design	Disk	Disk	FRH	FRH	SSH
Hub Material	SMC(1)	S2L(2)	Al(3)	Al(3)	M.S.(4)
Ring Material(5)	E/XAS	E/XAS	E-S2	E-S2	E-S2
Parameters(6)					
Diameter (cm)	60.96	60.96	60.96	60.96	60.96
Thickness (cm)	8.31	6.28	8.76	8.76	8.76
Mass (kg)	40.9	34.4	37.8	37.4	38.2
Inertia (kg-m^2)(7)	1.74	1.41	1.89	1.89	1.88
Volume (m^3)	2.41	1.85	2.56	2.56	2.56
Speed (rpm)	18,860	24,760	21,900	20,000	21,775
Energy (kWh)	0.94	1.32	1.38	1.15	1.36
Density (Wh/kg)	23.0	38.4	36.5	30.7	35.5
Life (cycles)	10^5	10^5	10^5	-	-
Performance(8)					
Top Speed (rpm)	25,770	33,520	29,200	-	32,250
Failure Mode	Hub	Ring	E/XAS	-	E/XAS
Energy (kWh)	1.87	2.45	2.37	-	2.93
Density (Wh/kg)	47.1	76.8	67.0	-	82.1

Notes:
(1) SMC - sheet molding compound, Owens-Corning Corp.
(2) S2-L - S2-glass laminate, Owens-Corning Corp.
(3) Al - 7075-T651 aluminum.
(4) M.S. - C300 maraging steel spokes, 7075 aluminum liner.
(5) E/XAS - Hysol Grafil Ltd., Coventry, UK, carbon fiber.
E-S2 - E/XAS outer, S2-glass inner.
(6) The design parameters refer to the rotor's maximum operating speed. Speed, energy, and (energy) density are for the max-operating speed. All rotors were designed to operate in an environment of -40 to 100 degrees C.
(7) Rotor polar mass moments of inertia were calculated.
(8) These numbers refer to the rotor's ultimate-speed capability. Failure mode is the component designed to fail first.

5.2 Procedure

An essential part of equipment development for the large-rotor tests was the lower catcher design and installation. Both the equipment and method devised to install the massive rotors and the lower catcher has been described in Section 3.2. This procedure requires that the quill shaft be installed in the turbine first, and, with the turbine bolted in place, the rotor is raised to mate with the shaft.

With the rotor secured to the end of the quill shaft, by means of three set screws, and with the turbine rotor levelled, dial-guage readings were taken of the rotor's tilt and runout. If the rotor tilt, measured at the circumference of the wheel, exceeded 6 mils,[17] the torque on the set screws was adjusted until the tilt was reduced accordingly.

A fast Fourier transform (FFT) spectral analyzer was used for this group of tests and was used to obtain individual spectra and produce cascade plots.

For some of the tests, CAMAC software[18] was available for logging filtered amplitude, phase angle, and rpm data. This made possible the production of Bode plots with data taken at 200-rpm intervals in two planes.

5.3 Results and Discussion: FW1-1

Data collected during its eight high-speed tests showed FW1-1 to be a well-behaved rotor. The data for FW1-1/5 was selected for presentation because a complete set of FFT and CAMAC data were collected for this test. A review of Table 5.2 also indicates that, by test number 5, balance techniques had been sufficiently advanced to the point where the rotor required no fur-

---

17 This arbitrary value was found through practice to be the lowest that the tilt could be practically reduced to.

18 Courtesy of Luc Menard, University of Ottawa Engine Fuels Laboratory.

ther balancing. Therefore, this test is representative of the rotor's response for all subsequent tests.

Filtered amplitude and phase information are shown in Figure 5.2 and a cascade plot of the upper plane spectra in Figure 5.3.

Table 5.2: FW1-1 Test History

Test No.	Static (g-cm)	Couple (g-cm^2)	Residual Amplitudes(1) Plane 1	Plane 2	Maximum Speed
1	42.0	- (2)	1.1	1.8	19,000
2	1.4	-	*(3)	*	19,000
3	66.7	653.2	1.4	3.5	18,450
4	-	-	1.5	4.1	18,830
5	160.0	2552.1	0.1	0.8	19,015
6	7.0	0.0	*	*	19,000
7	0.0	0.0	*	*	19,042
8	0.0	0.0	*	*	15,000

Note: (1) The residual filtered amplitude, peak-to-peak, in mils, at balance speed (3000 rpm) after the run up to maximum speed. Residuals before the run up to maximum were typically 1 mil or less.
(2) A (-) in the balance column means no correction.
(3) An asterisk (*) means no data recorded.

The upper plane filtered amplitude is quite flat, following the first critical speed. The lower plane, on the other hand, shows a filtered-amplitude, power-law speed dependency.

After assembly, FW1-1 was checked for concentricity of the displacement-transducer targets with respect to the outside diameter of the entire rotor. Finding there was substantial eccentricity, the target surfaces were ground to bring them back into concentricity. However, this now made the targets eccentric with respect to the quill shaft, as later discovered, by 2.2 mils at

Figure 5.2: High-Speed Bode Plots, Test FW1-1/5

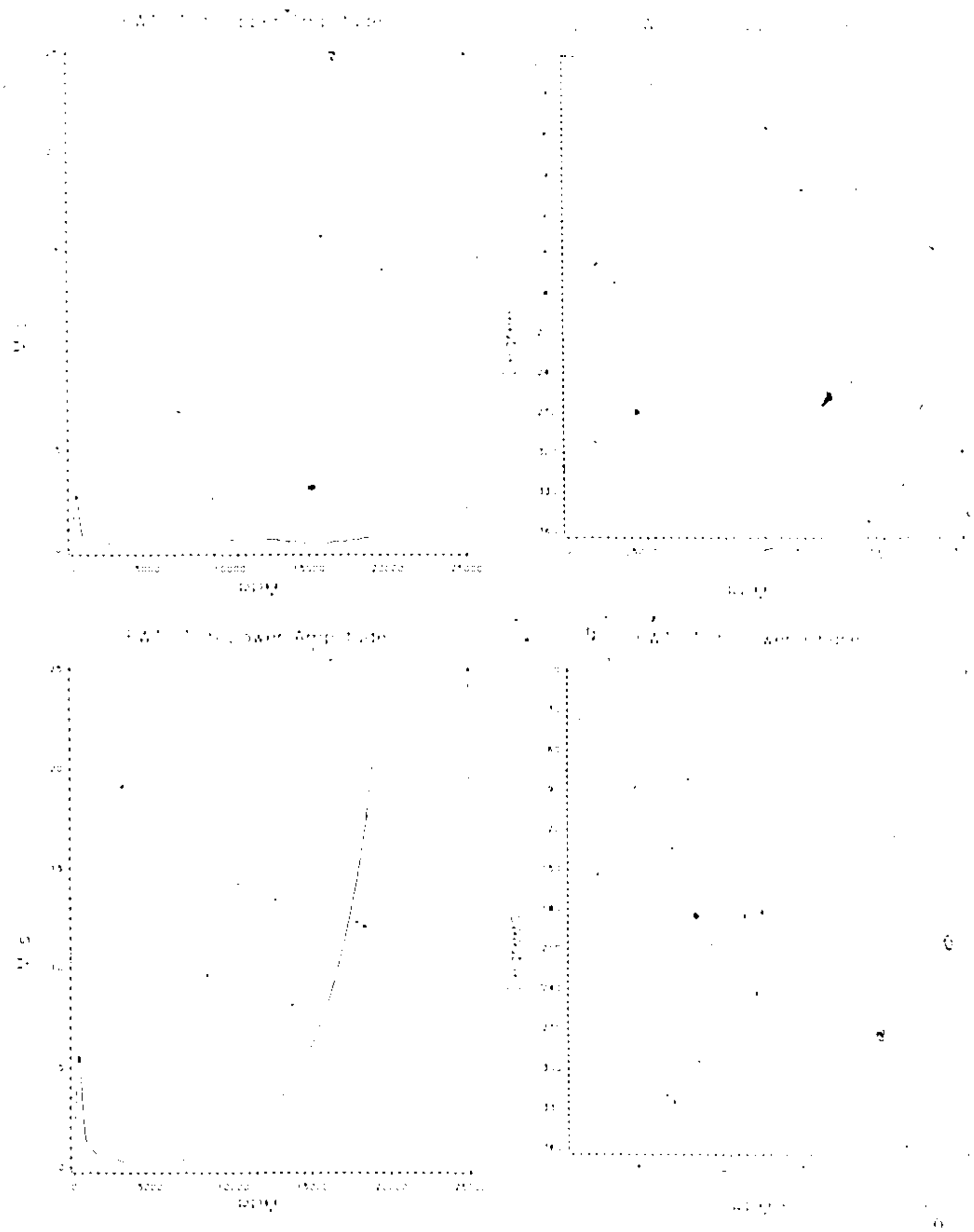

Figure 5.3: Cascade Plot, Plane 1, Test FW1-1/5

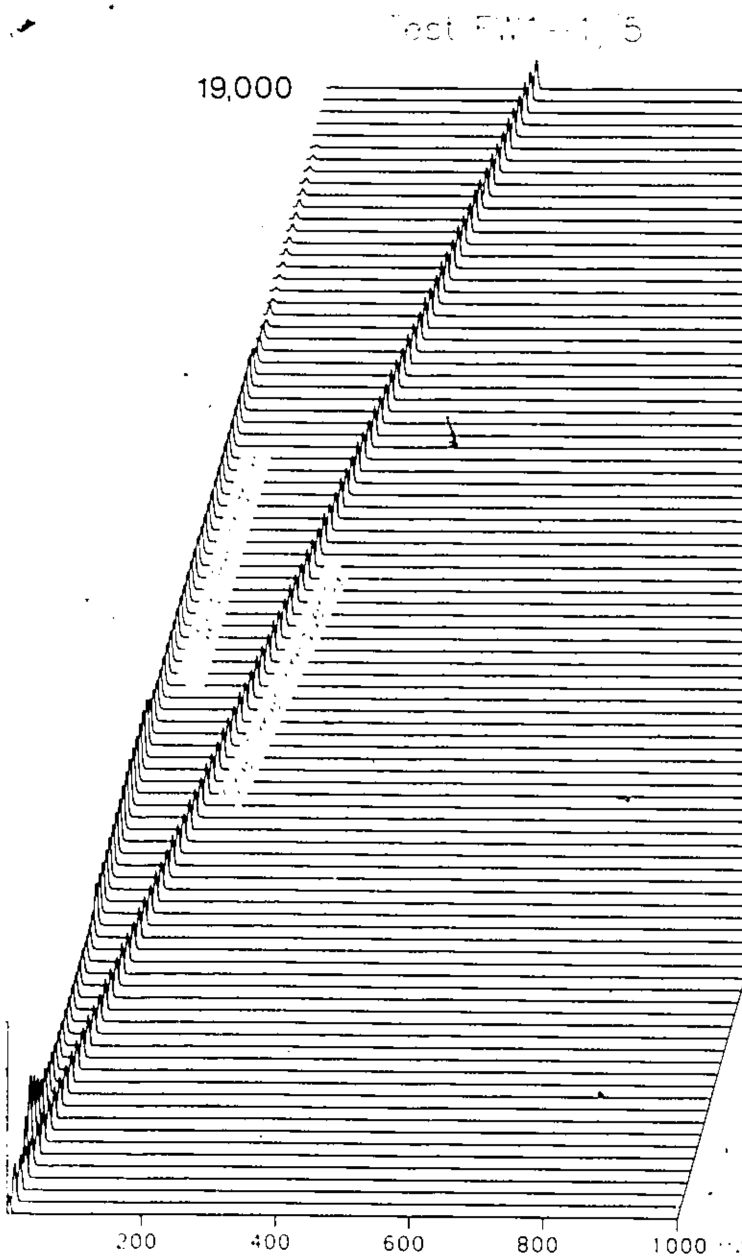

112 degrees and 7.5 mils at 292 degrees, upper and lower planes, respectively [51]. Since the location of the high spot in the lower plane is within 70 degrees of the target's built-in high spot, this suggests the lower target is moving with respect to the rotor and acting against the lower FRA.

The radial spring constants of FW1-1 were experimentally found to be 6.4 MN/m when the stiffnesses along and 45 degrees to the spokes were averaged. Assuming that the centrifugal force acting on the lower target (mass = 0.728 kg), when its center of mass is displaced a distance e meters equals the spring force of the FRA, then, for equilibrium,

$$ke = me\omega^2$$

or

$$k = m\omega^2$$

At 19,000 rpm, $m\omega^2$ = 2.9 MN/m. Thus, if the additional mass at the center of the FRA plus the screws are taken into account, the evidence suggests that the upturn in the lower-plane amplitude is an artifact, unrelated to the rotor's actual motion.

The cascade plot (Figure 5.3 on page 118) for the upper plane of test FW1-1/5 clearly shows the 1X (synchronous whirl) frequency and the oil-whip resonance. As concluded by Marchand [51], no single theory explains the persistence of the oil whip at substantially the same frequency when the rotor is operating above twice its first critical speed. Figure 5.4 shows the spectrum for this rotor's upper plane at 2400 and 18,100 rpm, the lower speed being the point at which the 1X first exceeds the oil whip in amplitude, and the higher speed being the highest speed at which it was still observable. In the first case, the whirl frequency is seen to be 600 rpm, i.e., twice first critical speed, as determined from Figure 5.5; in the second, the oil resonance is 700 rpm, i.e., it is substantially the same frequency.

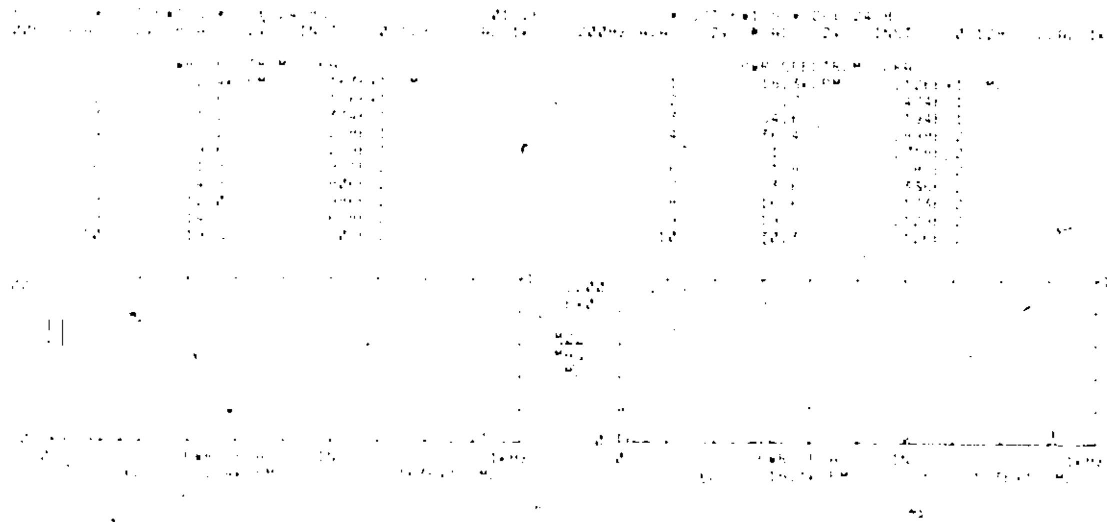

Figure 5.4: FW1-1/5 Spectra. Upper-plane spectra at 2400 rpm (L) and 18,100 rpm (R). The radial amplitudes in mils are listed above each spectogram.

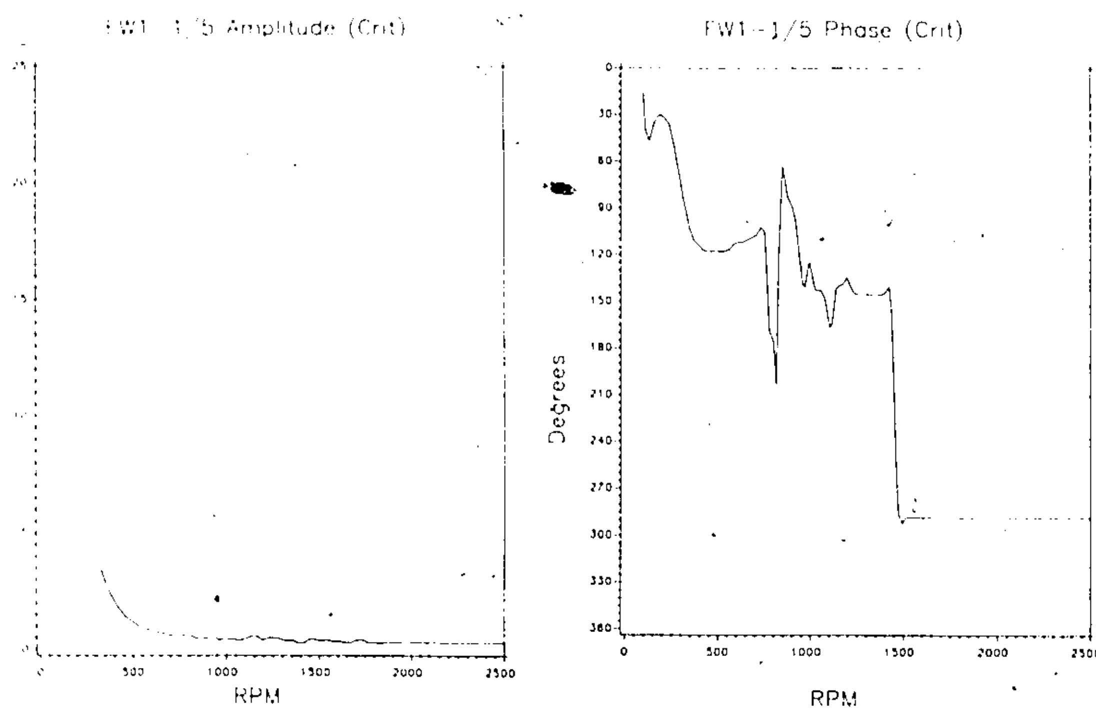

Figure 5.5: Low-Speed Bode Plot, Test FW1-1/5

Returning to the FRA spoke stiffness, if the flywheel is simplistically modelled as an undamped spring–mass system with spring stiffnesses of 5.4 and 7.5 MN/m acting on a mass of 40.9 kg, the natural frequencies are 368 and 436 r/s, or 3510 and 4160 rpm. No peaks are observed at these frequencies in the cascade plot.

5.4 Results and Discussion: FW2-1

Balancing this rotor was far more time consuming than FW1-1, requiring over 100 runs to reduce its amplitude sufficiently to permit continuing the test to maximum design speed. During this time, the full potential of the DVF2 was realized. This instrument has a feature that enables one to produce polar plots with an x–y recorder. In the process of doing this, one nulls out what is called an initial, or slow–roll, vector[19] with potentiometers in order to have the plot start at the origin. Using this feature, it is possible to measure the initial vector and manually subtract it from all subsequent amplitude/phase readings. After using this laborious technique for some time, it was pointed out by another DVF2 user[20] that, although the instrument manual is silent on the point, the nulling feature can be used at all times to automatically subtract the initial vector. This feature was used consistently with good results after Test FW2-1/4.

Table 5.3 gives the speeds attained in the four attempts, along with balance correction data and residual amplitudes at balance speed, taken after reaching the maximum speed.

---

[19] Caused by shaft bow, mechanical and electrical runout, misalignment, and bearings.

[20] Paul Kim, National Research Council of Canada.

Table 5.3: FW2-1 Test History

Test No.	Static (g-cm)	Couple (g-cm^2)	Residual Amplitudes(1) Plane 1	Plane 2	Maximum Speed
1	817.9	- (2)	1.4	1.8	16,300
2	43.5	1768.3	1.1	1.1	18,750
3	87.3	456.0	3.4	3.0	22,000
4	107.3	288.0	0.7	1.4	24,787

Note: (1) The residual filtered amplitude, peak-to-peak, in mils, at balance speed (3000 rpm) after the run up to maximum speed.
(2) Not computed.

Figure 5.6 is the cascade plot for test FW2-1/4. In this plot, the resonant oil whip disappears at 8,000 rpm, coincident with an increase in the 1X amplitude. This is consistent with the explanation of this phenomenon given previously, i.e., as the shaft loading due to imbalance force exceeds the hydrodynamic oil pressure, oil whirl ceases. It should be remembered that the FFT analyzer analyzes the signal directly from the displacement sensors, and therefore "sees" all real and apparent rotor motion, the latter including initial vectors.

The filtered amplitude/phase data available for FW2-1/4 are given in Figure 5.7 and comprise filtered amplitudes up to speed, but phase angles only up to 1500 rpm. From these plots, the nonlinear upper-plane amplitude growth pattern and the first critical speed are ascertained. The upper-plane filtered amplitudes versus speed were recorded with an x-y plotter for the final three tests in Figure 5.8. This figure represents the rotor's imbalance response for these three tests, from which it could be inferred that the balancing procedure in use at the time actually had an adverse effect. If the amplitude restrictions in effect for earlier tests had been relaxed for test FW2-1/3, it is possible

Figure 5.6: Upper-Plane Cascade Plot for Test FW2-1/4

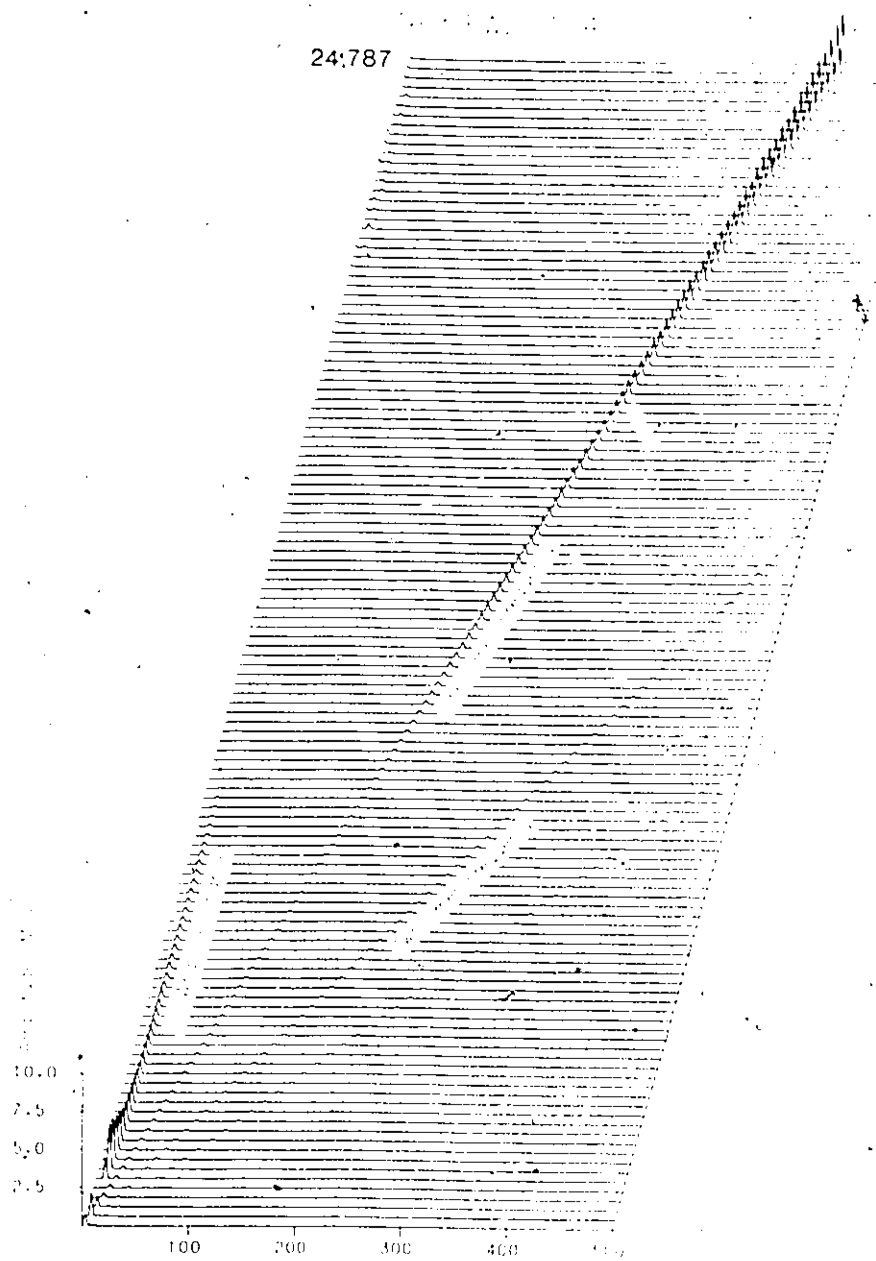

Figure 5.7: Test FW2-1/4 Bode Plots

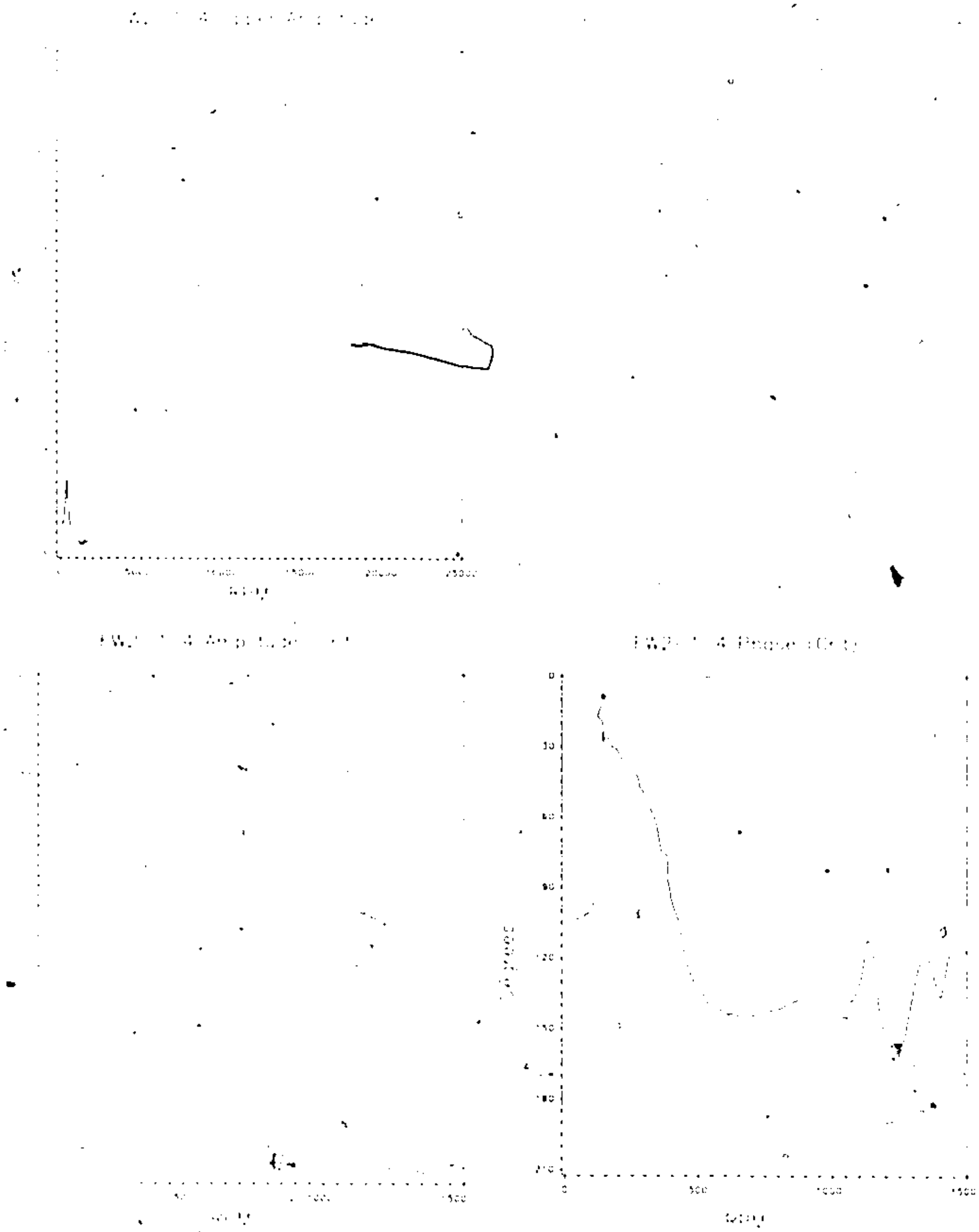

that the rotor might have achieved maximum speed sooner and with a lower amplitude.

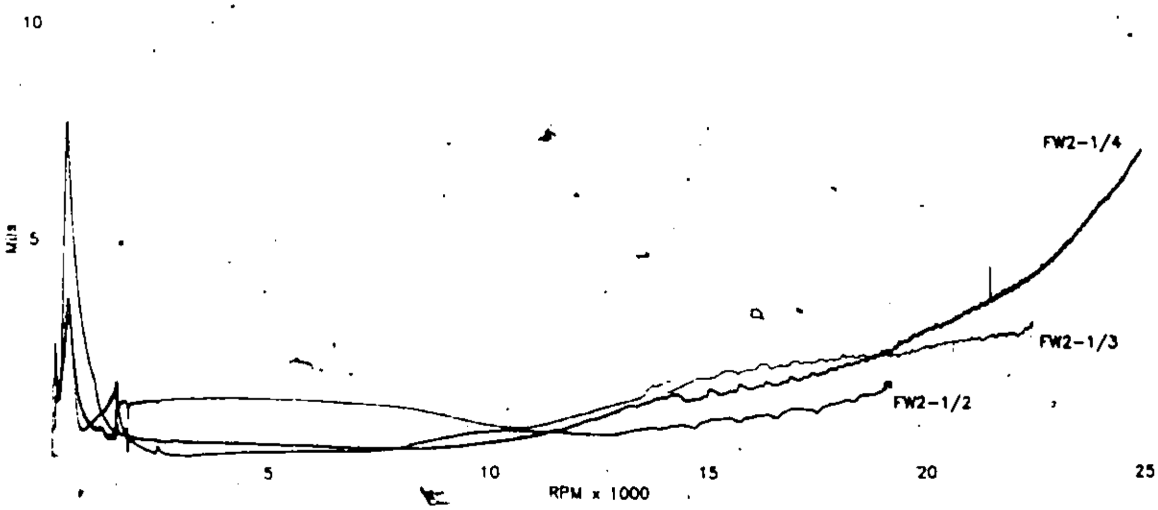

Figure 5.8: Amplitude Bode Plots, Tests FW2-1/2, /3, & /4

5.5 Results and Discussion, FW3-1

After several static and moment balance runs, FW3-1 was accelerated slowly (19 rpm/s to 13,200 rpm and 15 rpm/s thereafter) taking 21.3 minutes to reach 21,985 rpm. Using the refined procedures, this rotor was so well balanced that it had an almost imperceptible first-critical speed resonance, followed by a shallow, linear amplitude rise which, at 15,000 rpm, increased in slope but remained linear (Figure 5.9).

At maximum speed, the rotor went out of balance, contacting the upper and lower catchers. Within one video frame (1/30th of a second or 12.2 rotor revolutions) the displacement transducers were destroyed, as evidenced by the disappearance of the oscilloscope display. Ninety-six seconds later, the shaft failed and the rotor was supported by the catchers alone. The rotor came to rest in the catchers 8.5 minutes from the time of the initial imbalance.

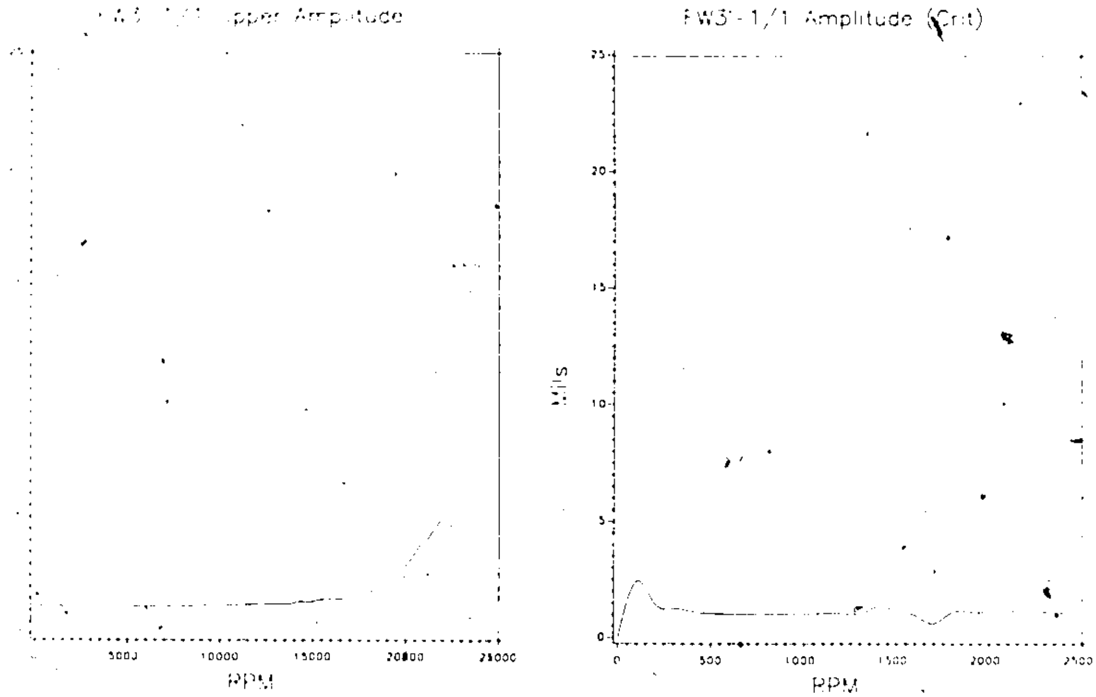

Figure 5.9: Bode Plots, Test FW3-1/1. High-speed (L) and low-speed (R) filtered amplitude versus speed, upper-plane data. The caption (CRIT) is used on all low-speed plots. No phase data were recorded.

Inspection of the rotor revealed a circumferential crack at 60% of the carbon ring radius. It was eventually concluded [10] that the ring had been subjected to premature curing due to a failure in the resin-bath heater which resulted in a measured transverse radial strength of 21 – 22 MPa, compared with the analytical stress at failure, 20.8 MPa.

The growth pattern seen in the upper plane of Figure 5.9 was first noticed in the FRH-1 rotor response which, instead of two linear regions, has four with inflection points near 14,500, 22,500, and 30,000 rpm.

While most of the small FRA-mounted rotors have displayed near-linear growth, none have shown an inflection to a second linear region. Neither SSH-1 (and -2) nor the large FRA-type rotors behaved in a linear fashion at all.

Figure 5.10: Upper-Plane Cascade Plot, Test FW3-1/1

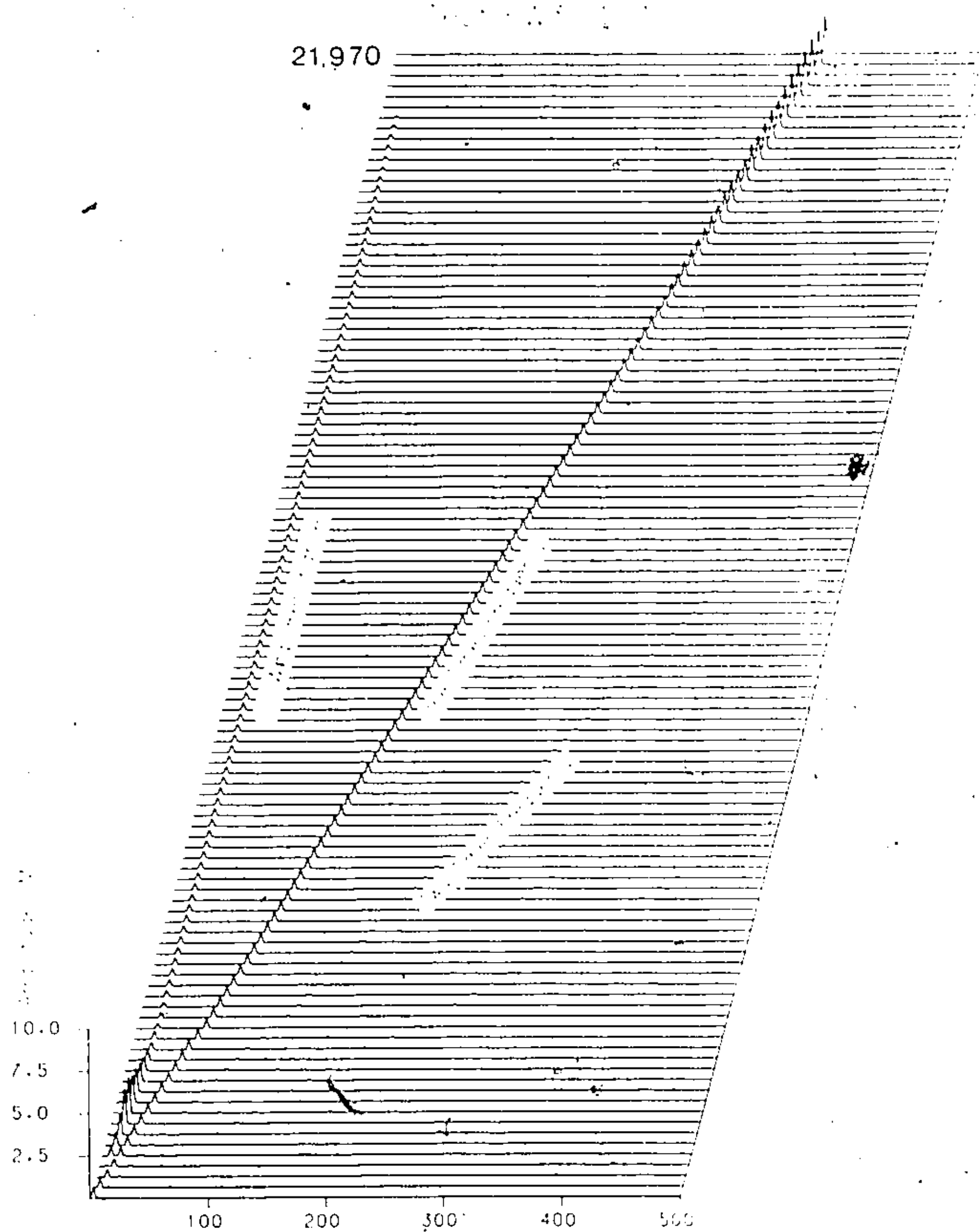

The occurrence of this phenomenon is linked to the flex-rim hub which has a variable stiffness due to the initial interference between hub and ring(s). As the rings grow with speed, there comes a point where they lift off of the hub at the spoke diameters, shown to be at 10,000 rpm for FRH-1 and calculated to be at a similar speed for FW3-1.[21] At this point, the ring is supported by the flexible rim of the hub alone and can, if not itself in perfect balance, load the now more flexible hub in such a way as to increase the mass eccentricity.

It is beyond the scope of this thesis to analyze this behavior in detail, but it can be stated that filtered-amplitude growth results from the balance between forcing functions (static and couple imbalances) and restoring functions (shaft elasticity, gyrodynamic torque, hub elasticity, and internal and external damping). The evidence for the linear-linear behavior of FW3-1 points toward variability in the hub's elasticity.

The cascade plot for FW3-1/1 is reproduced in Figure 5.10 on page 127 and shows the rotor to be quiet at all but the 1X and oil-whip frequencies. The upper-plane spectra taken before (21,820 rpm) and at failure (21,898 rpm) are shown in Figure 5.11. The onset of the ring failure was accompanied by broad-spectrum noise, as captured in the latter spectogram.

---

21 Project software calculation, R.C. Flanagan.

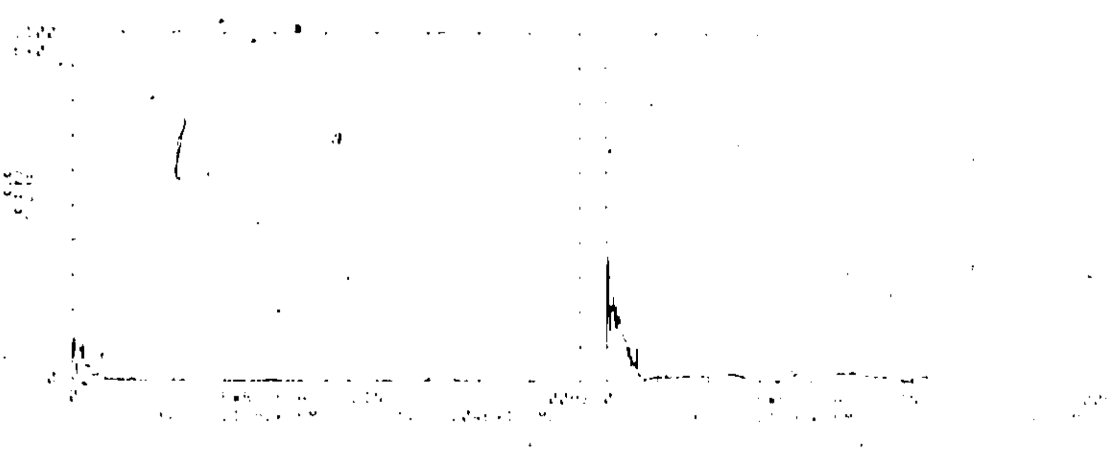

Figure 5.11: Spectra Near Failure, Test FW3–1/1. The spectra are 200 rpm before failure (L) at 21,820 rpm, and very close to failure, at 21,970 rpm (R).

5.6 Results and Discussion, FW3-2

The hub of FW3–1 was removed from the failed ring system and installed in an identical set that had been built for FW4–1. Since the carbon ring in the new system was manufactured under circumstances similar to those of the failed ring, it was decided that FW3–2 should be derated to a maximum operating speed of 20,000 rpm, a speed that it achieved on many occasions.

FW3–2 shows the same linear–linear behavior as FW3–1 (Figure 5.12). Referring to Table 5.4, the trebling of correction weights (both static and couple) at similar locations, between Tests FW3–1/1 and FW3–2/1, suggests that the rotor's imbalance is attributable, in part at least, to the lightly-damaged hub. This is a plausible reason because the new ring system installed between FW3–2/1 and FW3–3/1 did not significantly affect the amount of balance weight required.

The cascade plot for FW3–2/1, upper plane, is reproduced in Figure 5.13 and shows a somewhat higher overall 1X amplitude than FW3–1. This is emphasized by the reduction in oil–whip as well.

Figure 5.12: Bode Plots, Test FW3-2/1

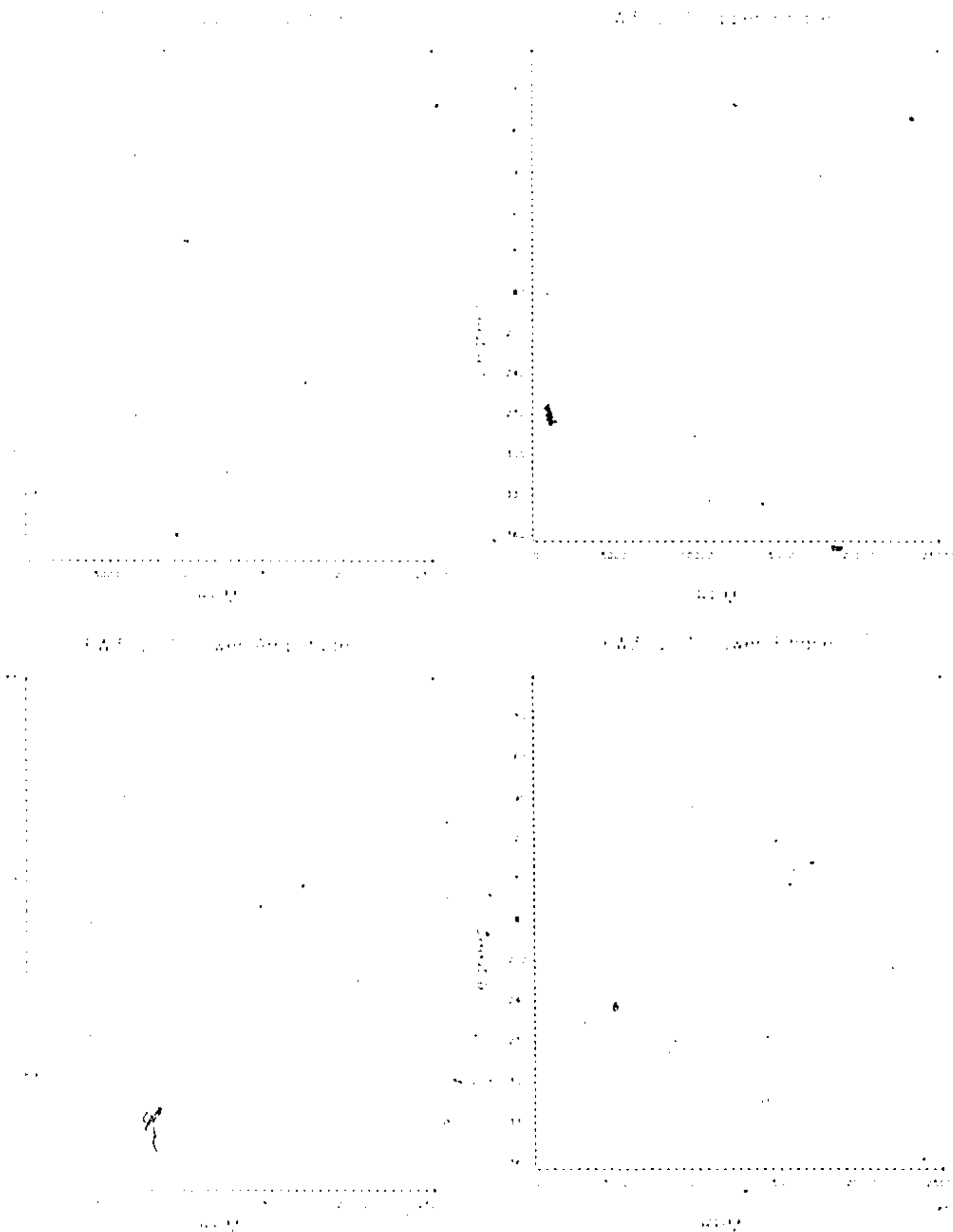

Figure 5.13: Cascade Plot, Upper Plane, Test FW3-2/1

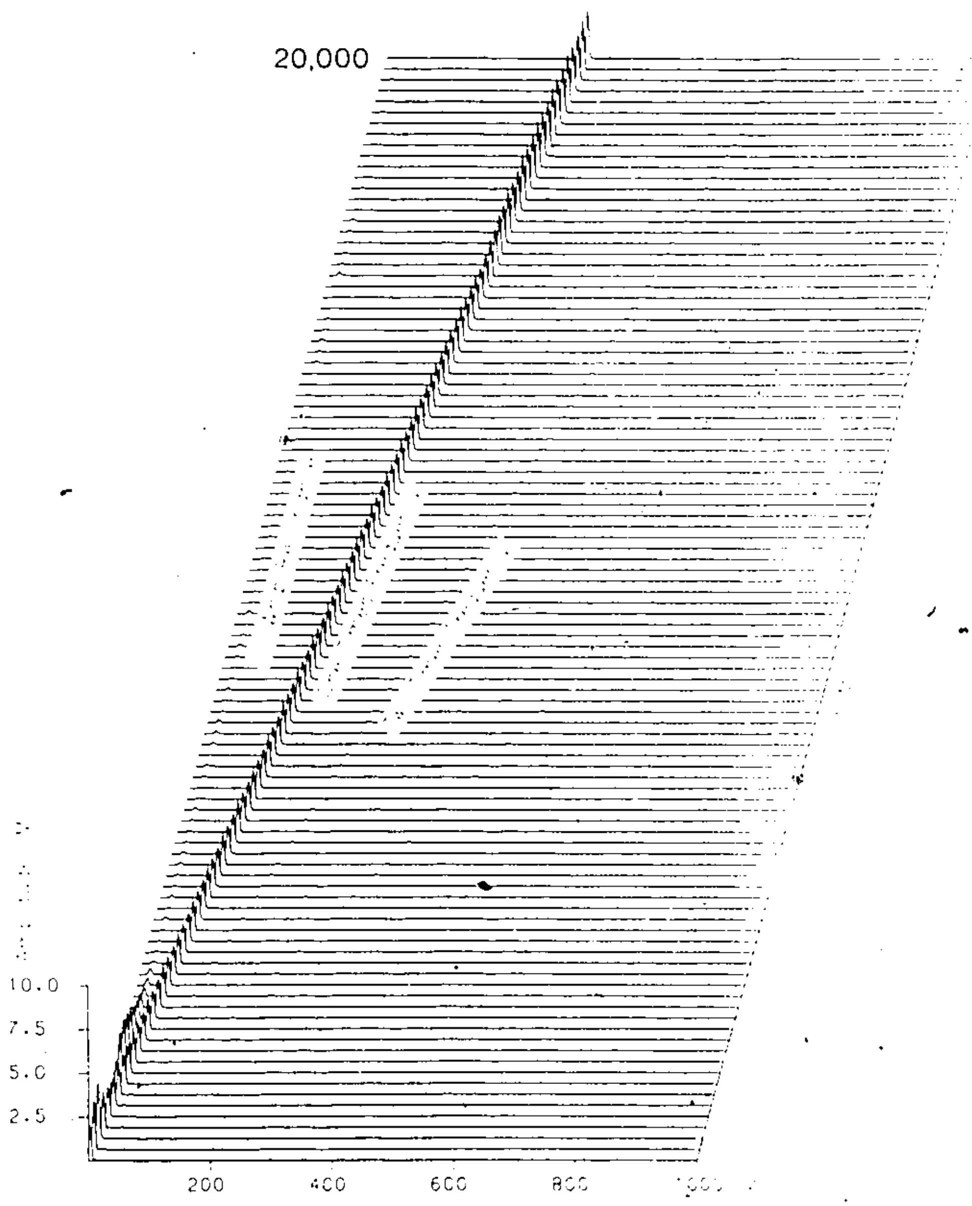

Table 5.4: FW3 Test History

Test No.	Static (g-cm)	Couple (g-cm^2)	Residual Amplitudes(1) Plane 1	Plane 2	Maximum Speed
FW3-1/1	103.4	480.1	-	-	21,898
FW3-2/1	303.4	1680.2	0.2	0.4	20,000
(2)	-	-	-	-	-
FW3-3/1	300.6	1142.3	-	-	21,345

Note: (1) The residual filtered amplitude, peak-to-peak, in mils, at balance speed (3000 rpm) after the run up to maximum speed.
(2) FW3-2 was used extensively for other experiments.

The critical-speed plot for FW3-2, representative of all three versions of FW3, is shown in Figure 5.14 and yields a value of 405 rpm.

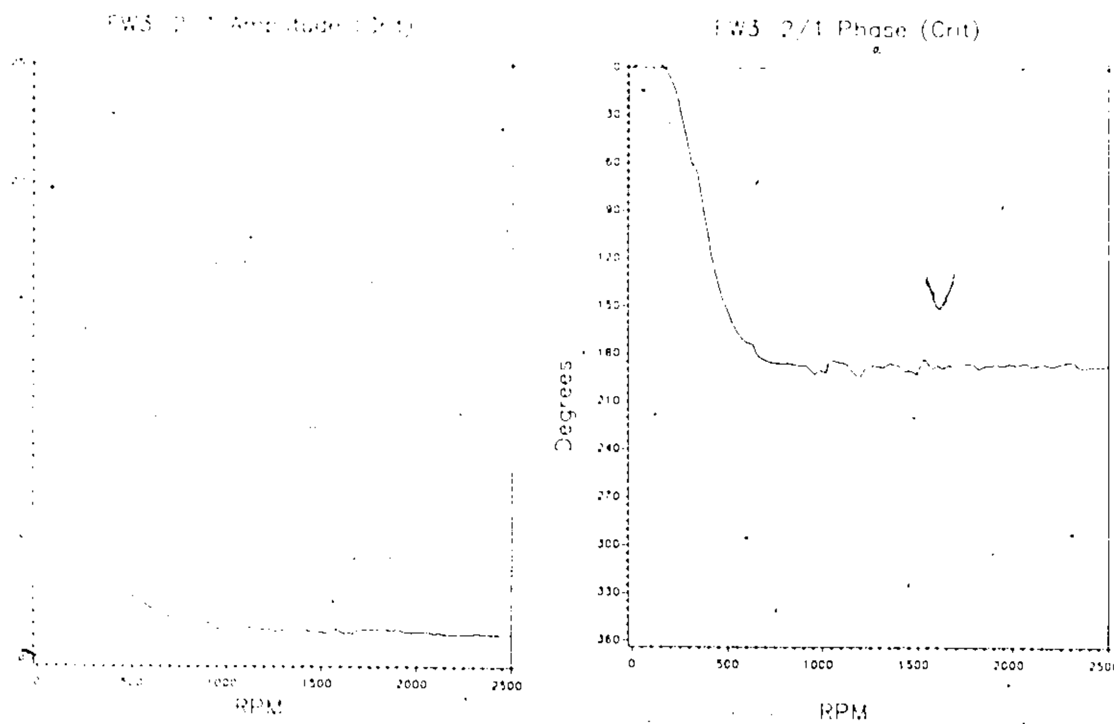

Figure 5.14: Low-Speed Bode Plot, Test FW3-2/1

5.7 Results and Discussion, FW3-3

The original FW3 hub was installed in a new ring system designed to reduce the transverse stress in the carbon ring while increasing the transverse stress in the glass ring [10]. Although the projected failure mode for this new rotor was transverse failure of the carbon ring, initially, and, after fatiguing, in the glass ring, the glass ring failed at 21,345 rpm during its first test. This failure is marked on Figure 5.15 by the near-instantaneous rise in filtered amplitude from 3.5 to 9 mils at failure speed.

Quite unlike FW3-1, this failure merely resulted in a slightly increased amplitude and, indeed, was not recognized as a ring failure until the rotor was inspected afterward. This was so unexpected that some time was spent searching for evidence of some other cause, when the cracked ring was observed almost accidentally.

In the case of the earlier carbon-ring failure, tensile tests showed the ring to be weaker in the radial direction than expected and led to corrective action. In this case, tensile test results of 19.77 +/-1.67 MPa for eight specimens[22] were very close to specification as determined by previous tests [10]. The conclusion drawn is that a local flaw, perhaps a surface crack initiated during hub insertion (the hub was cooled by damming its lower surface and filling it with liquid nitrogen) precipitated the failure.

The cascade plot for this test, Figure 5.16, gives no indication of any problem except, of course, after the fact. The failure began just as the final spectrum was being taken, as indicated by the spike in the 1X frequency at maximum speed.

---

22 M. Munro, personal communication.

Figure 5.15: Bode Plots, Test FW3-3/1

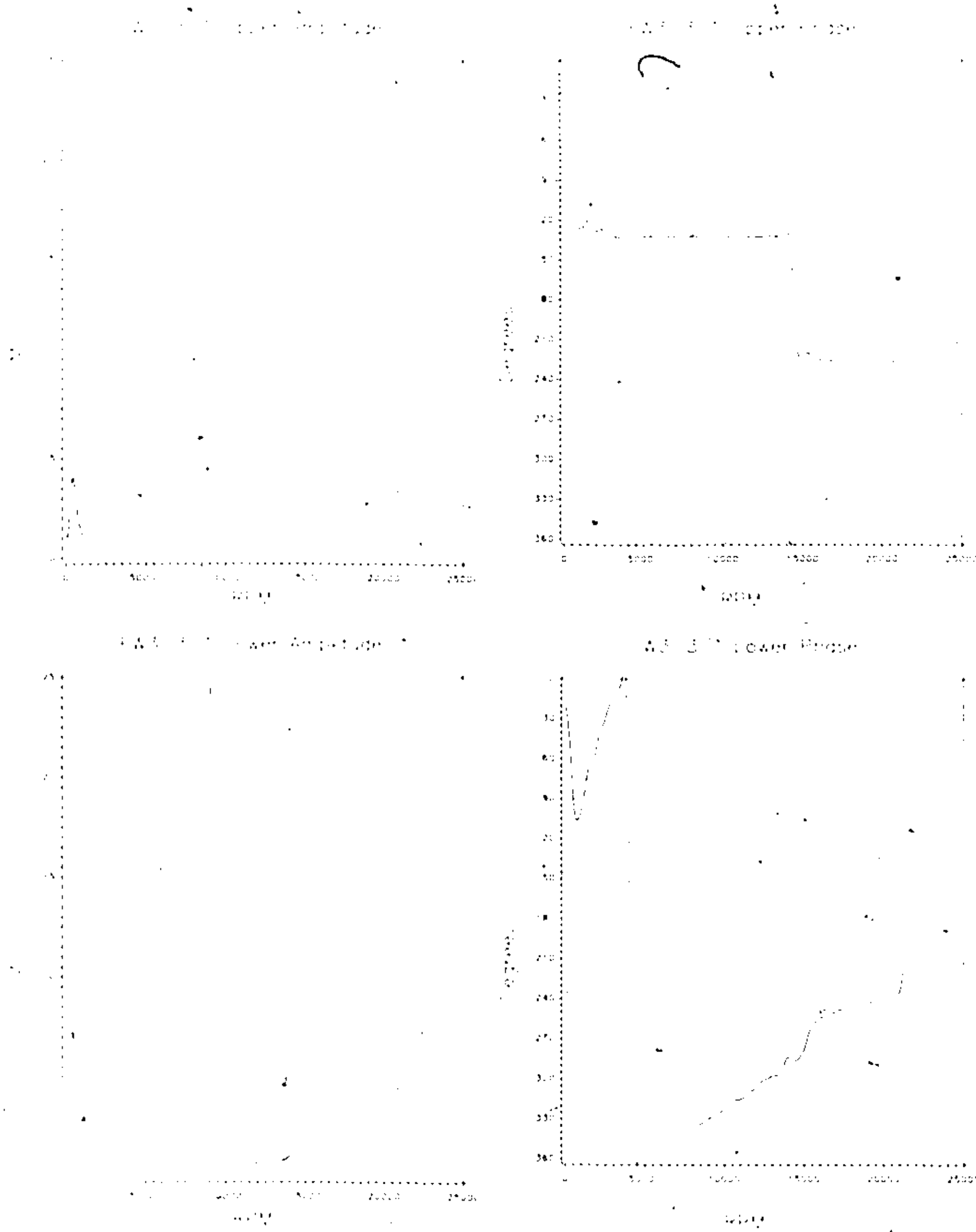

Figure 5.16: Cascade Plot, Upper Plane, Test FW3-3/1

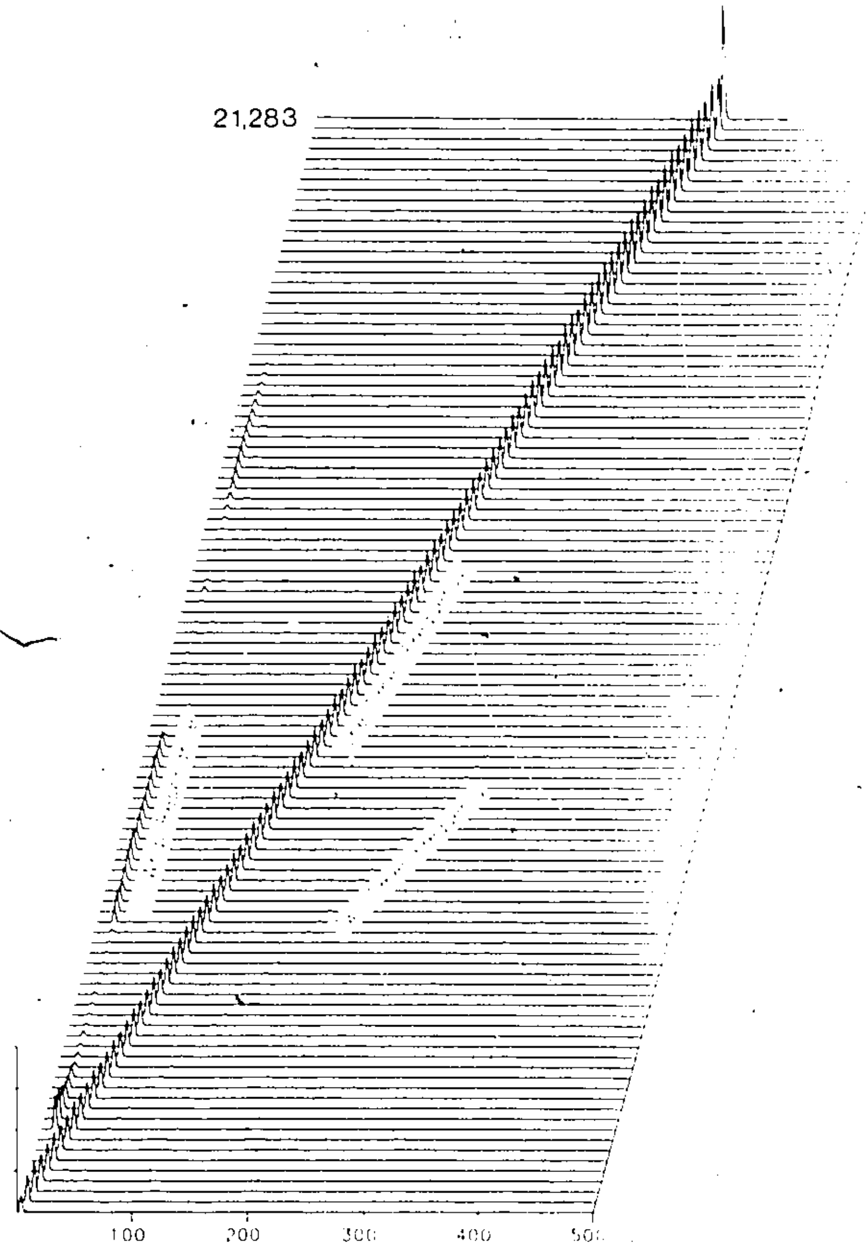

Returning to Figure 5.15, the phase discontinuity at 14,000 rpm, upper plane, coincides with the amplitude inflection point. The straight, horizontal phase trace up to 14,000 rpm means that the filtered amplitude was too low for the DVF2 to measure. When this occurs, the DVF2 registers "Phase Held" and continuously displays the last measured phase angle. Obviously, some type of unbalancing event had occurred at this point.

Comparing these results with Figure 5.12 on page 130 a similar pattern is evident, except that the phase discontinuity takes place in the lower plane during Test FW3-2/1. This could be significant, or might just mean that the balance correction weights were applied slightly differently for the two tests.

The filtered amplitude/speed plots for the three versions of FW3 are reproduced in Figure 5.17. There, the significance of the coincidence of balance condition change at 15,000 rpm for the three rotors is evident.

The cascade plot for FW3-3/1 reveals the same basic elements with two exceptions: the oil whip resonance disappears twice, then reappears and the ring failure is marked by the spike at 21,283 rpm. The change in the oil-whip resonance is most likely attributable to shaft loading and unloading caused by changes in the balance condition. This correlates with Figure 5.15 on page 134, upper-plane amplitude, which shows the load decreasing at 4500 rpm, then increasing at 9,000. Whip occurs next at the inflection point, marking the subtle, but consistent change in the rotor's balance condition.

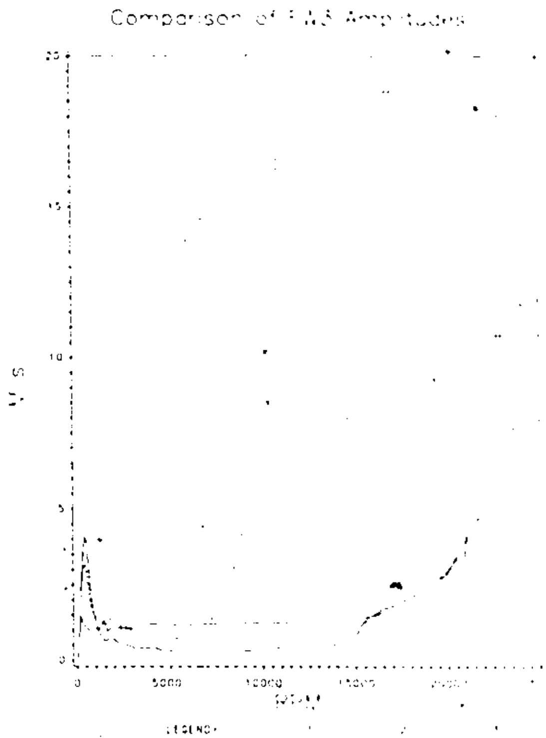

Figure 5.17: Filtered Amplitude Versus Speed, FW3 Rotors. Data are for the upper plane in each case. The legend denotes the version of FW3.

5.8 Results and Discussion, FW4-1

FW4-1 was assembled, in the manner described in Section 3.1, using the biannular ring originally built of FW4-1, but used temporarily for the FW3-2 rotor. This rotor showed a large static imbalance on a knife edge and an even larger moment imbalance in the chamber [51]. This was due to large runout and tilt values which arose from the spring plates, the arbor itself being quite concentric with the turbine shaft.

The hub was dismantled and rechecked for dimensional accuracy. Several defects were corrected and the hub reassembled such that the small amount of separation between arbor/spoke plate/bushing that was found in the first assembly was eliminated.

Nonetheless, although the runout was reduced marginally, the tilt increased by an order of magnitude and further attempts to balance the rotor were abandoned. This prudent decision was based on the exceptionally large amplitudes encountered during the balancing of the rotor as originally assembled.

5.9 Summary

In the large-rotor tests, the two FRA-mounted, composite-hub rotors, FW1-1 and FW2-1, reached their maximum design operating speeds with differing degrees of difficulty. FW1-1 balanced readily and reached speed for the first time after a modest number (15) of balance trials. FW2-1, on the other hand, required many more, namely 130 trials, including three high-speed attempts, before it succeeded.

After FW2-1/4, balance procedures were changed to utilize the nulling function of the DVF2. Had this feature been used earlier, FW2-1 might have balanced with fewer runs and achieved speed with lower amplitudes. On the other hand, it has been shown that if an eccentricity is introduced, as when the arbor targets were reground, the speed-squared forcing function on the lower arbor target, in particular, is an effect that cannot be nulled, and results in a false reading.

FW3 is superior to the composite-hub rotors in that achieving good concentricity is less of a problem. Coincidentally, improved balance procedures helped to bring FW3-1 up to speed after only 11 balance trials. The ring failures in FW3-1 and -3 were explicable and inexplicable, respectively. Tensile tests of the failed FW3-1 carbon ring proved that a manufacturing defect was responsible. Not so for FW3-3. Only the test of a new ring system, with every possible precaution taken during manufacture and assembly, will finally confirm the FRH-ring design.

The linear–linear filtered–amplitude behavior was evident in all FW3 rotors, sharing a common 15,000–rpm transition event.

A summary of the significant data for the 1–kWh rotor tests is given in Table 5.5.

Table 5.5: 1–kWh–Rotor Results

Rotor	Speeds Design (rpm)	Speeds Achieved (rpm)	Stored Energy (kWh)	Energy Density (Wh/kg)
FW1-1	19,000	19,042	0.98	24.1
FW2-1	24,787	24,787	1.32	38.3
FW3-1	21,898	21,898	1.38	36.5
FW3-2	20,000	20,000	1.15	30.8
FW3-3	21,898	21,345	1.31	34.9

Chapter VI

CONCLUSIONS

In this concluding chapter, the thesis objectives and the results of the research are brought together in order to measure the degree of success achieved.

6.1 STF Development

Starting with a test cell, a vacuum chamber, turbine controls, air supply, and audio–visual monitoring system, a world–class spin–testing laboratory has been established at the University of Ottawa. The capabilities of this facility have been expanded in the areas of vibration control and monitoring, analog and digital recording, computer control, dynamic analysis, rotor–temperature monitoring, and vacuum–pressure control.

6.2 ESR Component Performance Evaluation

In the 100–Wh–rotor test phase, a flex–rim attachment (FRA) and two metal–hub designs were tested as components. The FRA and FRH rotors were very well behaved and exhibited similar characteristics. The successful FRA test permitted composite–rotor testing, and the FRH testing proved that particular rotor–hub concept to be viable. The second metal–hub rotor, SSH–1, met its targets as well, although not as consistently or as well as FRH–1 did. In an experiment to test the SSH concept with a higher–inertia ring, the first ring–manufacture defect occurred, destroying the rotor. In this instance, the only shortcoming in the STF was the lack of a lower catcher system that would likely have saved the rotor, in view of the catcher's later success in saving the 1-kWh FRH rotor, FW3-1.

6.3 *Material Strengths*

Five material-strength tests were carried out, yielding consistent results for the two SMC bursts and the two S2L tests, the second of which resulted in a burst only after the disk was weakened with a central hole. The most important test in this series was the ring-radial strength test. It not only validated the Project ring design and concomitant stress analysis, but convincingly demonstrated that composite rotors can be built to fail in a manner so safe as to require minimal containment.

The success of these tests rested on the capability of the STF to perform them. Two of the most significant factors in this success were the acquisition of a very good air turbine, and the implementation of rotor balancing. This, coupled with the ability to accurately monitor the rotor's motion, eventually made spin testing quite routine.

6.4 *1-kWh-Rotor Performance*

Building on the experience with the smaller rotors, and with the installation of additional equipment, particularly the lower catcher system, large-rotor testing likewise soon became routine. Of the three rotors tested, FW3 proved superior on the basis of alignment, ease of balance correction, and repeatability. The fact that two ring failures occurred does not lessen the overall strong points in this rotor, but it does suggest that there is room for improvement in manufacture and assembly.

The fourth rotor design, FW4-1, apparently suffered from an alignment problem that was correctable on the small SSH rotor, but not the large one. Although an attempt was made to balance it, the amount of runout and tilt made this impractical.

During the large-rotor testing, the addition of digital data acquisition and FFT analysis increased the data-analysis capability considerably. The performance of the large rotors was, accordingly, easier to assess.

6.5 Conclusions

The University of Ottawa Rotor Project has contributed significantly to the body of fiber-composite flywheel technology. Part of this contribution was due to the Spin-Test Facility's capabilities which met or exceeded expectations and which are equivalent to laboratories described in the literature.

In the STF, the unprecedented through-drilling of composite hubs was proven not to weaken the disk specimens which were shown to fail at their centers. Repeatable SMC biaxial strength values were obtained and the highest ever S2-glass laminate failure stress was recorded. These material tests, plus the ring radial strength test, all supported the through-drilling concept (and FRA design) and are in themselves significant contributions.

The RRS test and the two unplanned FW3 ring failures are likewise significant in proving the safety of the benign ring failure-mode approach. The FW3 glass-ring failure, particularly, ensures that containment requirements can be minimized.

The thesis objectives may therefore be said to have been successfully met.

BIBLIOGRAPHY

Nine documents from two different symposia are referred to frequently as follows:

- FTS_Flywheel Technology Symposium, held in 1975, '77, and '80, sponsored by the US Government.
- CRM_Contractors' Review Meeting, annually to share results of the previous year's work with each other and the sponsoring agency, the US Department of Energy. These Symposia are listed as references [23 - 31].

1. Decker, H.D., UMTA Flywheel Trolley Coach Program Overview, CRM, 1980, p.13.
2. Togwood, D.A., An Advanced Vehicular Flywheel System for the ERDA Electric Powered Passenger Vehicle, FTS, 1977, p.63.
3. Satchwell, D.L., An Advanced Energy Storage Unit for a US Postal Service Delivery Vehicle, FTS, 1977, p.69.
4. Frank, A.A. and Beachley, N., Improved Fuel Economy in Automobiles by use of Flywheel Energy Management Systems FTS, 1975, p.76.,
5. Pezdirtz, G.F., Keynote Address, FTS, 1975, p. 3.
6. Davis, D. and Hodson, D., Rocketdyne's High-Energy Storage Flywheel Module for the US Army, FTS, 1977, p. 55.
7. Rinehart, D.E., A Flywheel Energy Storage Propulsion System for Intra Urban Buses, FTS, 1980, p. 145.
8. University of Ottawa ESR Research Team, High Energy Density Fibre Composite Rotors, Vol. 7, Mech. Eng. Tech. Rept. No. UOME-FP-8608-1, Ottawa, Canada, 1986.

9. Van Altena, G.J.W., Development of a Flywheel Storage System for Electrical Energy Applications, FWTS, 1980, p. 68.

10. University of Ottawa ESR Research Team, High Energy Density Fibre Composite Rotors, Vol. 8, Mech. Eng. Tech. Rept. No. UOME-FP-8609-1, Ottawa, Canada, 1986.

11. Jones, R.M., Mechanics of Composite Materials, Scripta Book Company, Washington, DC, 1975, p. 23.

12. Babelay, E.F., Jr., Flywheel and Containment Testing in FY 83, CRM, 1983, p.164.

13. Eisenhaure, D.B., Bliamptis, T.E., and Johnson, B.G., Mechanical Energy Storage Application Studies, CRM, 1981.

14. Krupka, M.C. and Jackson, S.V., Assessment of Taxicab Fleet Operations in New York City, CRM, 1981.

15. Frank, A.A. and Beachley, N.H., Control-Strategy Study for a Heat-Engine/Flywheel/CVT Vehicle, CRM, 1981.

16. Rabenhorst, D.W., Flywheel Programs in Other Countries, FTS, 1977, p.27.

17. Besel, G. and Erich, H., Flywheel Energy Accumulators for City Buses - Steel and Composite Design, FTS, 1980, p.4.

18. Poubeau, P.C., Flywheel Energy Storage Systems Operating on Magnetic Bearings, FTS, 1980, p.55.

19. Genta, G., Spin Tests on Medium Energy Density Flywheels, Composites, Vol. 13, Jan 1982, p.38.

20. Flanagan, R.C., Suokas, L.A., and St. Laurent, R., Mechanical Hybrid Drive for UTDC Minibus, Proceedings of the Third Symposium on Engineering Applications of Solid Mechanics, Toronto, June 1976, pp. 173-238.

21. Flanagan, R.C. and Suokas, L.A., Regenerative Drive for Subway Trains, Trans. ASME, J. Engineering for Industry, Vol. 98, 1976, pp. 737-760.

22. Flanagan, R.C. and Munro, M.B., Evaluation of and Program Recommendations for Anisotropic Materials, Tech. Rept. No. UOME-FP-8102-1, Feb 1981.

23. FTS, 1975, Proceedings of the 1975 Flywheel Technology Symposium, Lawrence Livermore Laboratory, Livermore, California, NTIS Report No. CONF-751133.

24. FTS, 1977, 1977 Flywheel Technology Symposium Proceedings, October 5-7, San Francisco, California, NTIS Report No. CONF-771053.

25. FTS, 1980, 1980 Flywheel Technology Symposium, October, 1980, Scottsdale, Arizona, NTIS Report No. CONF-801022.

26. CRM, 1978, Proceedings of the 1978 Mechanical and Magnetic Energy Storage Contractors' Meeting, October 24-26, 1978, Luray, Virginia, NTIS Report No. CONF-781046.

27. CRM, 1979, Proceedings of the 1979 Mechanical and Magnetic Energy Storage Contractors' Meeting, August, 1979, Washington, D.C., NTIS Report No. CONF-790584.

28. CRM, 1980, Proceedings of the Mechanical, Magnetic, and Underground Energy Storage 1980 Annual Contractors' Review, Washington, D.C., November 10-13, 1980 NTIS Report, No. Conf-801128.

29. CRM, 1981, Proceedings of the Mechanical, Magnetic, and Underground Energy 1981 Annual Contractors' Review, Washington, D.C., August 24-26, 1981, MCC Associates, Inc., 8534 2nd Ave, Silver Spring, Md. 20910, USA.

30. CRM, 1982, Proceedings of the DOE Physical and Chemical Energy Storage Annual Contractors' Review Meeting, Arlington, Virginia, August 24-26, 1982, NTIS Report No. Conf-820827.

31. CRM, 1983, Proceedings of the DOE Physical and Chemical Energy Storage Annual Contractors' Review Meeting, Arlington, Virginia, September 12-14, 1983, NTIS Report No. CONF-830974.

32. Rabenhorst, D.W., Flywheel Testing Laboratory of the Johns Hopkins University, Applied Physics Laboratory, Flywheel Testing Conference, San Francisco, April 24, 1979.

33. Smith, B.B., Flywheel Test Facility, CRM, 1978, p. 76.

34. Steele, R.S., Oak Ridge Flywheel Evaluation Laboratory, CRM, 1979, p. 416.

35. Raynard, A.E., Electric/Flywheel Powered Postal Vehicle Development Program, CRM 1979, p. 466.

36. Lawson, L.J., Flywheel Trolley Coach Propulsion with a High Capacity Composite Flywheel, FWTS, 1980, p. 153.

37. Davis, D.E., Advanced Composite Flywheel for Vehicle Application, CRM, 1978, p. 164.

38. Olszewski, M., Mechanical Energy Storage Technology Program FY 1982 Technical Progress Report, Oak Ridge National Laboratory Report No. ORNL/TM-8765, July, 1983.

39. Jarvinen, P.O., Advanced Flywheel Storage System, CRM, 1981.

40. Norrup, L.V., LLL/AiResearch Advanced Energy Storage Unit Development Project, CRM 1979, p. 488.

41. Thomson, W.T., Younger, F.C., and Gordon, H.S., Whirl Stability of the Pendulously Supported Flywheel System, J. Appl. Mech., Vol. 99, pp. 322-328, 1977.

42. Den Hartog, J.P. Mechanical Vibrations, McGraw-Hill Book Co., New York, 1956.

43. McRae, J., Flywheel Spin-Test Facility Modifications, Start Up and Dynamic Rotor Testing, MEng Report, University of Ottawa, 1981.

44. Bert, C.W. and Ramunujam, G., Design Guide for Composite-Material Flywheels: Rotor Dynamic Considerations Part I - System Whirling and Stability, University of Oklahoma Research Report OU-AMNE-81-5, September, 1981.

45. Wong, J., Flanagan, R.C., Munro, M.B., and Miyase, A., Analysis and Design of a 1.0 kWh Anisotropic Material Flywheel, Tech. Rept. No. UOME-FP-8102-1, Oct 1981.

46. Hendry, R.S., The Design and Fabrication of a High Speed Rotor Test Facility, Fourth Year Thesis, University of Ottawa, 1980.

47. Roy, D., Development of a Dynamic Testing Facility for High Energy Density Fiber Composite Flywheels, Fourth Year Thesis, University of Ottawa, 1982.

48. Weast, R.C., Ed., CRC Handbook of Chemistry and Physics, The Chemical Rubber Company, Cleveland, Ohio, 1969.

49. Flanagan, R.C., Miller, P.A., Munro, M.B., McRae, J., and Wong, J., Design and Development of a High-Speed Spin Test Facility and Rotor Dynamic Testing, Tech. Rept. UOME-FP-8305-1, Jan 1983.

50. Marchand, P., The Design and Fabrication of a Dynamic Balancing Facility, Fourth Year Thesis, University of Ottawa, April 1983.

51. Marchand, P., Static and Dynamic Balancing of High-Speed Fiber-Composite Flywheels, MASC Thesis, University of Ottawa, 1986.

52. Green, K., Design and Manufacture of High-Speed Fiber-Composite Flywheel Components, MEng Report (In preparation), University of Ottawa, 1986.

53. University of Ottawa ESR Research Team, High Energy Density Fibre Composite Rotors, Vol. 3, Mech. Eng. Tech. Rept. No. UOME-FP-8605-1, Ottawa, Canada, 1986.

54. Nimmer, R.P., Torossian, K., and Hickey, J., Laminated Composite Disc Fly-wheel Development, General Electric Company Report SRD-80-091, February, 1980.

55. Daniel, I.M., Behavior of Graphite/Epoxy Plates with Holes under Biaxial Loading, Experimental Mechanics, January 1980, pp. 1-8.

56. Nuismer, R.J. and Whitney, J.M., Uniaxial Failure of Composite Laminates Containing Stress Concentrations, Symposium on Fracture Mechanics of Composites, ASTM 593, 1975, pp. 117-142.

57. Timoshenko, S.P. and Goodier, J.N., Theory of Elasticity, 3rd Edition, McGraw-Hill Book Co., New York, 1970.

58. Mandell, J.F., Fatigue Behavior of Fiber-Resin Composites, In "Developments in Reinforced Plastics", Edited by G. Pritchard, Applied Science Publications, 1982.

59. Baird, D.C., An Introduction to Measurement Theory and Experiment Design, Prentice-Hall, Inc., Englewood Cliffs, New Jersey, 1962.

60. Aleong, C., Experimental Determination of Residual Stress in Filament Wound Composite Rings, MASc Thesis, University of Ottawa, 1986.

61. University of Ottawa ESR Research Team, High Energy Density Fibre Composite Rotors, Vol. 4, Mech. Eng. Tech. Rept. No. UOME-FP-8605-1, Ottawa, Canada, 1986.